

# **AERODYNAMIC PERFORMANCE OF LEADING EDGE PROTUBERANCES AT LOW REYNOLDS NUMBER**

Thesis

Submitted in partial fulfillment of the requirements for the degree of

**DOCTOR OF PHILOSOPHY**

by

**JAYAPAL REDDY CHITTEPU**

168005ME16P04




**DEPARTMENT OF MECHANICAL ENGINEERING  
NATIONAL INSTITUTE OF TECHNOLOGY KARNATAKA  
SURATHKAL, MANGALURU - 575025, INDIA**

**May 2024**

**DECLARATION**  
*(by the Ph.D. Research Scholar)*

I hereby declare that the Research thesis entitled '**AERODYNAMIC PERFORMANCE OF LEADING EDGE PROTUBERANCES AT LOW REYNOLDS NUMBER,**' which is being submitted to the **National Institute of Technology Karnataka**, Surathkal in partial fulfillment of the requirements for the award of the degree of **Doctor of Philosophy in Mechanical Engineering** is a bonafide report of the research work carried out by me. The material contained in this Research thesis has not been submitted to any University or Institution to award any degree.


  
Name: **Mr. JAYAPAL REDDY C**  
Register No.: **168005 ME16P04**  
Department of Mechanical Engineering

Place: NITK - Surathkal


Date: 31 / May / 2024

## CERTIFICATE

This is to certify that the Research Thesis entitled '**AERODYNAMIC PERFORMANCE OF LEADING EDGE PROTUBERANCES AT LOW REYNOLDS NUMBER**' submitted by **Mr. Jayapal Reddy C (Register Number: 168005ME16P04)** as the record of the research work carried out by him is accepted as the Research thesis submission in partial fulfillment of the requirements for the award of the degree of **Doctor of Philosophy**.

  
**Dr. A. Sathyabhama**  
Research Guide  
Professor  
Dept. of Mechanical Engg.  
NITK Surathkal - 575025



  
**Chairman - DRPC**  
(Signature with Date and Seal)

*I dedicate this thesis to  
my beloved wife **Harika**  
and  
cherished daughters **Rudhira Taara and Niteeksha***



## **ACKNOWLEDGEMENTS**

I would like to express my sincere gratitude to the following individuals who have contributed significantly to the completion of this very long journey.

I am deeply thankful to Dr. A Sathyabhama for her invaluable guidance, unwavering support, and expert advice throughout the entire research process. Her mentorship and insightful feedback have been instrumental in shaping the direction and quality of this work. I express my gratitude for the generous guidance and valuable suggestions provided by the members of the Research Progress Assessment Committee, namely Dr. P Jeyraj and Dr. K.S. Ravishankar. I would also like to extend my thanks to the Head of the Mechanical Engineering Department for their unwavering support throughout this journey. Additionally, I am grateful to all individuals who served as the head of the Mechanical Engineering Department during my research tenure.

I want to thank my fellow researchers and colleagues who provided a collaborative and stimulating academic environment. Their discussions, and feedback made the research journey more enriching and enjoyable. My heartfelt thanks go to my wife and sister for their unwavering support, love, and understanding throughout this academic endeavor. I am also grateful to my friends for their encouragement and shared moments that provided much-needed breaks and laughter.

I am grateful to National Institute of Technology Karnataka for providing the necessary resources, library facilities, and a conducive academic environment that facilitated my research. I acknowledge the financial support provided by the Science and Engineering Research Board and the Department of Science and Technology, Government of India. Their support played a crucial role in carrying out this research successfully.

This thesis would not have been possible without the collective support of these individuals and Institution. Thank you for being an integral part of this academic journey.

(JAYAPAL REDDY CHITTEPU)



## ABSTRACT

Wind energy plays a pivotal role in the renewable energy sector, offering sustainable and clean electricity, thus mitigating climate change by reducing greenhouse gas emissions and diversifying the energy mix away from fossil fuels. With increasing electricity demand, environmental concerns, and technological advancements, wind energy has gained prominence. The ambition for green energy heavily relies on tapping into the largely untapped potential of Small Horizontal Axial Wind Turbines (SHAFT). These turbines often face challenges such as low wind speed, small rotor size, and laminar separation, resulting in poor performance. Enhancing the aerodynamic efficiency of small wind turbine blades is crucial for increasing power and overall effectiveness. Various active and passive techniques are available to improve turbine blade aerodynamics. One passive method involves adopting leading-edge modifications inspired by Humpback Whale tubercles. These modifications, particularly effective in low Reynolds number flows, enhance aerodynamic performance by elevating the maximum lift coefficient and delaying stall.

In the first section of thesis, a detailed investigation on the aerodynamic performance of two distinct airfoils, E216 and SG6043, operating at 100K Reynolds numbers is presented. The emphasis is primarily on the effect of leading-edge protuberances on the aerodynamic properties of these airfoils. Numerical simulations in ANSYS FLUENT using the SST  $k - \omega$  turbulent flow model and experimental analyses in a subsonic wind tunnel using a sensitive three-component force balance were carried out. Three protuberance shapes were investigated: sinusoidal, slot, and triangular, with amplitudes ( $A$ ) of  $0.03c$ ,  $0.06c$ , and  $0.11c$  and wavelengths ( $W$ ) of  $0.11c$ ,  $0.21c$ , and  $0.43c$  relative to the chord length ( $c$ ) of the airfoil. The variation in amplitude and wavelength combinations resulted in nine distinct models. The numerical study examined fifty six models, including baseline and protuberance models of E216 and SG6043 airfoils. Out of these, wind tunnel experiments were conducted on the baseline model as well as one model each of the three protuberance shapes to validate the numerical findings, totalling eight models for validation. The studies covered an angle of attack range of  $0^\circ$  to  $20^\circ$ .

Numerical results showed that the sinusoidal protuberances caused a  $2^\circ$  stall delay with lower amplitudes, improving E216 A4.5W64.5  $C_{lmax}$  by 2.88% and  $(L/D)_{max}$  by 6.22%. However, for SG6043,  $C_{lmax}$  decreased by 10.21%, and  $(L/D)_{max}$  dropped by 4.38%. Triangular

protuberances also delayed stall by  $2^\circ$  to  $4^\circ$  for E216 A4.5 and A9, enhancing  $C_{lmax}$  and  $(L/D)_{max}$ . The E216 A4.5W64.5 model exhibited an 11.2%  $C_{lmax}$  increase and a 14.43% rise in  $(L/D)_{max}$  at stall angle, while SG6043 A4.5W64.5 showed a 4.37%  $C_{lmax}$  decrease and a 1.92%  $(L/D)_{max}$  drop at stall angle. Slot protuberances also delayed stall by  $2^\circ$  to  $4^\circ$ . The E216 airfoil demonstrated improved  $C_{lmax}$  and stall delay, while SG6043 enhanced  $C_{lmax}$  but reduced  $(L/D)_{max}$ . Slot and triangular A4.5 models excelled in stall delay and post-stall performance, favoring low amplitude and high wavelength configurations.

Further, the study was extended to investigate the effects of Reynolds numbers on E216 airfoil experimentally using strain gauges and data acquisition arrangement in subsonic wind tunnel facility. The Reynolds numbers considered for experimental investigation are 50K, 100K, and 150K. The study explored Reynolds number effects on protuberances, revealing minimal impact at 50K Reynolds numbers. However, at 100K and 150K Reynolds numbers, improvements were evident: enhanced post-stall lift coefficients and stall delay compared to the baseline. At 150K Reynolds number, slot, triangular, and sinusoidal protuberances showed notable increases in maximum lift coefficients by 29%, 23%, and 13%, respectively, compared to the baseline.

Furthermore, this study was extended to experimentally investigate the aerodynamic behaviour of the E216 airfoil with protuberances under dynamic conditions. This investigation made use of a stepper motor, strain gauges, and a data acquisition system in a subsonic wind tunnel facility. The reduced frequencies ( $k$ ) considered in this study are 0.025, 0.05, and 0.065. In essence, introducing protuberances to the airfoil not only influences lift coefficient patterns but also affects the hysteresis loop size during dynamic stall. Moreover, protuberance models exhibited smoother post-stall behavior compared to the baseline. Overall, slot and triangular protuberances notably enhanced  $C_{lmax}$  compared to both the baseline and sinusoidal protuberance models.

The smoke and tuft flow visualization techniques revealed important insights into flow patterns, assisting in understanding the flow physics. The smoke flow study observed increased post-stall lift with increasing angles of attack due to the merging of secondary flow with primary flow. While sinusoidal and triangular profiles exhibited similar behavior, triangular leading edges effectively guided flow to trough regions, resulting in a larger secondary flow volume. Triangular protuberances proved more effective for drag reduction on

the SG6043 airfoil, particularly at a Reynolds number of 100K, and contributed to post-stall lift improvement. According to the tuft flow visualization, separation of flow was observed at different distances from the leading edge in protuberance models, around 22% for the sinusoidal model and 24% for the triangular and slot configurations. Significantly, both the slot and triangular protuberance models showcased improved attached flow within the troughs, leading to elevated lift coefficients and stall delay.

The investigation was extended further to examine the aerodynamic performance of Small Horizontal Axis Wind Turbines (SHAWT) with protuberance blades, comparing them with the baseline blades. The aerodynamic performance of wind turbines featuring various protuberance blade models – sinusoidal, triangular, and slot designs, were tested and contrasted with the baseline. Based on the results, the enhancement in power coefficient ( $C_P$ ) for protuberance configurations is as follows: 2.7 % for sinusoidal, 5.2 % for triangular, and 7.6 % for slot blades compared to baseline blades. The slot protuberances blade model displayed the highest  $C_P$  value among the three shapes. This suggests that wind turbines incorporating slot, triangular, and sinusoidal protuberances achieved improved aerodynamic efficiency compared to baseline blades.



# TABLE OF CONTENTS

ACKNOWLEDGEMENTS .....	ii
ABSTRACT .....	iv
LIST OF FIGURES .....	xii
LIST OF TABLES .....	xviii
NOTATION .....	xx
ABBREVIATIONS .....	xxiii
CHAPTER 1.....	1
INTRODUCTION.....	1
1.1    SMALL SCALE WIND TURBINES.....	2
1.2    LOW REYNOLDS NUMBER AERODYNAMICS.....	3
1.3    LAMINAR SEPARATION BUBBLE .....	5
1.4    FLOW CONTROL TECHNIQUES .....	6
1.4.1    Blowing and Suction .....	6
1.4.2    Dimple actuators or Electroactive polymer actuators .....	7
1.4.3    Synthetic jet actuators .....	8
1.4.4    Vortex generators.....	8
1.4.5    Tubercles or Leading edge Protuberances.....	9
1.5    STALL.....	10
1.6    DYNAMIC STALL.....	11
1.7    SCOPE OF PRESENT WORK.....	13
1.8    OVERVIEW OF THE THESIS.....	13
CHAPTER 2.....	15
LITERATURE REVIEW .....	15
2.1    REYNOLDS NUMBER EFFECTS.....	15
2.2    EFFECT OF TUBERCLES ON AIRFOIL PERFORMANCE .....	16
2.2.1    Static study .....	16
2.2.2    Dynamic study.....	19
2.3    FLOW VISUALIZATION STUDY .....	22
2.3.1    Tuft flow visualization .....	22
2.3.2    Smoke flow visualization .....	23
2.4    WIND TURBINES WITH LEADING EDGE PROTUBERANCES .....	24
2.5    SUMMARY .....	26
2.6    RESEARCH GAP .....	26
2.7    RESEARCH OBJECTIVES .....	27
CHAPTER 3.....	29

RESEARCH METHODOLOGY .....	29
3.1  EXPERIMENTAL METHODOLOGY .....	29
3.1.1  Subsonic Wind Tunnel Facility.....	29
3.1.2  Three-component force balance and Load cell arrangement.....	30
3.1.3  Airfoil model design and fabrication.....	32
3.1.4  Geometry modelling.....	32
3.1.5  Model mounting arrangement.....	36
3.1.6  Pitot tube measurements.....	37
3.1.7  Boundary layer measurements.....	38
3.1.8  Wind Tunnel Corrections.....	39
3.1.9  Wind tunnel turbulence intensity.....	41
3.1.10  Experimental procedure and data processing .....	41
3.1.11  Uncertainties in the experiment.....	45
3.1.12  Smoke flow visualization setup.....	45
3.1.13  Tuft flow visualization arrangement.....	46
3.2  NUMERICAL METHODOLOGY .....	47
3.2.1  Computational fluid domain and Boundary conditions.....	47
3.2.2  Governing Equations and Turbulence model .....	48
3.2.3  Grid independent study.....	50
CHAPTER 4.....	53
RESULTS & DISCUSSIONS .....	53
4.1  NUMERICAL SCHEME VALIDATION.....	53
4.2  EXPERIMENTAL REPEATABILITY .....	54
4.3  STATIC STUDY.....	55
4.3.1  Sinusoidal Protuberances.....	55
4.3.2  Triangular Protuberances.....	60
4.3.3  Slot Protuberances .....	64
4.3.4  Effect of Distinct Airfoil Profiles .....	68
4.3.5  Reynolds Number effect.....	69
4.4  DYNAMIC STUDY .....	72
4.4.1  Baseline .....	72
4.4.2  Sinusoidal protuberances.....	74
4.4.3  Triangular protuberances .....	75
4.4.4  Slot protuberances .....	75
4.4.5  EFFECT OF PROTUBERANCES AT CONSTANT FREQUENCY .....	76
4.5  WORKING MECHANISM OF LEADING-EDGE PROTUBERANCES.....	77

4.5.1	Sinusoidal Protuberances .....	77
4.5.2	Triangular Protuberances.....	79
4.5.3	Slot Protuberances.....	81
4.6	FLOW VISUALIZATION .....	84
4.6.1	Smoke flow visualization.....	84
4.6.2	Tuft flow visualization .....	87
4.7	CONCLUSIONS.....	92
CHAPTER- 5 .....		95
EFFECT OF LEADING EDGE PROTUBERANCES ON THE PERFORMANCE OF SHAWT .....		95
5.1	SIZE OF THE WIND TURBINE.....	95
5.2	DESIGN OF WIND TURBINE BLADE.....	95
5.2.1	Blade shape .....	96
5.2.2	Geometry modelling.....	98
5.2.3	Fabrication of wind turbine blades.....	99
5.2.4	Wind Tunnel facility along with turbine testing unit.....	100
5.3	RESULTS AND DISCUSSION .....	102
5.3.1	Baseline wind turbine.....	102
5.3.2	Wind turbine with sinusoidal protuberance blades.....	103
5.3.3	Wind turbine with triangular protuberance blades .....	104
5.3.4	Wind turbine with slot protuberance blades:.....	105
5.4	PROTUBERANCES EFFECT ON COEFFICIENT OF PERFORMANCE.....	105
5.5	CONCLUSIONS.....	106
CHAPTER 6.....		107
CONCLUSIONS AND SCOPE FOR FUTURE WORK.....		107
6.1	CONCLUSIONS.....	107
6.2	SCOPE FOR FUTURE WORK.....	109
REFERENCES.....		111
LIST OF PUBLICATIONS.....		117
APPENDIX A .....		119
CURRICULUM VITAE.....		127



## LIST OF FIGURES

1.1	Wind energy installed capacity in India year on year(Ministry of Power 2022).	1
1.2	Wind turbine classification based on rotor diameter (Tummala et al. 2016).	3
1.3	The effect of Reynolds number on the maximum sectional lift to drag ratio of an airfoil ((Winslow et al. 2018) and (Mueller 1999)).	4
1.4	Sectional view of a laminar separation bubble (Horton 1968)	5
1.5	Achieving Oscillatory Blowing and Suction Using a Synthetic Jet with Zero Mass Flux (Moghaddam and Neishabouri, 2017)	7
1.6	Principle of operation of a Dimple actuator (Dearing <i>et al.</i> 2007).	7
1.7	Schematic of the synthetic jet actuator (Ramesh <i>et al.</i> 2009).	8
1.8	Examples of vortex generators and dimples on the suction side of an airfoil (Tiainen <i>et al.</i> (2017)).	8
1.9	Humpback Whale (left) and Whale Pectoral Flipper (right) (Corsini et al. 2013)	9
1.10	Stall stages on a wing or airfoil at various angles of attack (Shih et al., 1992)	11
1.11	Static polar is compared to the dynamic stall loop (Pechlivanoglou and Georgios (2013))	11
2.1	Top: A cross-section of a humpback whale's pectoral flipper. Bottom: NACA 634-021 airfoil profile.	16
2.2	Aerodynamics of a smooth Whale Flipper: (a)Lift coefficient, (b)Drag coefficient, (c)Lift to Drag Ratio and (d)Plan form area profile (Miklosovic et al. 2004)	17
3.1	Subsonic wind tunnel facility at National Institute of Technology Karnataka, India	29
3.2	Force balance calibration setup	31
3.3	Calibration curves	31
3.4	Coordinate data defining the shapes of airfoils SG6043 and E216.	33
3.5	Top view of three-dimensional models of the E216 airfoil baseline and protuberance	34
3.6	Various configurations of triangular protuberance models	35
3.7	Experimental airfoil models - (a) Manufactured through 5-Axis CNC Milling machine from Medium-Density Fiberboard wood and (b) 3-D Printed models	35

	using Polylactic Acid (PLA) material	
3.8	Airfoil mounting arrangement for static and dynamic study	36
3.9	(a) Total pressure tube rake inside the wind tunnel test section (b) close-up of the rake (c) boundary layer profile.	39
3.10	Schematic diagram of the experimental setup used for the Reynolds number effect and dynamic studies.	42
3.11	NEMA 23 stepper motor	42
3.12	(a) NI-9237 DAQ (b) NI-9401 DAQ	43
3.13	Smoke generator arrangement.	46
3.14	Tuft arrangement on airfoil surfaces for flow visualization and analysis	47
3.15	Computational domain and boundary conditions with a far field length of $10c$ .	48
3.16	Grid independence analysis for the E216 profile at $0^\circ$ angle of attack.	50
4.1	Numerical scheme validation for the E216 baseline airfoil (a) Lift coefficient (b) Drag coefficient, and (c) Lift to drag ratio	53
4.2	Experiment repeatability for the SG6043 baseline airfoil (a) Lift coefficient (b) Drag coefficient, and (c) Lift to drag ratio	55
4.3	The effect of sinusoidal protuberance wavelength on the aerodynamic parameters of an SG6043 airfoil with constant amplitude (a) Lift coefficient (b) Drag coefficient, and (c) Lift to drag ratio	56
4.4	The effect of sinusoidal protuberance wavelength on the aerodynamic parameters of an E216 airfoil with constant amplitude (a) Lift coefficient (b) Drag coefficient, and (c) Lift to drag ratio	57
4.5	Experimental results of the SG6043 baseline and the A9W64.5 sinusoidal protuberance model (a) Lift coefficient (b) Drag coefficient, and (c) Lift to drag ratio	58
4.6	The experimental results of the E216 baseline and the A9W64.5 sinusoidal protuberance model (a) Lift coefficient (b) Drag coefficient, and (c) Lift to drag ratio	59
4.7	The effect of triangular protuberance wavelength on the aerodynamic parameters of the SG6043 airfoil at constant amplitude (a) Lift coefficient (b) Drag coefficient, and (c) Lift to drag ratio	61
4.8	The experimental results of the SG6043 baseline and the A9W64.5 triangular	61

	protuberance model (a) Lift coefficient (b) Drag coefficient, and (c) Lift to drag ratio	
4.9	The effect of triangular protuberance wavelength on the aerodynamic parameters of an E216 airfoil with constant amplitude (a) Lift coefficient (b) Drag coefficient, and (c) Lift to drag ratio	63
4.10	The experimental results of the E216 baseline and the A9W64.5 triangular protuberance model (a) Lift coefficient (b) Drag coefficient, and (c) Lift to drag ratio	64
4.11	The effect of slot protuberance wavelength on the aerodynamic parameters of the SG6043 airfoil at constant amplitude (a) Lift coefficient (b) Drag coefficient, and (c) Lift to drag ratio	66
4.12	The experimental results of the SG6043 baseline and the A9W64.5 slot protuberance model (a) Lift coefficient (b) Drag coefficient, and (c) Lift to drag ratio	66
4.13	The effect of slot protuberance wavelength on the aerodynamic parameters of an E216 airfoil with constant amplitude (a) Lift coefficient (b) Drag coefficient, and (c) Lift to drag ratio	67
4.14	The experimental results of the E216 baseline and the A9W64.5 slot protuberance model (a) Lift coefficient (b) Drag coefficient, and (c) Lift to drag ratio	68
4.15	Effect of Reynolds number on the (a) baseline, (b) sinusoidal, (c) triangular, and (d) slot protuberance models.	70
4.16	Lift coefficient variation with angle of attack for baseline airfoil at various reduced frequencies.	73
4.17	Lift coefficient variation with angle of attack for sinusoidal airfoil at various reduced frequencies.	74
4.18	Lift coefficient variation with angle of attack for triangular airfoil at various reduced frequencies.	75
4.19	Lift coefficient variation with angle of attack for slot airfoil at various reduced frequencies.	76
4.20	Aerodynamic performance comparison of protuberance models with baseline at various reduced frequencies ( $k = 0.025, 0.05$ and $0.65$ )	77

4.21	Contours of vorticity magnitude for A4.5W64.5 configuration with sinusoidal protuberances at an angle of attack of 0°.	78
4.22	Counter-rotating vortices generated by A4.5W64.5 sinusoidal protuberances in a streamwise direction at an Angle of attack 0°.	78
4.23	(a) TKE contours at peak and trough regions at Angle of attacks 0° and 16° (b) Velocity contours at peak and trough regions at 16° angle.	79
4.24	Counter-rotating vortices are visualized at different streamwise slices for A4.5W64.5 configuration with triangular protuberances at 0° angle of attack.	80
4.25	Contours of TKE and velocity magnitude at peak and trough regions of A4.5W64.5 configuration with triangular protuberances at angles 0° and 18°.	80
4.26	(a) X vorticity contours at streamwise slices at 0° angle and (b) TKE contours at 0° and 16° taken at slot regions of A4.5W64.5 configuration with slot protuberances.	81
4.27	Comparison of pressure distributions of baseline and modified configurations at 0° and stall angles.	82
4.28	Experimental flow patterns observed using the smoke flow visualization for the SG6043 baseline.	85
4.29	(a) Secondary flow emerging from the trough region at 10° and (b) Merging of primary and secondary flows at 15° for SG6043 A9W64.5 Triangular model.	86
4.30	Streamline patterns of SG6043 A9W64.5 Slotted model with Angle of attack 0° (a) At non-slot region and (b) At slot region.	86
4.31	(a) Leading edge separation and (b) Formation of recirculation region behind the leading edge observed at Angle of attack 15°.	87
4.32	Visualisation of tuft patterns on a baseline airfoil at various angles of attack	88
4.33	Visualisation of tuft patterns on a sinusoidal airfoil at various angles of attack	89
4.34	Visualisation of tuft patterns on a triangular airfoil at various angles of attack	90
4.35	Visualisation of tuft patterns on a slot airfoil at various angles of attack	91
5.1	Section radius vs Chord and twist angle	97
5.2	Wind turbine blade design models: baseline and protuberance variants	98
5.3	Experimental models for SHAWT aerodynamic performance testing	99
5.4	Installation of wind turbine within the test section	100
5.5	Subsonic wind tunnel facility along with wind turbine test setup	101

5.6	Wind turbine parameter display unit	101
5.7	Validation of $C_P$ with TSR for baseline wind turbine	103
5.8	Variation of $C_P$ with TSR for wind turbine with sinusoidal protuberance blades	103
5.9	Variation of $C_P$ with TSR for wind turbine with triangular protuberance blades	104
5.10	Variation of $C_P$ with TSR for wind turbine with slot protuberance blades	105
5.11	Comparison of $C_P$ vs TSR for different turbines at a velocity 10m/s	106



## LIST OF TABLES

3.1	Airfoil profile geometrical parameters	33
3.2	Protuberance configurations and their terminology	34
3.3	Probe locations for measuring the boundary layer.	39
3.4	Smoke generator specifications	46
3.5	Grid Convergence Specifications	50
4.1	The aerodynamic performance of the E216 and SG6043 airfoils with sinusoidal protuberances.	56
4.2	The aerodynamic performance of the E216 and SG6043 airfoils with triangular protuberances.	60
4.3	The aerodynamic performance of the E216 and SG6043 airfoils with slot protuberances.	65
4.4	Aerodynamic parameters of E216 baseline and modified airfoils at 50K, 100K, and 150K Reynolds numbers	71
4.5	Comparison of chordwise pressure coefficient variation for various configurations at zero and stall angles of attack	83
5.1	Rotor design input parameters through BEMT	96
5.2	Determination of chord length and twist angle using BEMT	97
5.3	Technical specification of the parameter display unit	102
5.4	Technical specifications of generator unit	102



# NOTATION

## Roman Symbols

$A$	Amplitude of leading edge protuberance	[m]
$A_s$	Swept area	[m <sup>2</sup> ]
$B$	Number of blades	-
$c$	Mean chord	[m]
$C_l$	Coefficient of lift	-
$C_M$	Coefficient of moment	-
$C_N$	Coefficient of normal force	-
$C_p$	Coefficient of pressure	-
$C_d$	Coefficient of drag	-
$C_{l_{max}}$	Maximum coefficient of lift	-
$C_P$	Power coefficient	-
$D$	Drag force	[N]
$D_T$	Turbine diameter	[m]
$f$	Frequency	[Hz]
$k$	Reduced frequency	-
$k$	Turbulent kinetic energy	[J/kg]
$L$	Lift force	[N]
$(L/D)$	Lift to drag ratio	-
$(L/D)_{max}$	Maximum lift to drag ratio	-
$M$	Moment	[N-m]
$p$	Static pressure at chordwise location	[Pa]
$P$	Power output	[W]
$Re_c$	Chord-based Reynolds number	-
$Re_x$	Reynolds number based on distance	-
$s$	Span of blade	[m]
$U_\infty$	Free stream velocity	[m/s]
$V_w$	Wind velocity	[m/s]
$V_\infty$	Tunnel velocity	[m/s]
$W$	Wavelength of leading edge protuberance	[m]
$x$	Chordwise position	[m]
$y$	Spanwise position	[m]



## Greek Symbols

$\alpha$	Angle of attack	[°]
$\alpha_{\text{design}}$	Design angle of attack	[°]
$\beta$	Pitch angle	[°]
$\delta^*$	Boundary layer thickness	[mm]
$\eta$	Overall efficiency of wind turbine	[%]
$\theta$	Momentum thickness	[mm]
$\theta_T$	Twist angle	[°]
$\theta_P$	Pitch angle at any specific section	[°]
$\phi$	Relative angle	[°]
$\lambda$	Tip speed ratio	-
$\lambda_s$	Shape factor	-
$\mu$	Dynamic viscosity	[kg/m.s]
$\nu$	Kinematic viscosity	[m <sup>2</sup> /s]
$\omega$	Angular frequency	[rad/s]
$\omega$	Turbulent dissipation rate	[m <sup>2</sup> /s <sup>3</sup> ]
$\rho$	Density of air	[kg/m <sup>3</sup> ]
$\tau_{\text{blade}}$	Blade torque	[N-m]

## ABBREVIATIONS

AOA	Angle of Attack
BEMT	Blade Element Momentum Theory
CFD	Computational Fluid Dynamics
CNC	Computer Numerical Control
DAQ	Data Acquisition System
DSV	Dynamic Stall Vortex
FEA	Finite Element Analysis
LEV	Leading-Edge Vortex
MDF	Medium Density Fiberboard
NACA	National Advisory Committee for Aeronautics
PIV	Particle Image Velocimetry
PLA	Polylactic Acid Material
RANS	Reynolds Averaged Navier Stokes
RES	Renewable Energy Sources
RPM	Revolutions Per Minute
SST	Shear Stress Transport
SIMPLE	Semi-Implicit Method for Pressure-Linked Equations
SHAWT	Small Horizontal Axis Wind Turbines
TI	Turbulence Intensity
TKE	Turbulent Kinetic Energy
VG	Vortex Generators



# CHAPTER 1

## INTRODUCTION

Despite assurances from governments and major corporations worldwide to diminish greenhouse gas emissions, there's a prevailing trend of persisting with conventional energy sources rather than transitioning away from them. Although policymakers, civil society, and business leaders have initiated steps toward an energy transition, significantly more action is necessary to ensure these endeavors yield substantial results fast enough to prevent the most severe impacts of climate change. Projections indicate a substantial increase in global electricity demand ranging between 62 and 185% by 2050 compared to 2021. While the percentage of fossil fuels in the electricity mix is predicted to decrease from 59% in 2021 to approximately 55% by 2050. In contrast, more ambitious climate-focused scenarios envisage wind and solar power jointly surpassing the total electricity generation from all sources combined in 2021 by the year 2050. Meanwhile, in India, Wind Energy accounts for 34.06% of the total renewable energy capacity. According to reports from the department of non-conventional energy sources, it remains a primary contributor to clean energy. Figure 1.1 shows India's cumulative installed wind energy capacity from 2006-07 to 2022-23. Wind potential has consistently increased year after year, with a notable surge observed after 2016.

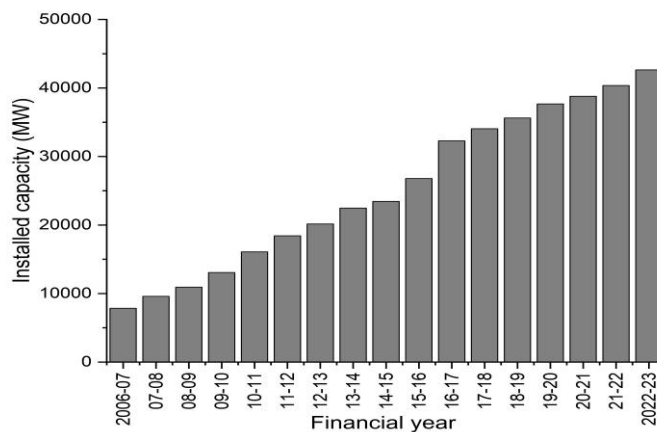


Figure 1.1: Wind energy installed capacity in India year on year (Ministry of Power 2022)

Notably, approximately 2 MW of power were added in 2006 and 2007, followed by a significant increase of 5400 MW in wind power capacity by 2016-17. In recent years, India's wind power generation capacity has increased substantially. As of December 31, 2023, the cumulative installed capacity of wind power reached 44.736 GW, making India the world's fourth-largest installed wind power capacity. The ambitious goal of achieving green energy relies heavily on utilizing the vast, but underutilized, potential of SHAWT. Low wind speeds, small rotor sizes, and issues with laminar separation are all common performance challenges for these turbines. Small wind turbines' power output and overall efficiency can be increased by improving the aerodynamic efficiency of their blades. Numerous active and passive techniques are available to improve turbine blades' aerodynamic performance. One such passive method is the use of leading edge modifications inspired by the tubercles found on Humpback Whales. These modifications have demonstrated the ability to improve aerodynamic performance by increasing the maximum lift coefficient and delaying stall. Despite its imposing size and sturdy body structure, the humpback whale has a remarkable ability for maneuverability. According to biologists, this agility can be attributed to the clever use of its pectoral flippers. These flippers have a distinct planform shape, exceptional flexibility, an elongated aspect ratio that spans up to one-third of the whale's body length, and prominent, sizable protuberances along their leading edges. The hypothesis of natural selection theory in evolutionary biology suggests that these protuberances serve an important function, contributing to the whale's survival abilities. Indeed, scientists hypothesize that these protuberances act as a form of flow control, critical to the whale's ability to secure prey.

The purpose of the dissertation is to investigate the potential performance enhancements provided by tubercles at low Reynolds numbers. Increased lift, lift to drag ratio and reduced drag are indicators of improved performance. Various protuberance shapes are studied in conjunction with an analysis of their three-dimensional effects.

## **1.1 SMALL SCALE WIND TURBINES**

The classification of wind turbines based on rotor diameter is illustrated in Figure 1.2, where large-scale wind turbines typically possess rotor diameters ranging from 50 to 100 meters and generate power between 1 to 3 MW. In contrast, SHAWT have rotor diameters spanning 3 to 10 m, with power capacities of 1.4 to 20 KW.

SHAWT with a nominal power rating of 50 watts tend to generate more expensive electricity than medium and large-scale turbines, particularly in windy areas. They do, however, serve well in applications that require high reliability, particularly in autonomous setups. These turbines can reliably produce energy when properly sized and used under optimal conditions, proving beneficial for socioeconomic growth, particularly in developing countries. Even in developed areas, these turbines can be valuable energy sources, particularly in remote areas without grid access.

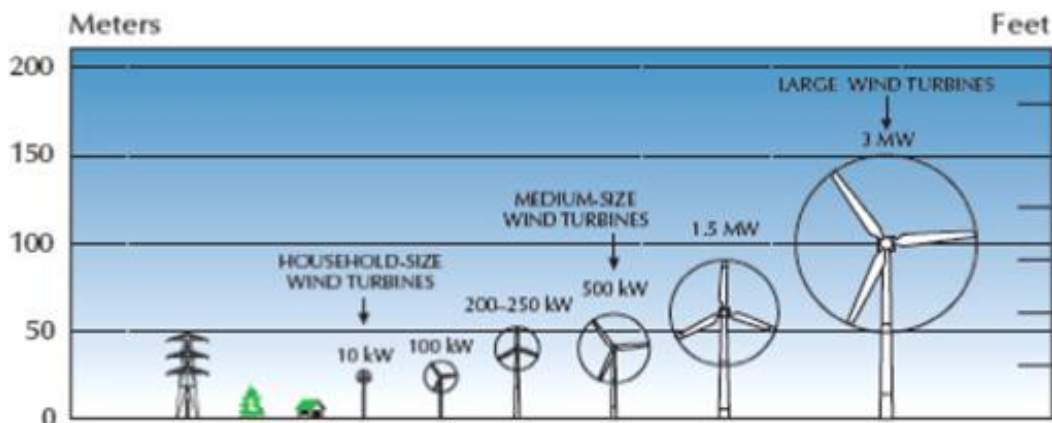


Figure 1.2: Wind turbine classification based on rotor diameter (Tummala *et al.* 2016)

The future growth potential of SHAWT is dependent on the cost-effectiveness of their generation. The initial cost per watt of power and the unit cost per kilowatt-hour (kWh) produced are important determinants. The SHAWT have the potential to become a significant source of power generation if these factors remain affordable.

## 1.2 LOW REYNOLDS NUMBER AERODYNAMICS

The Reynolds number is important in characterizing the balance of inertial and viscous forces in a fluid flow. Understanding the effects of the Reynolds number in the context of wind turbines is critical to optimize aerodynamic performance. Lower Reynolds numbers indicate viscous flows, which have a significant impact on the behavior of airflow around wind turbine blades. Higher Reynolds numbers, on the other hand, indicate a greater importance of inertial forces, which alters flow patterns and aerodynamic characteristics. The Reynolds number is a dimensionless quantity used to describe a fluid's flow regime. It is calculated using the equation 1.1 (Mueller, 1999).

$$Re = \frac{\rho U_{\infty} L}{\mu} \quad (1.1)$$

Where  $\rho$  represents the density of the air,  $L$  is a characteristic length, which is a scale of fluid motion related to the solid boundaries within the flow,  $U_\infty$  is the free stream velocity, and  $\mu$  is the dynamic viscosity of air.

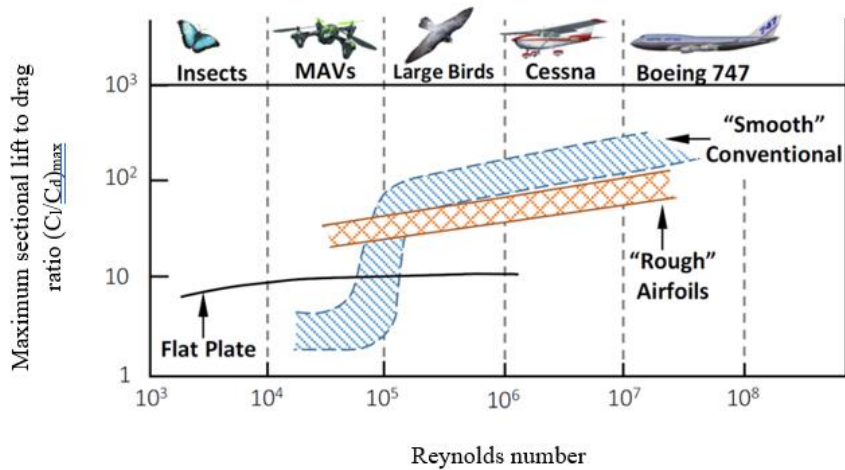


Figure 1.3: The effect of Reynolds number on the maximum sectional lift to drag ratio of an airfoil ((Winslow *et al.* 2018) and (Mueller, 1999)).

Figure 1.3 in the study shows how the Reynolds number affects the performance of airfoils. The airflow behaves differently when Reynolds number is low, as in tiny aeroplanes, mini drones, bird wings, and small insects like bees. Regular airfoils, on the other hand, perform best when Reynolds number is greater than  $10^6$ . These airfoils perform poorly at lower Reynolds number values. They cannot generate as much lift and cannot handle steep angles as well as when Reynolds number is higher. This means it's critical to figure out how to better manage airflow in order to generate more lift in situations with lower Reynolds number.

Airflows over wind turbine blades exhibit distinct behavior at lower Reynolds numbers. Flow separation and increased drag are caused by viscous forces, limiting the turbine's efficiency by reducing lift generation. This scenario is particularly relevant in smaller-scale wind turbines and in low-wind conditions.

Higher Reynolds numbers, on the other hand, demonstrate improved airflow stability and decreased viscous effects. This results in increased lift generation, decreased drag and improved overall aerodynamic performance of wind turbine blades. However, at extremely high Reynolds numbers, the transition to turbulent regimes may cause increased drag and unsteady flow patterns, reducing efficiency.

### 1.3 LAMINAR SEPARATION BUBBLE

Drag due to laminar separation bubbles formed under high adverse pressure also contributes significantly to total drag in low Reynolds number flows.

The airflow around an airfoil encounters regions with both favorable and adverse pressure gradients. A favorable pressure gradient occurs at the leading edge where pressure decreases along the flow direction. However, as the surface curvature changes, it leads to an adverse pressure gradient where static pressure increases downstream, causing a decrease in flow velocity. At a certain point, the airflow near the airfoil surface reverses direction compared to the free stream, leading to boundary layer separation.

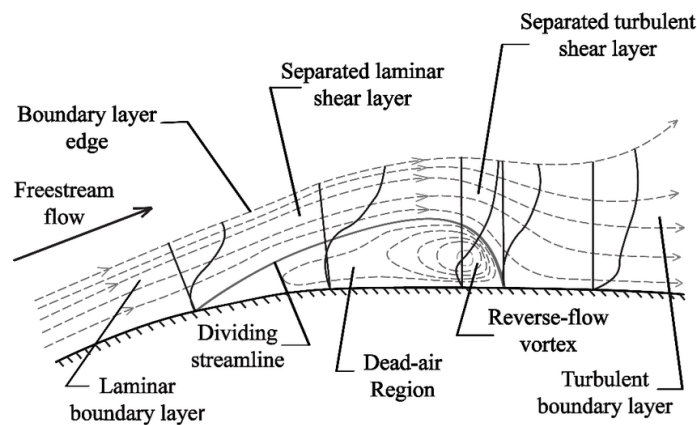


Figure 1.4: Sectional view of a laminar separation bubble (Horton, 1968).

In low Reynolds number conditions, the laminar flow in the free stream lacks sufficient energy to overcome the adverse pressure gradient, resulting in separation before transitioning to turbulent flow. The separated laminar boundary layer turns into turbulent flow, gaining energy through interaction with the main flow. If the turbulent flow gains enough energy, it can resist the adverse pressure gradient, reattaching to the surface (Walker, 1991). This process creates a recirculating dead air zone known as a laminar separation bubble (Jahanmiri, 2011), illustrated in Figure 1.4. The formation of laminar separation bubbles is common in SHAWT blades operating in low Reynolds number flows (Musial and Cromack, 1988).

The length of the separation bubble is significantly influenced by the Reynolds number. As the angle of attack increases, so does the adverse pressure gradient, causing the separation bubble to move towards the upstream direction. Additionally, the size of the leading edge radius plays a role in the formation of these bubbles. A smaller radius leads to a smaller bubble closer to the leading edge, often resulting in a sudden stall. Conversely, a larger radius

creates a separation bubble toward the rear part of the airfoil, leading to a more gradual stall at the trailing edge (Rodriguez and Rothan, 1993).

In enhancing the aerodynamic performance of low Reynolds number airfoils, minimizing the size of the separation bubble is crucial. The pressure drag associated with the laminar separation bubble can be reduced by employing effective flow separation control methods, as discussed below.

## **1.4 FLOW CONTROL TECHNIQUES**

Aerodynamic flow control techniques encompass a wide range of methods for altering airflow around objects such as aircraft, vehicles, or wind turbines to achieve specific aerodynamic goals. These active or passive techniques involve altering airflow dynamics to improve lift, reduce drag, manage separation, or increase efficiency. Active methods use actuators or jets to dynamically influence airflow, whereas passive methods use vortex generators or streamlined surfaces to modify airflow characteristics passively. Several active and passive flow control techniques are explained below.

### **1.4.1 Blowing and Suction**

Suction is the process of drawing fluid from the boundary layer to prevent separation upstream, whereas blowing is the process of introducing fluid into the boundary layer to increase its momentum. Blowing and suction can be controlled in two ways: continuously or periodically (oscillatory). High-energy fluid is injected near the surface during uniform blowing to increase boundary layer momentum. Direct injection of fluid raises boundary layer momentum tangentially, whereas normal blowing injects fluid perpendicular to the surface. However, using periodic blowing and suction, which involves intermittent surface action, proves to be more effective than the steady method. One method for achieving this periodic blowing and suction is to use a synthetic jet with zero mass flux as shown in Figure 1.5.

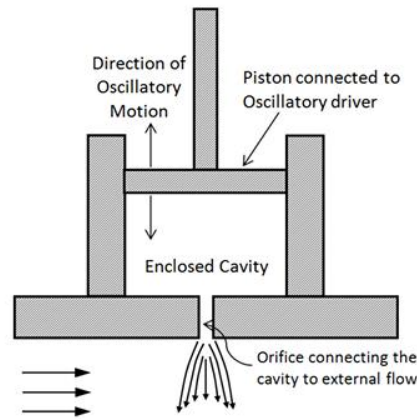


Figure 1.5: Achieving Oscillatory Blowing and Suction Using a Synthetic Jet with Zero Mass Flux (Moghaddam and Neishabouri, 2017)

#### 1.4.2 Dimple actuators or Electroactive polymer actuators

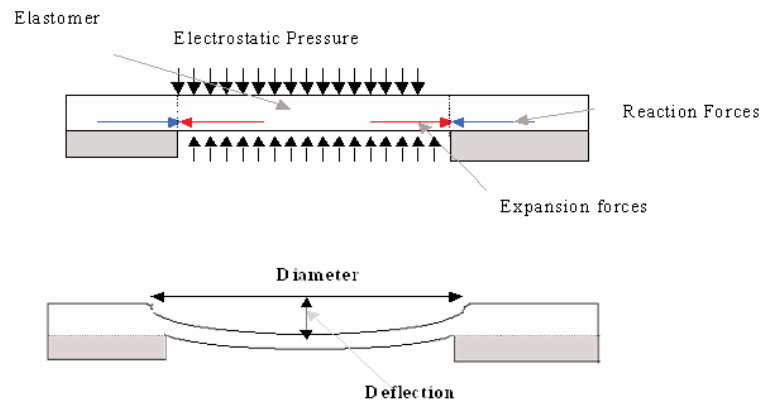


Figure 1.6: Principle of operation of a Dimple actuator (Dearing *et al.* 2007).

The development of electro-active polymers has enabled the creation of actuators with variable planforms that generate time-dependent depressions, or "dimples." These electro-active polymers' circular dimples have been used in experiments beneath laminar boundary layers, acting either as harmonic motion devices for open-loop control or as "on-demand" vortex generators. In the latter case, the dimple produces a single vortex of known strength for a specified duration. electro-active polymer actuators consist of an elastomer sandwiched between compliant electrodes, preferred over piezoelectric, electrostatic, and electromagnetic devices due to their simplicity, good electro-mechanical coupling efficiency, and low weight. When bonded to a substrate, the lateral motion at the edge of the dimple is constrained, resulting in out-of-plane buckling when voltage is applied, as shown in Figure 1.6.

### 1.4.3 Synthetic jet actuators

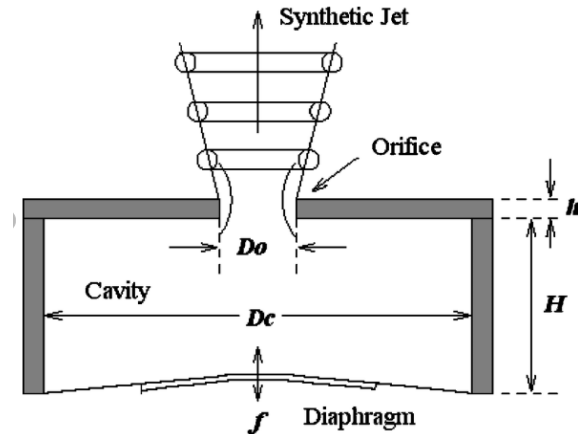


Figure 1.7: Schematic of the synthetic jet actuator (Ramesh *et al.* 2009).

Among various types of active flow control methods, oscillatory blowing using synthetic jets shows great promise in low Reynolds number flow regimes. The advantage of using synthetic jets as flow control devices is that they require no external air supply, eliminating the need for piping, connections, and compressors associated with conventional jets. The schematic of the present configuration using piezo stack is shown in Figure 1.7.

### 1.4.4 Vortex generators

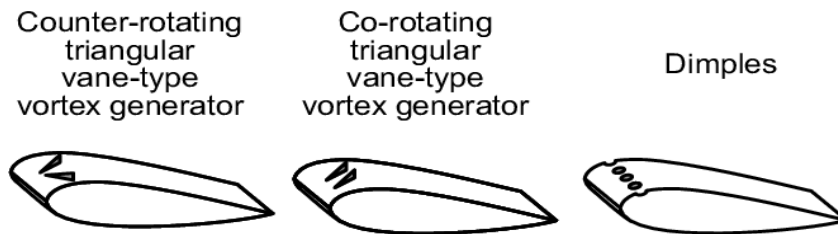


Figure 1.8: Examples of vortex generators and dimples on the suction side of an airfoil (Tainen *et al.* (2017)).

A vortex generator (VG) is a small aerodynamic device attached to lifting surfaces, such as aircraft wings or wind turbine rotor blades, to delay flow separation. Typically placed near the leading edge, VGs help maintain steady airflow over the trailing edge control surfaces. They are usually rectangular or triangular, positioned to create a tip vortex that draws fast-moving external air into the slower boundary layer, making it turbulent and less likely to separate. Vortex generators are commonly seen on the wings and vertical tails of many airliners to enhance the effectiveness of control surfaces. Counter-rotating and co-rotating triangular

vane-type vortex generators, along with dimples on the suction side of the airfoil, can be seen in Figure 1.8.

#### 1.4.5 Tubercles or Leading edge Protuberances

Leading edge tubercles, inspired by the humpback whale's pectoral fins shown in Figure 1.9 are small, scallop-shaped protuberances placed asymmetrically along the leading edge of airfoils or hydrofoils.



Figure 1.9: Humpback Whale (left) and Whale Pectoral Flipper (right) (Corsini *et al.* 2013)

Leading edge tubercles significantly enhance aerodynamic and hydrodynamic performance compared to other flow control techniques. They induce stall delay, allowing airfoils to maintain lift at higher angles of attack, increasing lift and reducing drag, especially in low Reynolds number flows. Unlike active methods, which require an energy source and are complex to design and operate, and other passive techniques like vortex generators, which are difficult to design and fix over blades, tubercles are a simpler passive solution that improves low-speed performance and reduces noise. Their versatility and adaptability make them a cost-effective and efficient option for various applications. Tubercle characteristics such as size, shape, and positioning have been extensively studied to understand their impact on flow behaviour. Tubercles' ability to manage flow separation, control vortices, and reduce drag by redistributing pressure gradients along the airfoil surface has been revealed by computational simulations and wind tunnel experiments.

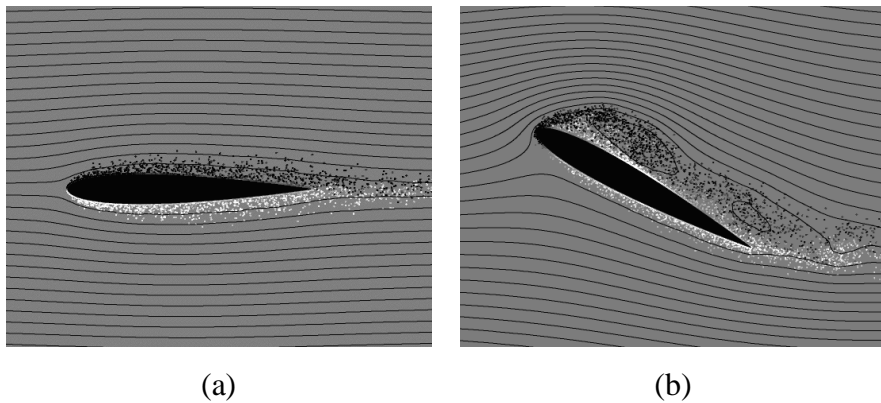
Furthermore, research into the use of tubercles in a variety of industries, including aerospace, wind energy, and marine propulsion, has yielded promising results. According to these findings, incorporating tubercles into airfoil and hydrofoil designs has the potential to

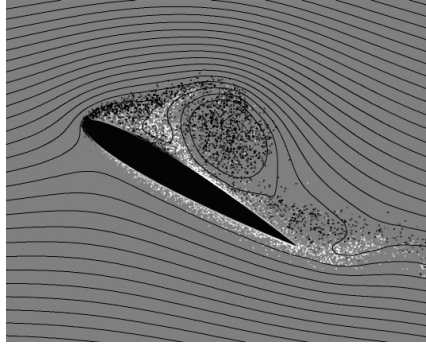
significantly improve performance metrics, resulting in more efficient and maneuverable systems.

## 1.5 STALL

A stall occurs in aerodynamics when the angle of attack on an airfoil or wing exceeds a specific threshold, resulting in a decrease in lift and a rapid increase in drag due to flow separation. This critical angle of attack varies depending on factors such as the cross-section of the airfoil or wing, its design, and its aspect ratio. This critical angle is typically between 8 and 20° relative to the incoming wind direction for most subsonic airfoils.

Figure 1.10 illustrates the airflow over the cross-section of a stalling wing. At very small angles of attack (Figure 1.10(a)), the vortices within the boundary layer remain close to the wing until they are carried downstream. During this stage, the wing generates substantial lift with minimal drag. As the angle of attack increases (Figure 1.10(b)), the boundary layer vortices detach from the wing surface near the leading edge. Consequently, the incoming airflow doesn't completely curve around the leading edge, resulting in a stalled wing and significant drag. Despite this, a considerable amount of lift remains as the separated vortices hover above the wing. However, as the angle of attack continues to increase, causing the separated vortices to be blown down the trailing edge (Figure 1.10(c)), the lift diminishes significantly.





(c)

Figure 1.10: Stall stages on a wing or airfoil at various angles of attack (Shih *et al.* 1992)

## 1.6 DYNAMIC STALL

Static stall relates to the behavior of an airfoil at a fixed angle of attack, whereas dynamic stall involves changes in the airfoil's angle of attack over time. Dynamic stall introduces hysteresis effects, which cannot be captured through static polars, resulting from the oscillating angle of attack in the airfoil model shown in Figure 1.11. This dynamic stall model creates a loop of hysteresis around the maximum lift coefficient ( $C_{lmax}$ ) and post-stall regions. This loop extends dynamically beyond the limitations of static polars (Pechlivanoglou, 2012). The dynamic stall concept computes revised values that represent an exchange of lift and drag coefficient values with those from the static polars.

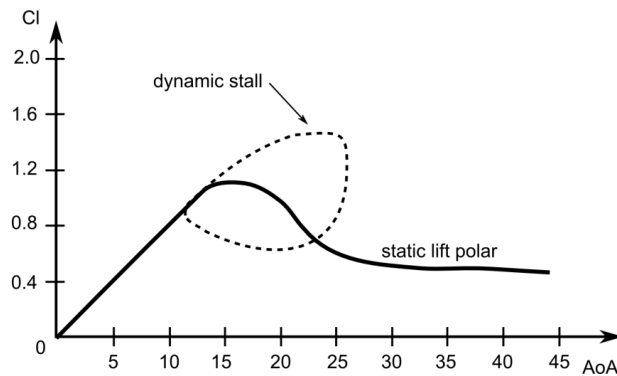


Figure 1.11: Static polar is compared to the dynamic stall loop (Pechlivanoglou, 2012)

A comprehensive comprehension of the dynamic mechanisms associated with stall is necessary to effectively prolong the stalled process (Francis and Keesee, 1985). Research by Ham and Garelick (2009) identified that swift pitching movements of airfoils could generate additional lift, attributed to a vortex created during the airfoil's unsteady motion. Equation 1.2 depicts the instantaneous angle of attack for an airfoil experiencing dynamic stall.

$$\alpha = \alpha_0 + \alpha_m \sin(\omega t) \quad (1.2)$$

Where  $\alpha$  is the instantaneous angle of attack ( $^\circ$ ),  $\alpha_0$  is the mean angle of oscillations ( $^\circ$ ),  $\alpha_m$  is the amplitude of oscillations ( $^\circ$ ),  $\omega$  is the angular frequency (rad/s), and  $t$  is the time interval (sec).

In the context of unstable aerodynamics and aeroelasticity, the reduced frequency ( $k$ ) serves as a dimensionless parameter that characterizes the level of unsteadiness in aerodynamic scenarios. It quantifies the frequency of the sine wave motion, as expressed in equation 1.3 (Pechlivanoglou, 2012).

$$k = \frac{\omega \frac{c}{2}}{U_\infty} = \frac{\pi f c}{U_\infty} \quad (1.3)$$

Where  $\omega$  is the angular frequency (rad/s),  $c$  is the chord of the airfoil (m),  $U_\infty$  is the free stream velocity (m/s), and  $f$  is the frequency (Hz).

For values where  $0 < k < 0.05$ , the situation is deemed quasi-steady, while  $k \geq 0.05$  indicates an unsteady state.

Flow separation on rotating wind turbine blades leads to an important consequence known as dynamic stall. This phenomenon occurs due to the unsteady behavior of an airfoil when it operates beyond its critical stall angle.

The formation and evolution of the Dynamic Stall Vortex (DSV) are considered crucial aspects of the dynamic stall process. Extensive studies by (Carr *et al.* 1977)(Carr 1988)(Carr *et al.* 1983)(Monterey, 1993) have significantly contributed to understanding DSV and dynamic stall. Preceding the onset of dynamic stall, a region of reversed flow forms at the trailing edge. This reversed flow area gradually progresses towards the leading edge under the influence of an adverse pressure gradient while remaining attached to the surface. This process leads to the creation of a leading-edge vortex (LEV) at the airfoil's front, generating strong suction. The LEV eventually separates from the surface, forming the DSV. As the angle of attack increases, the DSV moves towards the trailing edge and eventually separates from it.

During dynamic stall, there is an observed increase in the airfoil's lift during pitch-up, particularly at high reduced frequencies. This lift increase is often linked to the formation of

the DSV. However, as the vortex moves downstream, there's a sudden drop in the airfoil's lift, leading to a state known as deep stall.

## **1.7 SCOPE OF PRESENT WORK**

The investigation of leading edge protuberances is motivated by their potential to improve aerodynamic performance via mechanisms that delay airflow separation and stall, thereby improving lift and lowering drag. Understanding pressure distributions, boundary layer behavior, and flow separation patterns are all part of the investigation of these protuberances. This study seeks to understand how these changes affect aerodynamic force coefficients, to optimize airfoil performance under various conditions such as low Reynolds numbers and different angles of attack under static and dynamic condition. Finally, this investigation explores the possibility of improving the power coefficient ( $C_P$ ) of wind turbine fitted with blades incorporating these protuberances.

## **1.8 OVERVIEW OF THE THESIS**

This thesis investigates the impact of leading edge protuberances on the aerodynamic performance of airfoils at low Reynolds numbers, specifically within the context of small horizontal axis wind turbines (SHAWT). Chapter 1 introduces the study's significance, focusing on the effects of low Reynolds numbers on airfoil performance and the potential benefits of leading edge protuberances in both static and dynamic conditions. Chapter 2 provides a thorough literature review, identifying research gaps and examining previous studies on low Reynolds number effects and the role of leading edge protuberances in enhancing aerodynamic performance. Chapter 3 details the research methodology, including the experimental and numerical models, airfoil fabrication, and testing procedures. Chapter 4 presents and discusses the results from numerical simulations and experimental investigations, highlighting the influence of various leading edge shapes, wavelengths, amplitudes, Reynolds numbers, and reduced frequencies on airfoil performance, along with the use of smoke and tuft flow visualization techniques to understand airflow patterns. Chapter 5 focuses on the effect of leading edge protuberances on SHAWT performance, describing the methodology and experimental studies comparing baseline and protuberance blades. Finally, Chapter 6 consolidates the findings, offering conclusive insights on the impact of low Reynolds numbers on airfoil aerodynamics and the role of leading edge protuberances in enhancing SHAWT performance.



## CHAPTER 2

### LITERATURE REVIEW

The literature review in this thesis is divided into four major sections. It begins by delving into the aerodynamic impact experienced by airfoils operating in scenarios with low Reynolds numbers. Following that, it lists various literature sources that investigate various types of tubercles and their effects on aerodynamic performance under both static and dynamic conditions. The third section examines various flow visualization techniques reported in the literature. In the fourth section, the effect of leading edge protuberances on the aerodynamic performance of SHAWT literature is presented. Finally, it discusses the motivation for the study and clearly outlines the current research objectives.

#### 2.1 REYNOLDS NUMBER EFFECTS

Recognising the Reynolds number is critical when dealing with three-dimensional effects. Notably, lift enhancement through tubercles was observed in studies with Reynolds numbers ranging from 500K to 631K ((Miklosovic *et al.* 2004) (Miklosovic *et al.*, Pedro and Kobayashi, 2008), specifically on model Humpback whale flippers. This demonstrates the effectiveness of tubercles when applied to this particular geometry.

In contrast, Weber *et al.* (2010) discovered that applying tubercles to rudders resulted in decreased performance for Reynolds numbers ranging from 200K to 880K. Notably, this was the only study conducted in water at such high Reynolds numbers, and the decline in performance could be attributed to increased cavitation caused by lower pressure in the troughs.

Furthermore, Stanway (2008) obtained results in the low Reynolds number range of 44K to 120K. All tests except for Reynolds number 120K showed a decrease in maximum lift coefficient. These findings indicate that tubercle-related poor performance in model Humpback whale flipper simulations is uncommon, emphasising the importance of Reynolds number effects.

Miklosovic *et al.* (2007) found that tubercles improved performance on a model whale flipper but reduced performance on a full-span rectangular planform. They concluded that tubercles provided a three-dimensional advantage that was beneficial to the model flipper but not used

by full-span models. The difference in Reynolds numbers, with the model flipper at Reynolds number 534K to 631K and the full-span case at Reynolds number 274K to 277K, may explain the different performance characteristics, though this was not explicitly stated in the article.

## 2.2 EFFECT OF TUBERCLES ON AIRFOIL PERFORMANCE

### 2.2.1 Static study

Watts and Fish (2001) research highlights the remarkable agility of humpback whales despite their considerable size, discussing the whales' ability to perform intricate maneuvers and tight turns, particularly during hunting pursuits. Their study focuses on the unsteady movements of aquatic creatures, emphasizing the humpback whale's unique mobility attributed to its distinctive pectoral flippers, as depicted in Figure 2.1.

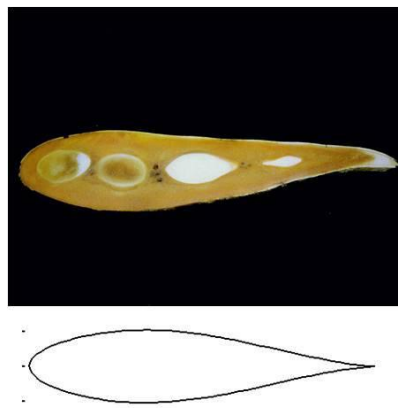


Figure 2.1: Top: A cross-section of a humpback whale's pectoral flipper. Bottom: NACA 634-021 airfoil profile.

Biologists suggest that the protuberances positioned along the leading edge of these flippers are potentially employed by humpback whales as a means of passive flow control or reducing drag during extreme maneuvers like bubble netting, setting them apart from other species in terms of maneuverability.

Figure 2.2 depicts lift and drag data for the scalloped whale flipper model, with the solid lines in (A), (B), and (C) representing the average of data from wind tunnel experiments using the smooth flipper model for comparison. (A) Measurement of the lift coefficient  $C_l$  in a wind tunnel as a function of angle of attack. It is worth noting that the scalloped geometry retains lift at greater angle of attack than the smooth model. (B) The drag coefficient  $C_d$  as a function of angle of attack. (C) L/D aerodynamic efficiency (D) Idealised scalloped model profile

(solid line) superimposed on actual whale flipper profile (dotted line). These measurements show that the scalloped model delays stall and gives a 40% improvement over the smooth model's stall angle (Miklosovic *et al.* 2004).

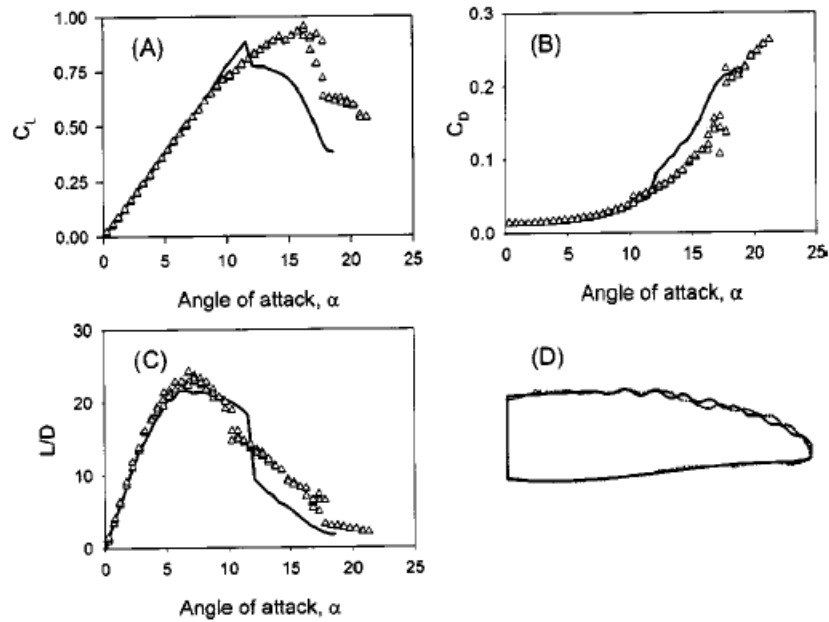


Figure 2.2: Aerodynamics of a smooth Whale Flipper: (a)Lift coefficient, (b)Drag coefficient, (c)Lift to Drag Ratio and (d)Plan form area profile (Miklosovic *et al.* 2004)

By examining the hydrodynamic performance of flippers enhanced with leading edge tubercles, an analogy was drawn to vortex generators. As a result, it may provide an alternative to vortex generators for low Reynolds number aerial and underwater vehicles.

The humpback whale flipper is characterized by a relatively large aspect ratio ( $b/c=6$ ), featuring substantial protuberances along its leading edge. Generally, the flipper's cross-section exhibits a symmetric shape with a rounded leading edge and a sharp trailing edge. These protuberances along the leading edge differ in both amplitude and wavelength across the span of the flipper. Amplitudes of these protuberances range between 2.5% to 12% of the chord length, while wavelengths vary from 10% to 50% of the chord length. Additionally, the thickness ratio changes along the span, with the maximum thickness ranging from  $0.20c$  to  $0.28c$  and averaging at  $0.23c$ , diminishing from mid-span to the tip. The location of maximum thickness ratio ranges between  $0.20c$  to  $0.40c$ . Fish *et al* (2011) have identified that the cross-section of the flipper resembles a NACA 634-021 airfoil profile.

Hansen *et al.* (2011) used an open circuit wind tunnel to evaluate the performance of two NACA airfoils with different aerodynamic characteristics and sinusoidal leading-edge protrusions. It was discovered that decreasing tubercle amplitude leads to a higher maximum lift coefficient and larger stall angle, whereas in the post-stall regime, larger amplitude tubercles performed better, and decreasing wavelength leads to improvements in all aspects of lift performance, including maximum lift coefficient, stall angle, and post-stall characteristics.

Johari *et al.* (2007) conducted experimental investigations on sinusoidal protuberances positioned at the leading edge of two-dimensional NACA 63-021 airfoils. Their study revealed that airfoils with these protuberances exhibited a 50% increase in lift coefficients and drag coefficients in the post-stall regime, regardless of the leading edge geometry, when compared to the baseline foil. However, in the pre-stall regime, there was a reduction in lift coefficient and an increase in drag coefficient. Additionally, it was observed that the amplitude of the protuberances significantly influenced the resultant forces and moments.

Weber *et al.* (2011) used commercial CFD codes to simulate the flow of a humpback whale flipper model. Their research demonstrated both the benefits and limitations of using CFD to explain experimental results. In these codes, Reynolds-Averaged Navier-Stokes (RANS) equations were used. Flow visualizations indicated differing stall patterns between the smooth and tubercle flippers, with the smooth flipper experiencing primarily trailing-edge stall, while the tubercle flipper tended to stall in the troughs first. Pressure contours varied, showcasing low pressures and substantial gradients in the troughs of the tubercle flipper. The tubercle flipper demonstrated a capacity for achieving a larger post-stall lift coefficient due to maintained flow attachment along its span, facilitated by the presence of tubercles.

Pedro and Kobayashi (2008) used the detached eddy simulation model because it has a higher accuracy in the stall region, but a higher computational cost when compared to Reynolds Avaraged Navier Stokes (RANS) approach. The results showed superior aerodynamic efficiency of scalloped flippers is attributed to stream-wise vortices induced by tubercles. These vortices delay trailing-edge separation by carrying momentum to the boundary layer and confine leading edge separation to the tip region.

On the other hand, Stanway (2008) employed Particle Image Velocimetry (PIV) measurements to analyze the velocity field over a static foil featuring tubercles. Investigating both static and dynamic foils with tubercles, Stanway observed that while tubercles improved

performance in static foils by delaying stall, they adversely affected the performance of flapping foils. The force measurements conducted on a flapping foil indicated a degradation in performance. Stanway concluded that the presence of tubercles delayed stall in static foils, elucidating why humpback whales possess them on their pectoral flippers rather than on their flukes.

The vortical flow caused by the scalloped leading edge had different effects when compared to traditional vortex generators. Pre-stall lift loss was significantly lower (81% less) for a semispan wing than for a full-span wing, and poststall gains were significantly higher (65% increase). The semispan wing experienced 88% less prestall moment loss and 40% less poststall gain than the full-span wing. In conclusion, the vortical flow induced by the sinusoidal leading edge reduced the effectiveness of a full-span wing by causing early separation, but improved the performance of a half-span wing by preventing spanwise stall progression, thereby extending its operational capabilities while incurring minimal performance costs, as demonstrated by Miklosovic *et al.* (2007) experiments.

Zhao *et al.* (2023) study uses Large Eddy Simulation to analyse the flow field around a NACA 0021 airfoil with and without tubercles at Reynolds number of 120K. Three tubercle amplitudes (2 mm, 4 mm, and 8 mm) are compared. The study found that larger amplitudes delay flow separation by increasing momentum transfer, resulting in better aerodynamic performance. Furthermore, both amplitude and wavelength have a significant impact on the formation of Large-Scale coherent structure at troughs, which helps with flow reattachment and aerodynamic performance. The analysis of aerodynamic lift fluctuations associated with Karman vortices reveals a strong relationship between dominant proper orthogonal decomposition modes and vortex shedding. The study concludes that increasing tubercle amplitude exacerbates the destruction of spanwise coherent structures.

### **2.2.2 Dynamic study**

Experiments (Leishman, 1990) on the NACA 23012 aerofoil revealed that static stall was caused by abrupt trailing edge separation, with the abruptness increasing as the Reynolds number increased. However, separation always began near the leading edge under dynamic conditions, and low oscillation frequencies could prevent trailing edge separation, converting the stall mechanism to a leading-edge type stall. Overall, dynamic stall behaviour was similar to that of other airfoils, with significant increases in lift and pitching moment caused by

vortex shedding from the leading edge during dynamic stall. Secondary vortex shedding was blamed for secondary loading peaks, especially at low Mach numbers. Surface flow reversals were predicted by boundary layer measurements prior to significant flow separation.

Ozen and Rockwell (2010) found that altering the leading-edge shape, whether straight or sinusoidal, has minimal impact on the tip vortex shape, even at relatively low Reynolds numbers. Although their study focused on low Reynolds numbers, they propose that the identified flow mechanisms are likely applicable to higher Reynolds numbers, particularly in scenarios involving sharp, slender leading edges, and wings flapping at increased reduced frequencies. They suggest future investigations should encompass a broader range of Reynolds numbers, considering diverse wing motions. In essence, a sinusoidal leading edge effectively controls flow structures in inboard areas of flapping wings, with potential applications across various wing motions, including revolving or rotating wings characterized by prevalent spanwise flow.

Holst *et al.* (2019)<sup>a</sup> conducted an investigation involving a sinusoidal pitching airfoil across an incidence range of  $5^\circ$  to  $25^\circ$ , utilizing lower frequency ( $k=0.025$ ) and higher Reynolds number for stability assessment. Although CFD slightly underestimated the maximum lift, the hysteresis loop width aligned well. Reattachment was predicted to occur slightly earlier than the static polar. Additionally, the study encompassed a  $10^\circ$  to  $30^\circ$  movement using a higher reduced frequency ( $k=0.05$ ) and Reynolds number 80K, revealing that numerical stall occurred slightly prior to experimental observations, resulting in premature lift reduction during pitch up and instability. The RANS approach encountered challenges in modeling the post-stall flow but offered a basic estimate of the maximum lift location.

According to Wei *et al.* (2021), the physics of the DSV is closely related to dynamic stall, which has a significant effect on the aerodynamic performances of dynamic airfoils. The physics of the DSV on the NACA 0012 airfoil were investigated experimentally using unsteady pressure measurements with high time precision. At Reynolds number 150K was the experimental Reynolds number, and  $k=0.069$  was the reduced frequency. The unsteady pressure field propagation during the dynamic stall process was thoroughly investigated. The DSV's motion characteristics, including near-wall development characteristics and near-wall evolution velocity, were investigated. Furthermore, wavelength analysis combined with proper orthogonal decomposition technology was used to investigate the frequency

characteristics of the near-wall DSV. Furthermore, the effects of the mean angle of attack and amplitude on the DSV motion and frequency characteristics were thoroughly investigated. The effects of mean angle of attack on near-wall DSV strength and propagation velocity were linear, whereas amplitude effects were nonlinear. At the beginning of the DSV development ( $x/c=0.10-0.20$ ), the mean angle of attack and amplitude had a significant influence on the frequency of the LEV.

Holst *et al.* (2019)<sup>b</sup> study investigates static and dynamic sinusoidal pitching configurations across two Reynolds numbers 140K and 180K, encompassing near stall, post stall, and deep stall incidence ranges. The research delves into bi-stable flow phenomena utilizing high-frequency measurements, unveiling substantial lift fluctuations in post and deep stall regimes surpassing the maximum lift of static polars and not captured by averaged measurements. Detailed surface pressure distributions are analyzed to enhance understanding of flow conditions and pressure development during dynamic motion. Notably, the high-resolution dynamic experiments reveal lift fluctuations exceeding  $C_{lmax}$  of the static polar in the post-stall regime, with even larger fluctuations observed beyond  $120^\circ$  of angle of attack. Although this angle of attack range is unlikely during wind turbine operation, it could induce oscillations during standstill under changing wind directions.

Wei *et al.* (2019) investigated the behavior of the S809 airfoil during oscillation by utilizing pressure signatures to assess transition and separation events. Notably, fixed transition analysis showed no distinct transition peaks downstream of roughness, indicating effective turbulence induction by the transition strip in the flow. Separation and reattachment also showcased a marked hysteresis effect, notably influenced by the reduced frequency; higher frequencies advanced flow separation and delayed reattachment, amplifying hysteresis. The study revealed varying mechanisms governing flow transition/relaminarization and separation/reattachment during airfoil pitching oscillation. Hysteresis in aerodynamic forces stemmed primarily from transition/relaminarization at smaller angles of attack and separation/reattachment at larger angles. Moreover, an increase in oscillation frequency within the studied range heightened the hysteresis effect on  $C_l$ , resulting in a rise in  $C_{lmax}$  from 1.24 to 1.55 and an elevation in the stall angle of attack from  $11.54^\circ$  to  $14.95^\circ$  as the reduced frequency increased from  $k = 0.0785$  to  $k = 0.2356$ .

Zhu *et al.* (2023) study looks into the effects of Reynolds number and reduced frequency on the performance and dynamic stall behaviour of a vertical axis wind turbine with a tip speed ratio of 1.5. Using URANS simulations with transitional turbulence modelling, the study discovers that overall vertical axis wind turbine power performance is primarily influenced by blade aerodynamic responses during dynamic stall, particularly on the upwind side. Increasing the Reynolds number significantly improves power performance by delaying dynamic stall onset and altering stall behaviours. Increasing the reduced frequency improves power performance by delaying stall onset and dampening dynamic stall vortex movement. The study emphasises the impact of high Reynolds number and reduced frequency on dynamic stall behaviours, which improves vertical axis wind turbine performance without the use of external equipment.

## **2.3 FLOW VISUALIZATION STUDY**

### **2.3.1 Tuft flow visualization**

In a water tunnel study by Johari *et al.* (2007) examining sinusoidal protuberances on NACA 634-021 airfoils, protuberance amplitudes ranged from 2.5% to 12% of the mean chord length, with spanwise wavelengths mirroring those of a humpback whale's flipper (25% to 50% of the mean chord length). The tuft flow visualization indicated attached flow over the protuberances post baseline airfoil stall at the angle of attack. Predominant flow separation occurred in troughs between adjacent protuberances, with minimal impact observed from protuberance wavelength on flow separation. In his investigation of various foils with leading-edge protuberances at different angles of attack (12°, 18°, and 24°) revealed flow separation originating in troughs between these protuberances. As angle of attack increased, the baseline foil exhibited augmented separated flow, while foils with protuberances sustained attached flow over their surfaces even in the post-stall regime at 24°. Foils featuring protuberances displayed higher lift coefficients compared to fully stalled baseline foils, affirming the effectiveness of protuberances in delaying stall and enhancing lift performance. Surface tuft visualizations demonstrated persistent attached flow over the protuberances following baseline airfoil stall, while flow separation mainly occurred in the troughs between modified foil protuberances, with negligible impact from protuberance wavelength on flow separation.

De Paula *et al.* (2016) study, employing tuft and oil flow visualization techniques, observed that at lower angles of attack, all NACA 0012 airfoil configurations retained attached flow on their upper surfaces. Flow separation onset occurred at the trailing edge of the smooth configuration at a  $10^\circ$  angle of attack, while wavy configurations exhibited varying degrees of separation. Notably, at a  $15^\circ$  angle of attack, the smooth configuration encountered extensive flow separation, contrasting with diverse separation characteristics observed in wavy configurations. As the angle of attack increased to  $20^\circ$ , the smooth configuration underwent full flow separation over its upper surface, signifying entry into the post-stall regime, while wavy configurations demonstrated varying levels of flow separation and lift behavior.

Broeren and Bragg (2001) reported mini-tuft photographs captured at angles slightly beyond the stall angles for the Ultra-Sport and NACA 2414 airfoils, indicating a non-integer number of stall-cell patterns, approximately 1.4-1.5. These patterns corresponded to those observed in the NACA 0015 airfoil at a different angle of attack. Notably, the key distinction observed was that boundary-layer separation did not extend to the leading edge of the current airfoils within the main stall cell.

### **2.3.2 Smoke flow visualization**

Mueller and Batill (1980) study detail the smoke-wire flow visualization technique, discussing its method, equipment, and its impact on the undisturbed flow field. It specifically applied this technique to examine the transition of the free shear layer linked to the laminar separation bubble on a low Reynolds number NACA 663-018 airfoil section. The study showcased how the smoke-wire technique effectively introduced smoke streak lines into the flow field, offering valuable visualization for understanding complex flow phenomena.

The smoke visualization images presented the flow characteristics of the three airfoils, marking flow separation points with arrows and delineating separated areas with dotted lines (Fan *et al.* 2022). Comparatively, the two modified airfoils exhibit improved suction side flow field structures in contrast to the reference airfoil. At angle of attack  $5^\circ$ , the influence of the tubercles on the flow field appears subtle and challenging to discern visually. Yet, as the angles of attack increase towards angle of attack  $15^\circ$ , near the stall angles of attack, the spanwise flow characteristics of the modified airfoils become more evident. The tubercles impact on the flow field is highlighted, observed through clearer delineation and separation points of the flow separation area. In mod-1, flow separation occurs later compared to the

reference airfoil at a specific cross-section, extending to a distance of  $0.5c$  instead of  $0.4c$ . Passing through the trough section, the incoming flow expands the separation area. For mod-2, the flow field structure closely resembles that of mod-1.

## **2.4 WIND TURBINES WITH LEADING EDGE PROTUBERANCES**

Huang *et al.* (2015) conducted experimental research to determine the effect of Leading edge protuberances on the aerodynamic performance of SHAWT. Their static 3D blade analysis indicated that changes in the tubercle's wavelength and amplitude could affect aerodynamic performance. The tests on rotating turbine models showed that tubercles effectively delayed stall, improving turbine performance, especially at low Tip Speed Ratios (TSR).

Ng *et al.* (2017) used numerical analysis to investigate the role of leading edge protuberances in the fatigue life of SHAWT blade. Their research revealed that blades with tubercles occupying varying percentages of the leading-edge span (from 20% to 95%) had a 6% reduction in flapwise root-bending moment compared to the unmodified configuration. Furthermore, the torsional moment decreased by 17% due to reduced leading-edge suction along tubercle crests that were further away from the elastic axis. Tubercle positioning was critical: placing tubercles close to the blade tip improved performance during stall episodes caused by large tip deflections, resulting in a significant increase in root-bending moment due to a larger moment arm and faster relative flow. Conversely, positioning tubercles near the blade root showed little effect on fatigue responses, despite this region being prone to stall at low speeds.

Siram *et al.* (2022) addressed the necessary procedures for the creation of four model turbine rotors made up of E216, SG6043, NACA63415, and NACA0012 airfoils, beginning with aerofoil selection and progressing to blade design and analysis using blade element momentum theory (BEMT). In comparison to the other three models, this study shows that the model rotor with the E216 airfoil has better performance. However, a slight decrease in performance due to mechanical losses was observed in the subsequent wind tunnel investigation using the E216 model.

Alkhabbaz *et al.* (2021) explained how the aerodynamic design of a 10 KW horizontal axis wind turbine rotor is completed. The generated nonlinear blade profile is refined to increase aerodynamic efficiency while reducing fabrication complexity. The chord and twist

distribution are linearized by dividing the congruent line of both ideal and real models into equal parts, which is a novel linearization technique.

Sayed *et al* (2012) studied the effectiveness of various blade profiles at different wind speeds, determining the best blade profile for each wind speed based on the highest sliding ratio. Additionally, the optimal angle of attack for each blade profile at each wind speed is determined. The numerical results are compared to measurements obtained in a wind tunnel.

Ahmad and Zafar (2023) research focuses on the challenges of self-starting and power efficiency in vertical axis wind turbines. A novel hybrid vertical axis wind turbines design with tubercles is created to achieve self-starting capability and a high power coefficient. The aerodynamic characteristics of the hybrid vertical axis wind turbines, including torque and power coefficients, are evaluated using a comprehensive investigation that combines experimental and computational techniques. Key findings include the hybrid design's ability to maintain positive static torque coefficients at all azimuth angles, resulting in independent self-starting. The hybrid configuration has a superior power coefficient of 0.475 at a tip speed ratio of 3, demonstrating its potential for power generation under low-wind conditions. Outer tubercles improve performance at low tip speed ratios, whereas inner tubercles improve performance at higher tip speed ratios. According to the study, the hybrid vertical axis wind turbines shows promise for residential power generation in low-wind-speed scenarios, and further investigation, including variable pitch angles, is recommended for future research. Furthermore, computational fluid dynamics is proposed for analysing rotor design variations and forecasting the development of hybrid wind turbines in wind farms.

Zhang *et al.* (2023) introduces a rapid prediction method for wind turbine airfoil aerodynamics with leading edge protuberances, treating leading edge protuberances as a simplified delta wing structure. Utilizing the GH-Bladed computing platform, the study verifies the impact of leading edge protuberances on the power output and blade performance of a 2.3 MW wind turbine under various conditions. Optimized leading edge protuberances show improved lift coefficients and stall characteristics, enhancing power output efficiency and stability during aerodynamic stall. In low wind speeds, leading edge protuberances increase average and maximum blade loads, while at higher speeds, they notably reduce fatigue and ultimate loads. Particularly near the rated wind speed, leading edge protuberances demonstrate a 7% reduction in average load and a 17% decrease in load standard deviation.

The study suggests that leading edge protuberances are more effective in reducing blade loads in high wind speed conditions, making them suitable for offshore wind turbine applications.

## **2.5 SUMMARY**

The synthesis of current research on leading edge tubercle technology and related studies reveals essential insights. Leading edge protuberances notably enhance an airfoil's aerodynamic performance by boosting maximum lift coefficients and stall delay. The proposed mechanism involves generating streamwise vortices, energizing the boundary layer to defer separation. These protuberances exhibit similarities to vortex generators and aid in diminishing dynamic stall while reducing the hysteresis loop. Studies on amplitude and wavelength variations suggest larger wavelengths offer more advantages, while amplitude has minimal impact. However, literature primarily explores Reynolds numbers below 100K, with a focus on airfoil profiles resembling Humpback Whale flipper cross sections and conventional airfoils.

This extensive review underscores the necessity for in-depth exploration of airfoil selection suited for low Reynolds number applications, as well as examining protuberance shape, amplitude, and wavelength. Such investigations are crucial for a more comprehensive understanding of the intricate flow dynamics linked to leading edge protuberances. These studies play a pivotal role in enhancing airfoil performance, especially in addressing aspects like dynamic stall and conducting comprehensive flow visualization analyses. The collective discoveries will contribute significantly to enhancing the aerodynamic efficiency of SHAWT functioning under low wind speeds.

## **2.6 RESEARCH GAP**

Certainly, the previous investigations regarding leading edge protuberances have primarily focused on applications at low Reynolds numbers. Additionally, these studies have predominantly examined sinusoidal leading edge shapes, limiting the exploration of other potential configurations. Consequently, there remains a lack of conclusive findings regarding the optimal amplitude and wavelength ranges suitable specifically for wind turbine applications. Moreover, the studies have not sufficiently delved into the effects of protuberances in dynamic scenarios, particularly in dynamic stall studies. Dynamic stall refers to the complex flow phenomenon occurring during abrupt changes in angles of attack,

commonly observed in wind turbine operation. Unfortunately, this particular aspect hasn't been thoroughly explored concerning the impact of protuberances.

Furthermore, the understanding of the underlying flow physics related to protuberances has primarily relied on numerical investigations rather than comprehensive experimental analyses. This limitation impedes a comprehensive understanding of the flow mechanisms associated with protuberances in practical aerodynamic scenarios, particularly in wind turbine applications. Thus, there's a significant need for further empirical research to expand our insights into the intricate flow physics behind leading edge protuberances, especially in the context of wind turbine aerodynamics under various operating conditions and dynamic scenarios.

## **2.7 RESEARCH OBJECTIVES**

- a) To study the effect of leading edge protuberances like sinusoidal, triangular and slot on two distinct assymmetric airfoils suitable for low Reynolds number applications.
- b) To investigate the effect of Reynolds number on the aerodynamic performance of airfoils with leading-edge protuberances.
- c) To study the effect of leading edge protuberances on unsteady aerodynamic characteristics.
- d) To determine the mechanism by which leading edge protuberances enhance airfoil performance.
- e) To investigate the effect of leading edge protuberances on the wind turbine performance.



## CHAPTER 3

### RESEARCH METHODOLOGY

This chapter is divided into two sections. The first section explains the experimental methodology, including model preparation, and instrumentation with a focus on testing of airfoils and wind turbine equipped with leading edge protuberance. The second section goes over the numerical methodology, outlining geometric considerations, meshing, and simulation solver setup. The reasoning behind the methodologies chosen is explained throughout.

#### 3.1 EXPERIMENTAL METHODOLOGY

##### 3.1.1 Subsonic Wind Tunnel Facility

The experiments were conducted in a subsonic open wind tunnel in the Mechanical Engineering Department of the National Institute of Technology Karnataka, India. The facility depicted in Figure 3.1 shows the open circuit wind tunnel components: (a) Test section, (b) Contraction cone, (c) Honeycomb and screens, (d) Settling chamber, and (e) Diffuser cone.



Figure 3.1: Subsonic wind tunnel facility at National Institute of Technology Karnataka, India.

The airfoil model is installed in the test section, where the incoming airflow from the settling chamber is filtered by honeycomb and screens. As the velocity increases through the contraction cone, a uniform, laminar flow into the test section is ensured. The mounting arrangements allow the test model's angle of attack to be adjusted. The flow returns to the open atmosphere via the diffuser cone, which is aided by an axial flow fan unit at the wind

tunnel's back end, which generates the necessary suction. The 1 x 1 x 2 m test section has a design velocity of 30 m/s and a turbulence intensity of around 0.1%. A 9:1 contraction ratio with a length of 2.25 m is required to achieve the required test section velocity, while the overall wind tunnel size is 4 x 4 x 13.5 m.

### 3.1.2 Three-component force balance and Load cell arrangement

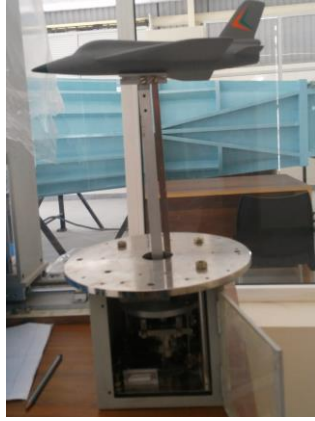
The aerodynamic forces generated by the airfoil model are measured using a highly sensitive three-component force balance, as shown in Figure 3.2. With an accuracy of 0.5%, this balance can handle 15 kg of normal force and 3 kg of drag force. A 16-bit data acquisition system facilitates data collection by averaging over 1 minute. The airfoil model is mounted on a stem within the test section and has a simple pitching adjustment mechanism. The load is transferred to four strain elements by the stem, which is attached to a metric plate. Strain gauges mounted on these elements produce outputs that are amplified appropriately by specially designed amplifiers.

$$\begin{aligned} L &= (D_{11}V_1 + D_{12}V_2 + D_{13}V_3)1000/G \\ P_m &= (D_{21}V_1 + D_{22}V_2 + D_{23}V_3)1000/G \\ D &= (D_{31}V_1 + D_{32}V_2 + D_{33}V_3)1000/G \end{aligned} \quad \left. \vphantom{\begin{aligned} L \\ P_m \\ D \end{aligned}} \right\} \quad (3.1)$$

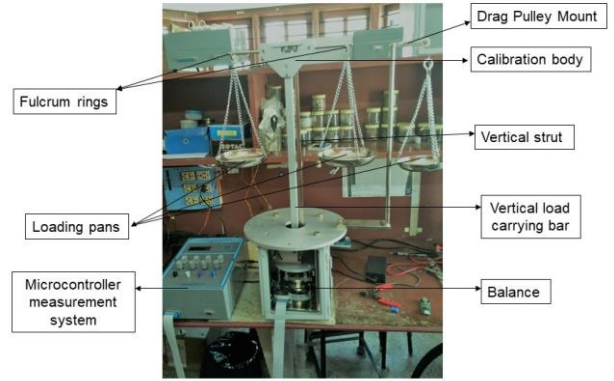
$$C_l = \frac{L}{\frac{1}{2}\rho V_\infty^2 a} ; \quad C_d = \frac{D}{\frac{1}{2}\rho V_\infty^2 a} \quad \left. \vphantom{C_l} \right\} \quad (3.2)$$

Where  $C_l$  is the lift coefficient, and  $C_d$  is the drag coefficient, and  $\rho$  is the density of the air ( $\text{kg/m}^3$ ),  $V_\infty$  is the free stream velocity inside the wind tunnel (m/s), and  $\alpha$  is the angle of attack ( $^\circ$ ).

Using equation 3.1 and the inverted matrix  $D_{ij}$  derived from the calibration coefficient matrix  $C_{ij}$ , the measured voltages are converted into forces and moments. The voltage conversion at the strain elements is accounted for by the denominator's gain.



(a) Three component force balance



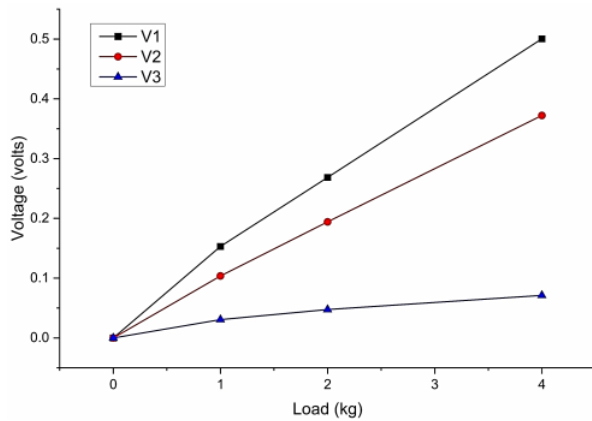
(b) Calibration setup for force balance

Figure 3.2: Force balance calibration setup.

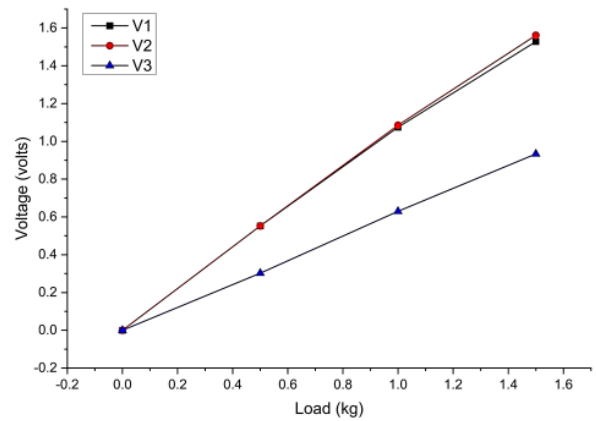
Equation 3.2 is used to convert the resulting aerodynamic forces into non-dimensional coefficients. The inverted matrix for  $C_{ij}$  and  $D_{ij}$  are given equation 3.3 and 3.4.

$$C_{ij} = \begin{bmatrix} C_{11} & C_{12} & C_{13} \\ C_{21} & C_{22} & C_{23} \\ C_{31} & C_{32} & C_{33} \end{bmatrix} \quad (3.3)$$

$$D_{ij} = \begin{bmatrix} -1.9595 & -2.0625 & 0.2352 \\ -17.2651 & 11.5158 & -50.6412 \\ 0.1080 & 0.0163 & 0.8266 \end{bmatrix} \quad (3.4)$$



(a) Lift curve



(b) Drag curve

Figure 3.3. Calibration curves.

Calibration of the force balance is performed to establish a linear relationship between measured forces (lift and drag) and pitching moment in response to applied loads. The linearity of this relationship is due to the use of strain gauge instrumentation. The slopes of

these linear variations are used to calculate calibration coefficients. The calibration body installed on the balance is shown in Figure 3.2(b), along with the associated microcontroller measurement system. Calibration curves are created by capturing voltages that correspond to pure lift, drag, and moment loads. The lift and drag calibration curves are depicted in Figure 3.3. Equation specifies the value of  $D_{ij}$  derived from this calibration process.

### 3.1.3 Airfoil model design and fabrication

Fifty low Reynolds number airfoils were studied, including benchmark types like Clark Y and Goe 417a, NREL airfoils like S822, S823, and NACA 66(2)-415, as well as specialized low Reynolds airfoils like the S, SD, and SG series designed for aircraft and wind turbines. Maximum lift-to-drag ratio ( $L/D$ ), maximum lift coefficient ( $C_{lmax}$ ), and stall angle ( $\alpha_{stall}$ ) were measured using XFOIL (Drela and Youngren 2001) at a Reynolds number of 100K. Among these airfoils, the SG6043 profile had  $(L/D)_{max} = 66.5$ ,  $C_{lmax} = 1.65$ , and  $\alpha_{stall} = 14.5^\circ$ , while the E216 profile had  $(L/D)_{max} = 68.5$ ,  $C_{lmax} = 1.57$ , and  $\alpha_{stall} = 13.5^\circ$ , the highest values among the airfoils considered. As a result, these two airfoils were chosen for further research.

### 3.1.4 Geometry modelling

Various airfoil models, including baseline and modified versions with leading-edge sinusoidal, triangular, and slot configurations, were created in SOLIDWORKS. The baseline's three-dimensional geometry was created by importing coordinate points from a text file obtained from UIUC (2014). To generate the necessary geometries, these imported points were connected using splines, and the baseline model was formed by extruding the curve derived from the joined airfoil coordinates across the required span.

The protuberance shapes considered for this study are sinusoidal, triangular and slot. The SOLIDWORKS design tool was used to create baseline and various leading edge protuberance models for the E216 and SG6043 profiles. The baseline model of both the profiles was developed by extruding the curve obtained by joining the airfoil coordinates to a span(x) of 0.132 m. The sinusoidal protuberance model was developed by lofting the equation-driven curve with the same span as the baseline model by using equation 3.5, where  $A$  and  $W$  are the amplitude and wavelength of the protuberances, respectively.

Table 3.1: Airfoil profile geometrical parameters

Parameters	SG6043	E216 (10.4%)
Thickness (%)	9.990	10.408
Camber (%)	5.498	5.169
Trailing Edge Angle (%)	10.646	8.688
Lower Surface Flatness (%)	18.685	14.584
Leading Edge Radius (%)	2.347	2.215

The geometrical parameters of the two airfoils are shown in Table 3.1, and their profiles are shown in Figure 3.4.

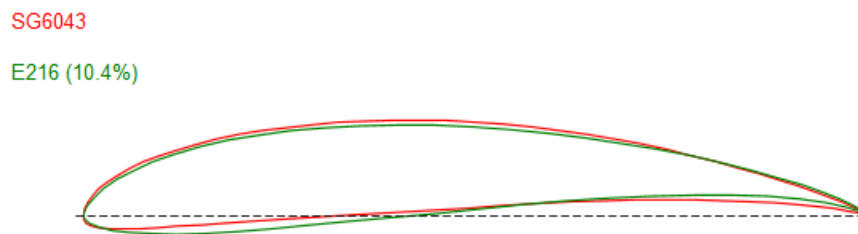


Figure 3.4: Coordinate data defining the shapes of airfoils SG6043 and E216.

$$y_x = A \sin(b x), \quad \text{Where } b = \frac{2\pi}{w} \quad (3.5)$$

The triangular and slot protuberance models were created similarly, but the leading-edge profile was drawn to achieve the desired shape. In this study, the amplitude values selected were  $0.03c$ ,  $0.06c$ , and  $0.11c$  and the wavelengths were  $0.11c$ ,  $0.21c$ , and  $0.43c$ , where  $c$  is the chord of the airfoil. These values are defined concerning a reference chord( $c$ ) of  $0.15\text{m}$ . For the slot protuberance, the thickness ( $t$ ) was maintained constant at  $0.002\text{ m}$ . Table 3.2 lists the various protuberance configurations and terminology used in this study. The design models of both the baseline and modified versions are depicted in Figure 3.5. Figure 3.6 depicts the top view of the leading-edge triangular models in all configurations, along with their relevant geometrical parameters.

Table 3.2 Protuberance configurations and their terminology

Configuration	Terminology	Configuration	Terminology	Configuration	Terminology
$A = 0.03c$ , $W = 0.11c$	A4.5W16.5	$A = 0.06c$ , $W = 0.11c$	A9W16.5	$A = 0.11c$ , $W = 0.11c$	A16.5W16.5
$A = 0.03c$ , $W = 0.21c$	A4.5W31.5	$A = 0.06c$ , $W = 0.21c$	A9W31.5	$A = 0.11c$ , $W = 0.21c$	A16.5W31.5
$A = 0.03c$ , $W = 0.43c$	A4.5W64.5	$A = 0.06c$ , $W = 0.43c$	A9W64.5	$A = 0.11c$ , $W = 0.43c$	A16.5W64.5

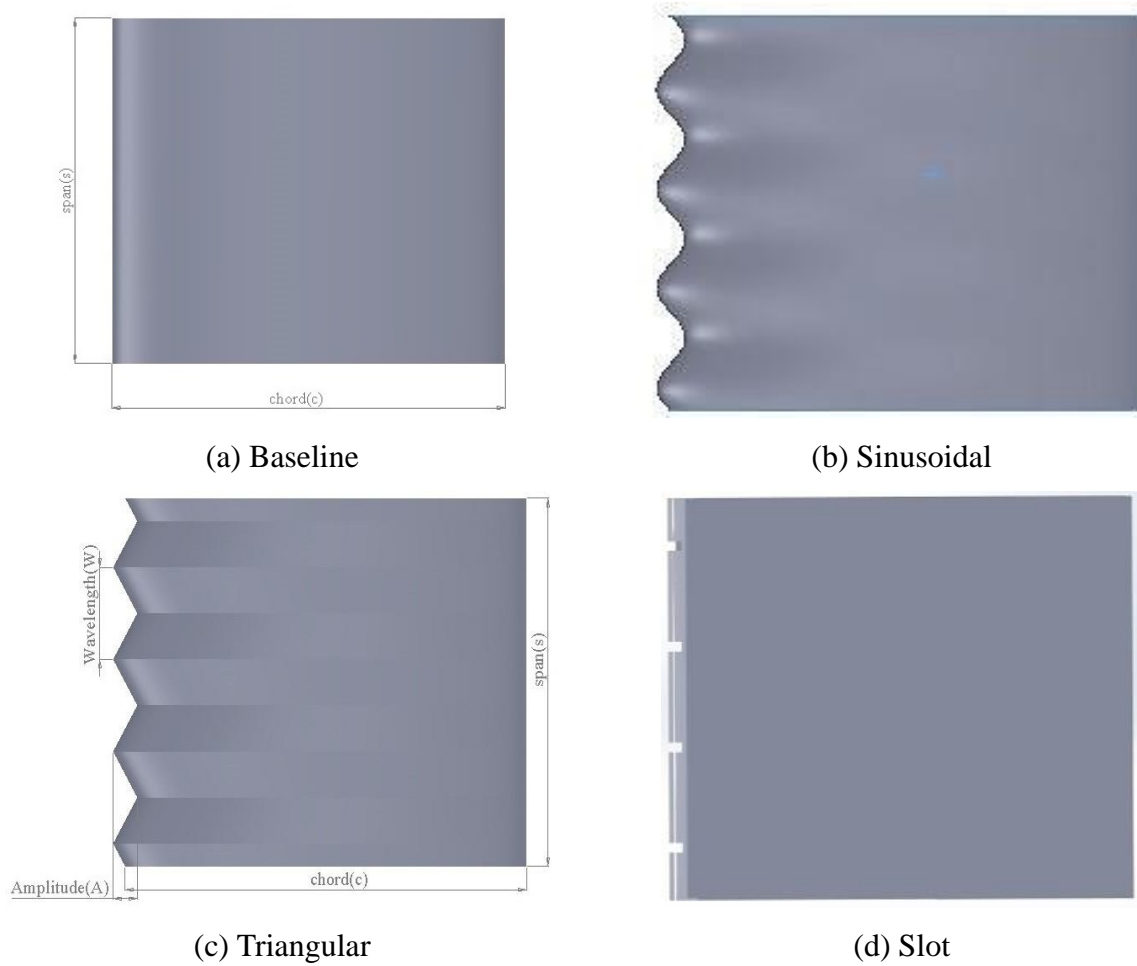


Figure 3.5: Top view of three-dimensional models of the E216 airfoil baseline and protuberance

Wavelength (W) Amplitude (A)	0.11c	0.21c	0.43c
0.03c			
0.06c			
0.11c			

Figure 3.6: Various configurations of triangular protuberance models

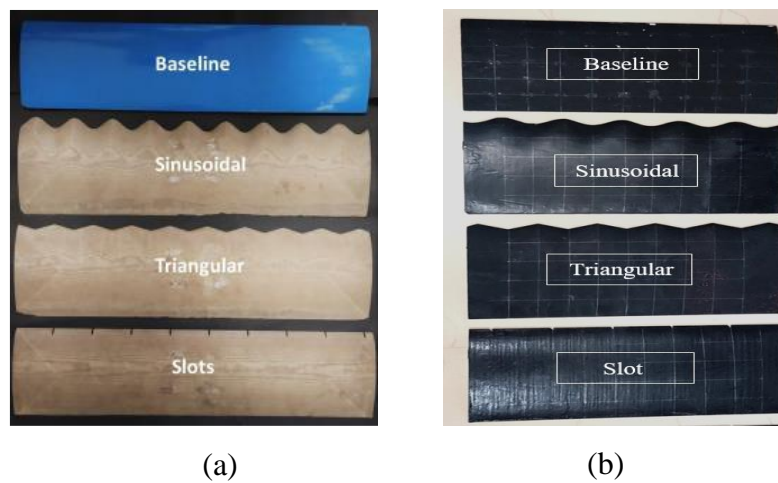


Figure 3.7: Experimental airfoil models - (a) Manufactured through 5-Axis CNC Milling machine from Medium-Density Fiberboard wood and (b) 3-D Printed models using Polylactic Acid (PLA) material

The A4.5W64.5 and A9W64.5 configurations were chosen for experimental investigation due to their optimal aerodynamic efficiency in the numerical investigation. Static testing was performed at a Reynolds number of 100K using the E216 and SG6043 airfoils in baseline and A9W64.5 configurations with sinusoidal, triangular, and slot leading edge protuberances.

These models were manufactured on a 5-axis CNC milling machine using Medium Density Fibreboard (MDF) wood as the material. Figure 3.7(a) displays the experimented models, comprising baseline and A9W64.5 configurations with leading-edge protuberances.

For experimental investigation of the effect of leading edge protuberances at different Reynolds numbers and for dynamic stall study, E216 baseline and A4.5W64.5 configuration were used. Further wind turbine experiments were carried out using both baseline and protuberance models. Models for dynamic analysis and turbine testing were manufactured in a 3D printing machine using polylactic acid material shown in Figure 3.7(b). The reasons for choosing 3D printed models are weight to strength ratio PLA and the weight limitation of the experimental test setup. Each airfoil model possesses a span of 0.592 m and a mean chord of 0.15 m, yielding a planform area of 0.08 m<sup>2</sup>.

### 3.1.5 Model mounting arrangement



(a) Model mounting for three component force balance



(b) Model mounting for Strain gauge balance

Figure 3.8: Airfoil mounting arrangement for static and dynamic study

Figure 3.8 illustrates the mounting arrangement of the airfoil for two distinct testing arrangements. In Figure 3.8(a), the airfoil model is horizontally positioned to investigate the aerodynamic effects of E216 and SG6043 baseline and protuberance models at a Reynolds number of 100K utilizing a three-component balance. The airfoil model is affixed to the L-frame section, which is connected to the struct rod, subsequently linked to strain gauges.

In the wind tunnel setup for measuring aerodynamic loads of E216 and SG6043 airfoils, the model is mounted on a stem within the test section. This stem is affixed to a metric plate, connected to four strain elements dedicated to measuring lift (15 kg), drag (2 kg), and pitching moment (50 kg-cm). The strain gauge outputs undergo amplification and time multiplexing before being fed into a 12-bit A/D converter with a range of 0 to +4.096V. The positioning and angle of the model are controlled via a pitching mechanism located at the base of the stem. The static study begins with the airfoil model mounted on a three-component force balance, with the wind tunnel velocity set to 10.8 m/s to correspond to a Reynolds number of 100K, allowing time for the tunnel flow to stabilize. Subsequently, aerodynamic forces acting on the airfoil model are collected through the stem protruding into the test section, which transfers the forces to the strain elements mounted on the metric plate. These strain gauge outputs are amplified using specially designed low-noise and highly stable instrumentation amplifiers. The amplified signals are then time multiplexed and connected to the 12-bit A/D converter. A microcontroller-based measurement system oversees the channel selection and A/D conversion processes. The resultant forces are displayed on a dedicated board and concurrently stored. The system collects averaged sample values every millisecond, while averaged updated data are presented on-screen every two seconds. This procedure is repeated for various angles of attack ranging from 0 to 20 degrees. In Figure 3.8(b), the airfoil model is vertically positioned to explore the Reynolds number effects of E216 baseline and protuberance airfoil models at various low Reynolds numbers. Additionally, this setup is employed to examine the dynamic effects of the same airfoil models at different reduced frequencies using a strain gauge arrangement. In this configuration, the model is directly connected to the stepper motor shaft at one end, with strain gauges fixed between the motor and airfoil closer to the motor. The aerodynamic forces acting on the airfoil model are conveyed to the shaft, and the strain gauges connected to the shaft directly measure these forces.

### **3.1.6 Pitot tube measurements**

To measure the local flow velocity within the wind tunnel, a 1.5mm diameter pitot-static tube was used. This tube made it possible to measure both free stream and wake velocity. The free stream velocity, denoted as  $U_\infty$ , was calculated in the empty tunnel using equation 3.6, with the pitot tube positioned in the same location as the model within the test section.

$$\rho_w g \Delta h_w = \frac{1}{2} \rho_a U_\infty^2 \quad (3.6)$$

where  $\Delta h_w$  is the total and static pressure differential measured in terms of water column height difference.

### 3.1.7 Boundary layer measurements

A 25 mm air gap was set up to ensure that the wind tunnel's model mounting and tunnel wall configuration allowed for unrestricted model movement during angle of attack adjustments. Verification was required to ensure that the air gap was smaller than the tunnel wall's boundary layer thickness. This determination was critical to avoid wing vortices and keep a two-dimensional experimental setup free of spanwise flow. Boundary layer measurements were taken within the wind tunnel using a boundary layer probe shown in Figure 3.9(a).

The boundary layer probe (shown in Figure 3.9(b)) consisted of 20 stainless steel tubes with internal diameters of 0.25 mm that were inclined down at  $150^\circ$  to capture pressure distribution very close to the wind tunnel wall. The electronic pressure transducer was used to measure the pressure. Pressure was measured at twenty different vertical positions using this probe at the same time. The probe locations are listed in Table 3.3. The local velocity ( $u$ ) at different vertical directions ( $y$ ) from the wind tunnel wall surface was measured until the local velocity equals 0.99 times the free stream velocity,  $U_\infty$ . Figure 3.9(c) depicts the boundary layer profile  $u/U_\infty$  plotted against the similarity variable (where  $\zeta = \frac{y}{2x} \sqrt{Re_x}$ ,  $y$  = vertical distance of measuring probe from tunnel wall,  $x$  = boundary layer development length, and  $Re_x$  = Reynolds number based on distance  $x$ ).

The boundary layer thickness,  $\delta^*$  and momentum thickness,  $\theta$  for this vertical distance were calculated using equations 3.7 and 3.8.



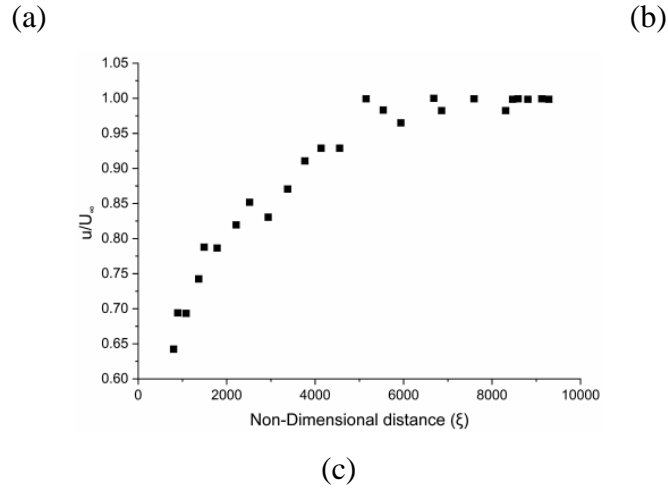


Figure 3.9: (a) Total pressure tube rake inside the wind tunnel test section (b) close-up of the rake (c) boundary layer profile.

$$\delta^* = \int_0^\delta \left(1 - \frac{u}{U_\infty}\right) dy \quad (3.7)$$

$$\theta = \int_0^\delta \frac{u}{U_\infty} \left(1 - \frac{u}{U_\infty}\right) dy \quad (3.8)$$

Table 3.3: Probe locations for measuring the boundary layer.

Probe number	1	2	3	4	5	6	7	8	9	10	11	12	13	14	15	16	17	18	19	20
Distance (mm)	0.5	1	2	3.5	4	5.5	7.5	9	11	13	14.5	16	18	20	22	24	27	28	31	34.5

The above equations were numerically solved using the trapezoidal rule. According to the calculations, the boundary layer thickness was 35.01 mm and the momentum thickness was 26.73 mm from the wall. As a result, the shape factor value is 1.31, indicating that the boundary layer is turbulent.

### 3.1.8 Wind Tunnel Corrections

The flow within a wind tunnel is constrained by its side wall. To simulate the flow as an open field flow and reduce measurement errors, necessary corrections called wind tunnel corrections must be incorporated into the measured data. The study followed the guidelines provided by Barlow *et al.* (2015) and Selig and McGranahan (2004). The corrections are solid blockage, wake blockage, and streamline curvature. considered in the study. Buoyancy and downwash corrections were not included in this model.

The presence of a model within the wind tunnel test section causes solid blockage, which reduces the effective area through which the air flows. Equation 3.9 was used to calculate the solid blockage correction factor. Here,  $t$  is the model thickness,  $h$  is the tunnel cross sectional height,  $\lambda_s$  and  $s$  is the shape factor, which is 1.5 as recommended by Barlow *et al.* (2015) for a tunnel-spanning wing.

$$\varepsilon_{sb} = 0.822 \lambda_s \frac{t^2}{h^2} \quad (3.9)$$

Wake blockage, abbreviated  $\varepsilon_{sb}$  is caused by a decrease in local pressure in the airfoil wake, resulting in higher flow velocity outside the wake than in the free stream. Equation 3.10 was used to calculate the correction factor,  $\varepsilon_{sb}$  (Selig and McGranahan, 2004).

$$\varepsilon_{wb} = \frac{c}{2h_{ts}} C_{du} \quad (3.10)$$

where  $h_{ts}$  is the height of the test section and  $C_{du}$  is the uncorrected drag coefficient. The wind tunnel walls influence the stream line curvature around the airfoil, resulting in induced pseudo camber of the airfoil in the test section. This simulated camber increases lift generation. Equation 3.11 was used to calculate the correction factor (Selig *et al.* 2004).

$$\sigma = \frac{\pi^2}{48} \left( \frac{c}{h_{ts}} \right)^2 \quad (3.11)$$

Finally, using equations 3.12 - 3.14, corrected parameters combining all blockage corrections were calculated:

$$U = U_{\infty}(1 + \varepsilon) \quad (3.12)$$

$$C_L = C_{lu}(1 - \sigma - 2\varepsilon) \quad (3.13)$$

$$C_D = C_{du}(1 - 3\varepsilon_{sb} - 2\varepsilon_{wb}) \quad (3.14)$$

Where  $\varepsilon_b = \varepsilon_{sb} + \varepsilon_{wb}$ . For the baseline airfoil model at angle of attack of  $12^0$ , following values for correction factors are obtained:

$$\varepsilon_{sb} = 3 \times 10^{-4}$$

$$\varepsilon_{wb} = 6.08 \times 10^{-3}$$

$$\sigma = 4.63 \times 10^{-3}$$

The calculated correction factors were extremely small and insignificant. As a result, wind tunnel corrections were not included in the study.

### 3.1.9 Wind tunnel turbulence intensity

Turbulence intensity (TI) represents velocity fluctuation in the wind tunnel and should be as low as possible in order to obtain a reliable result. It represents the variation in velocity in the wind tunnel. The TI of the wind tunnel in this study was calculated under the assumption that TI is isotropic (Schlichting and Gersten, 2016). As a result, the simplified equation shown 3.15 below is used to calculate TI.

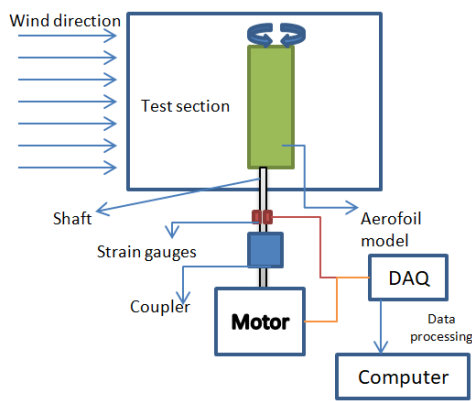
$$TI = \frac{\sqrt{u'^2}}{U_\infty} \quad (3.15)$$

where  $u'$  is the streamwise fluctuating velocity component.

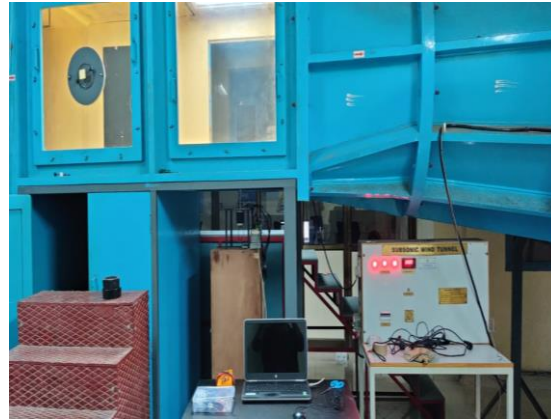
The TI for a free stream velocity of 10.8 m/s was calculated at various points in a plain 425 mm from the inlet of the test section, where the leading edge of the test model begins. The measurements were taken on a total of  $4 \times 4 = 16$  equidistant points in the plane. The distance from the surrounding wall measured in the free stream flow away from the boundary layer. The tunnel's TI was discovered to be an average of 0.12%.

### 3.1.10 Experimental procedure and data processing

Figure 3.10 (a) presents the schematic diagram of the experimental setup utilized in the study. In this arrangement, the airfoil was positioned vertically within the wind tunnel. A coupler connected a shaft, passing through the quarter chord of the airfoil, directly to a stepper motor. The stepper motor system was responsible for controlling both the blade position and the oscillations required for dynamic study. Strain gauges were manually affixed to the base of the shaft to measure the strain, enabling the determination of the forces exerted on the airfoil. Additionally, a sturdy steel frame was designed to house the motor, completing the experimental system. For a visual representation of the experimental setup, refer to Figure 3.10 (b).



(a)



(b)

Figure 3.10: (a) Schematic diagram of experiment setup experimental setup (b) Actual experimental setup with model.

The Nema 23 stepper motor shown in Figure 3.11 was selected, featuring specifications such as a torque of 25 Kg-cm, a step angle of  $1.8^\circ$  per step, and a shaft diameter and length of 8mm and 20mm, respectively. To drive this motor, the Rhino Motion Controls (RMCS-1106) micro-stepping drive was employed. This drive, utilizing a digital signal processor, is optimized for 1.8-degree bipolar stepper motors. It ensures quiet and efficient operation while maintaining torque and control at higher speeds. Safety features including short-circuit, over-voltage, and under-voltage protections are integrated into the RMCS-1106 for motor outputs.

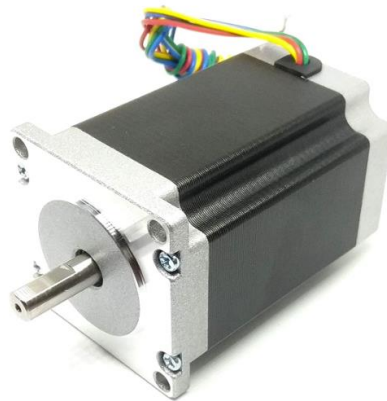


Figure 3.11: NEMA 23 stepper motor

During motor stoppage or slow rotation, the RMCS-1106 employs micro-stepping through synchronous pulse-width modulation output drive and accurate current feedback, leading to noiseless operation. Optical isolation enhances noise immunity for the pulse/step, direction, and enable inputs. These inputs are adaptable to logic drive signals of 2.5V, 3.3V, or 5V. The

low input drive current at 2.5V accommodates various logic families for driving the inputs. Moreover, individual anode and cathode connections for each input's opto-isolator enable versatile input drive interfaces.

**Data Acquisition System:**

This study employs a comprehensive data acquisition system comprising NI-9237, NI-9401 modules shown in Figure 3.12, Compact DAQ, and Compact RIO for synchronized and accurate experimental data collection. The NI-9237 module offers signal conditioning for up to four bridge-based sensors, while the NI-9401 module provides versatile bidirectional digital functionality. Compact DAQ and Compact RIO facilitate seamless integration, customizable through LabVIEW software. In wind tunnel force measurement, strain gauges, including wire and semiconductor types, detect aerodynamic load-induced elastic spring deformation. A half-bridge arrangement utilizing strain gauges on a shaft's surface is explored, guided by Finite Element Analysis (FEA) for precise positioning. The report underscores the Wheatstone bridge method's application, augmented by strain gauges and FEA for effective electrical resistance measurement, enriching practical implementation.

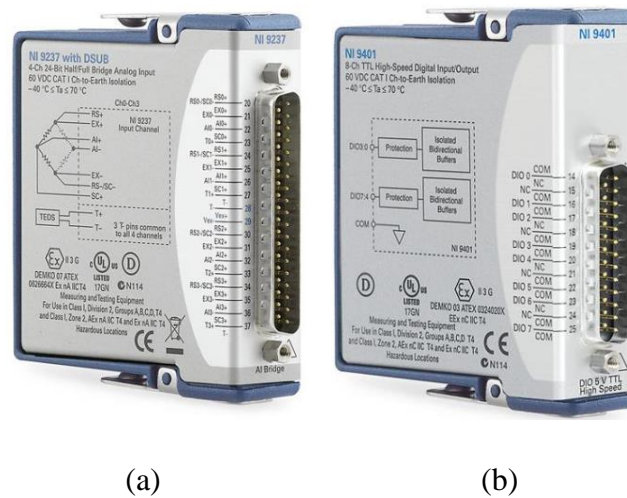


Figure 3.12: (a)NI-9237 DAQ (b)NI-9401 DAQ

Appendix A provides a comprehensive guide detailing the procedure for data processing and outlines the LabView programs used to control motor motion and facilitate data acquisition.

The lift and drag forces acting on the airfoil section vary continuously with the variable angle of attack as it pitches around a shaft passing through its cross-section. LabView software controls the data acquisition (DAQ). Initially, data is collected for two-degree increments over

a range of angles between 0 and 20 degrees. To ensure short-term reliability, a second run is conducted under identical conditions. The airflow is allowed to stabilize for about 30 seconds at each angle before data collection begins. The airfoil is retested after completing all tests to ensure medium-term dependability. The results of the short-term tests are found to be identical to those of the original tests. The LabView program drives a stepper motor to a required angle relative to a current rest position. It does so by sending a single pulse (consisting of 2 samples - one high and one low) to the pulse channel until the required angle is achieved. The direction channel is also given 2 samples (either both high or both low) depending on the boolean direction input. This procedure is repeated for different Reynolds numbers for the E216 airfoil under static conditions to evaluate its performance across various low Reynolds numbers.

### **Procedure for Dynamic Study:**

The airfoil was oscillated by directly controlling the position of the motor, facilitated by the direct coupling of the motor and shaft. A sinusoidal profile was fed to the motor controller at 0.01-second intervals, which was then interpolated to achieve the required frequency sinusoidal motion of the motor. Although the resulting motion was not purely sinusoidal due to the time required for the built-in interpolation function and the torsional moments produced by the lift and drag forces on the airfoil, the general motion appeared sinusoidal. However, some overshoot was experienced in all cases, and the peaks of the oscillations were occasionally warped, resulting in a mismatch in the angle of attack change between the fully sinusoidal motion and the actual motion of the airfoil. Despite this discrepancy, the difference in error between the two curves was minor, ensuring a high level of confidence in the final conclusions. The LabView code generates sinusoidal angular motion using a stepper motor and Rhino stepper driver. As the angular speed of a stepper driver is proportional to the pulse frequency, this frequency is varied as a cosine wave to produce angular displacement as a sine wave.

A custom-designed program using LabView software was employed to control the positioning, dynamic motion, and gathering of strain gauge data. The program aimed to offer a unified user interface capable of managing both the airfoil's position and the collection of strain gauge data simultaneously. Organized around a series of case structures accessible via a menu, the program facilitated a seamless transition between static and dynamic controls. Each

structure comprised one high-priority loop and one low-priority loop. The high-priority loop oversaw hardware functions such as motor control and strain data gathering. To ensure timely completion of each task within the loop, it was timed and synchronized with the Compact Rio. The collected data, including the motor's position, strain from each half bridge, and timestamp, was recorded to local variables. Subsequently, the low-priority loop utilized these variables to display and save the data to a file. Raw voltages obtained from the Wheatstone bridges were translated into equivalent lift and drag coefficients through data processing. Utilizing calibration curves established earlier, the voltages recorded at each angle of attack were averaged over the data acquisition period and converted into their respective normal and tangential forces.

### 3.1.11 Uncertainties in the experiment

The electronic manometer used in the experiment to measure pressure has an uncertainty of  $\pm 0.03\%$ . Uncertainty in the derived quantity is calculated as described in Kline (1963). If  $R$  is defined as a function of the independent variables  $x_1; x_2; x_3, \dots, x_n$ . shown in equation 3.16. Thus,

$$R = R(x_1, x_2, x_3, \dots, x_n) \quad (3.16)$$

Let represent the uncertainty in the  $R$  and  $\omega_1, \omega_2, \omega_3, \dots, \omega_n$ , Let represent the uncertainties in the independent variables shown in equation 3.17. Then,

$$\omega_R = \left[ \left( \frac{R}{x_1} \omega_1 \right)^2 + \left( \frac{R}{x_2} \omega_2 \right)^2 + \dots + \left( \frac{R}{x_n} \omega_n \right)^2 \right]^{\frac{1}{2}} \quad (3.17)$$

The maximum uncertainties obtained for the derived parameters are  $\pm 3.74\%$  for  $C_l$ ,  $\pm 1.77\%$  for  $C_d$ , and  $\pm 5.69\%$  for  $C_l/C_d$ . Additional information regarding experimental uncertainties is available in Appendix A.

### 3.1.12 Smoke flow visualization setup

A smoke generator, which produced dense white smoke aligned with the air movement direction, was used to observe flow patterns over the airfoil models. The apparatus (Figure 3.13) is made up of a liquid reservoir, a heating zone, a smoke tube with control valves, and a blower/compressor located beneath the control unit to direct smoke into the test area.

Table 3.4 lists the specifications and capacities of the smoke generator, which includes a 1 kW heater capacity, a 0.24 HP blower capacity at 2800 RPM, and a smoke collecting jar with a capacity of 2000 ml. The visualization was done at low RPMs, typically between 25 and 30.



(a) Front view (b)Rear view

Figure 3.13: Smoke generator arrangement.

Table 3.4: Smoke generator specifications

Parameter	Value
Heater capacity	1 kW
Glass beaker oil capacity	500 ml
Oil drain capacity	200 ml
Smoke collecting jar	2000 ml
Blower capacity	0.24 HP, single phase, 2800 RPM

### 3.1.13 Tuft flow visualization arrangement

Tuft flow visualisation is an aerodynamic technique used to visually assess and understand airflow patterns around objects such as airfoils or vehicles. This method entails attaching small pieces of yarn or tufts to various points on the object's surface and observing their behaviour under various flow conditions. The tufts were methodically arranged in a grid-like pattern along the suction surface of the baseline airfoil in this study to allow for clear visualisation and analysis of airflow separation and reattachment. The tufts were meticulously placed on the surface of the airfoil, with consistent spacing and lengths. This configuration aimed to make changes in boundary layer behaviour and airflow patterns more visible. The

tuft arrangement on airfoil surfaces for flow visualization is depicted in Figure 3.14 for both baseline and modified airfoils.

A specific arrangement strategy was used for the protuberance models. One row of tufts was attached to the protuberance's peak, while another row was attached to the trough. This configuration enabled researchers to observe directional changes in flow patterns, with a particular emphasis on the transition and mixing of primary and secondary flows during the reattachment process.

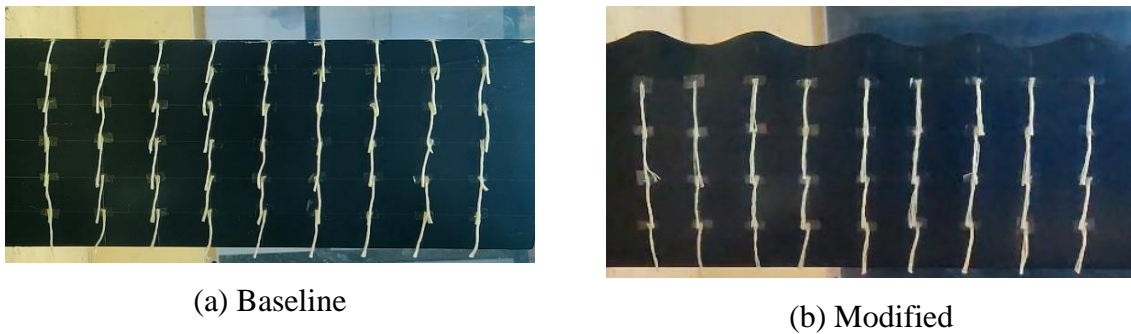


Figure 3.14: Tuft arrangement on airfoil surfaces for flow visualization and analysis

The wind tunnel tests included a variety of experimental conditions, including different angle of attack and Reynolds numbers. These parameters were systematically changed in order to generate different flow regimes and simulate various airfoil performance scenarios. The variation in angle of attack allowed for an evaluation of the airfoil's response under varying lift and drag conditions, while changes in Reynolds numbers revealed information about the impact of flow speed on boundary layer behaviour.

## 3.2 NUMERICAL METHODOLOGY

### 3.2.1 Computational fluid domain and Boundary conditions

Figure 3.15 depicts the computational domain, boundary conditions, and mesh strategy. A semi-circular inlet domain was created to optimise computational efficiency, to generate a highly refined mesh specifically around the airfoil while using a coarser mesh in the far-field region. The sphere of influence technique was used to refine the mesh selectively in order to reduce computational time. Because of the intricate leading-edge geometry with distinct protuberances such as sinusoidal, triangular, and slots, each with varying amplitudes and wavelengths, an unstructured mesh composed of tetrahedral elements was chosen.

The following boundary conditions were used: (i) a velocity inlet condition specified on the domain's semicircular surface, (ii) a pressure outlet condition set to atmospheric pressure on the domain's outer vertical surface, and (iii) a no-slip condition applied on both the airfoil surface and the domain's outer horizontal surfaces. To meet the requirements of the turbulent model, the first cell height was calculated with a  $y^+$  calculator and set at 0.029mm, resulting in a non-dimensional wall distance ( $y^+$ ) below one. The convergence criterion was set at a residual value of  $10^{-5}$ .

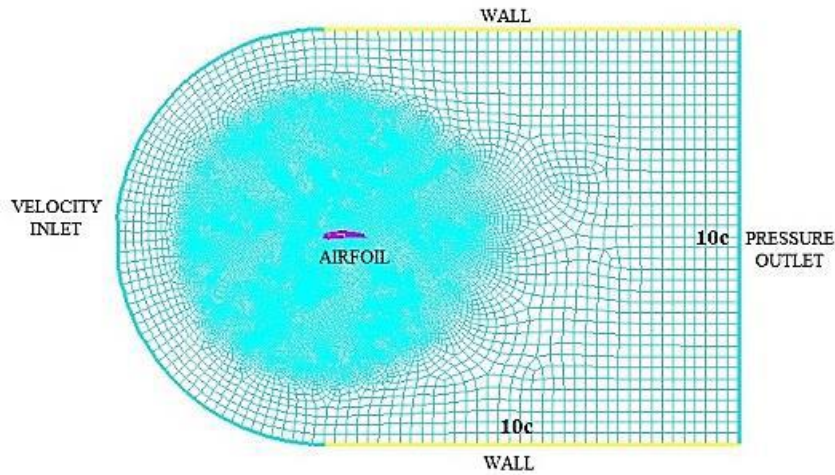


Figure 3.15: Computational domain and boundary conditions with a far field length of  $10c$ .

The SIMPLE (Semi-Implicit Method for Pressure-Linked Equations) algorithm by Patankar (2018) was used to solve the velocity and pressure fields, while the SST  $k-\omega$  model was used for turbulence modelling. The least squares cell-based gradient and second-order upwind schemes were used for spatial discretization (as described in the (FLUENT 2014)). The simulations were run at a Reynolds number of 100K with angles of attack ranging from  $0^\circ$  to  $+20^\circ$ .

### 3.2.2 Governing Equations and Turbulence model

The equations that govern the flow around the airfoil model (Gawad, 2013) are time-averaged continuity and momentum equations, which are given for the steady flow of a constant-property fluid respectively by,

$$\frac{\partial U_i}{\partial x_i} = 0 \quad (3.18)$$

$$U_j \frac{\partial U_i}{\partial x_j} = \frac{\partial}{\partial x_j} (v \frac{\partial U_i}{\partial x_j} - \overline{U_i U_j}) - \frac{1}{\rho} \frac{\partial P}{\partial x_j} \quad (3.19)$$

In equations 3.18 and 3.19,  $i, j = 1, 2, 3$ ,  $U_i$  is the mean-velocity vector in three directions (x, y, and z),  $P$  is static pressure,  $\rho$  is fluid density, and  $\nu$  is its kinematic viscosity. Indexes that are repeated imply summation. In equation 3.19, the unknown Reynolds stress  $\overline{U_i U_j}$  is calculated using the  $k$ - model, as shown in equation 3.20:

$$\overline{U_i U_j} = \frac{\mu_t}{\rho} \left( \frac{\partial U_i}{\partial x_j} + \frac{\partial U_j}{\partial x_i} \right) - \frac{2}{3} \delta_{ij} \left( k + \frac{\mu_t}{\rho} \frac{\rho U_k}{\rho x_k} \right) \quad (3.20)$$

The eddy-viscosity in equation 3.21 is,

$$\nu_t = \frac{\mu_t}{\rho} \quad (3.21)$$

The  $k$ - $\omega$  based SST model accounts for turbulent shear stress transport and provides highly accurate predictions of the onset and amount of flow separation under adverse pressure gradients.

The baseline  $k$  - $\omega$  model combines the benefits of the Wilcox and  $k$  - $\omega$  models, but it still fails to predict the onset and amount of flow separation from smooth surfaces. This deficiency arises primarily because these models do not account for the turbulent shear stress transport, which overpredicts the eddy-viscosity. As a result, the proper transport behaviour can be obtained by adding a limiter to the eddy-viscosity formulation, as shown in equation 3.22:

$$\nu_t = \frac{a_1 k}{\max(a_1 \omega SF)} \quad (3.22)$$

Where  $F$  is a blending function used to blend the  $k$  - $\omega$  model near the surface and the  $k$  - $\epsilon$  model developed by Menter in the outer region. It consists of converting the  $k$  - $\omega$  model to a  $k$  -  $\epsilon$  formulation and then adding the corresponding equations.  $S$  is an invariant strain rate measure.

The SST  $k$  - $\omega$  model is similar to the standard  $k$  - $\omega$  model in structure:

$$\frac{\partial}{\partial t} (\rho k) + \frac{\partial}{\partial x_i} (\rho k u_i) = \frac{\partial}{\partial x_j} \left( \Gamma_k \frac{\partial k}{\partial x_j} \right) + \tilde{G}_{k^1} - Y_k + S_k \quad (3.23)$$

$$\frac{\partial}{\partial t} (\rho \omega) + \frac{\partial}{\partial x_i} (\rho \omega u_i) = \frac{\partial}{\partial x_j} \left( \Gamma_\omega \frac{\partial \omega}{\partial x_j} \right) + G_\omega - Y_\omega + D_\omega + S_\omega \quad (3.24)$$

$G_k$  represents the generation of turbulence kinetic energy due to mean velocity gradients in equations (3.23) and (3.24).  $G_\omega$  denotes the generation of specific dissipation rate of  $\omega$ .  $\Gamma_k$  and  $\Gamma_\omega$  represent the turbulence-induced dissipation of  $k$  and  $\omega$ .  $D_\omega$  denotes the cross-diffusion term.  $S_k$  and  $S_\omega$  are user defined source terms.

### 3.2.3 Grid independent study

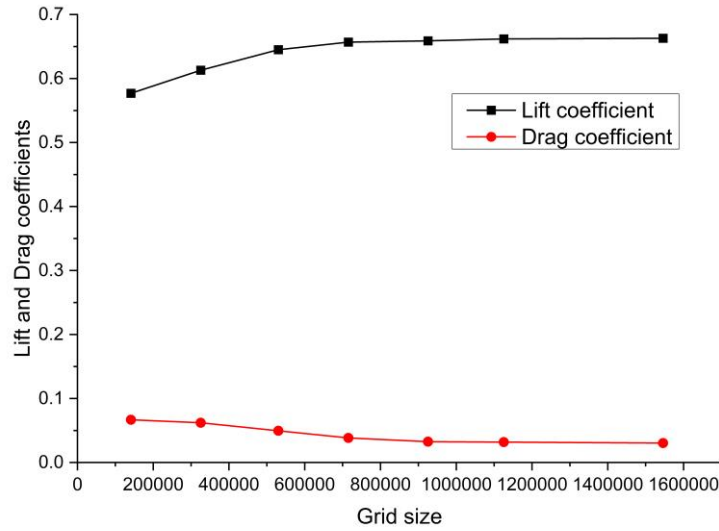


Figure 3.16: Grid independence analysis for the E216 profile at  $0^\circ$  angle of attack.

Table 3.5: Grid Convergence Specifications

Grid	No. of elements	Max. $y^+$	Aerodynamic coefficients	
			$C_l$	$C_d$
G1	141054	0.2	0.597	0.0668
G2	325460	0.2	0.613	0.0621
G3	530240	0.2	0.645	0.0426
G4	715025	0.2	0.657	0.0384
G5	925457	0.2	0.659	0.0375
G6	1125458	0.2	0.662	0.0362
G7	1545789	0.2	0.663	0.0359

A three-dimensional unstructured grid composed of tetrahedral elements was constructed for the computational domain. To accurately capture the airfoil wake profile, a local grid

refinement zone was established around the airfoil using a sphere of influence with a radius of  $4c$  (four times the chord length). Maintaining  $y^+$  values below one at the walls aimed to capture near-wall effects effectively. The grid study for the baseline model of the E216 profile at an angle of attack of  $0^\circ$  is depicted in Figure 3.16.

Various grid sizes ranging from 1 lakh to 15 lakh elements were chosen for the baseline model. To assess convergence, the study investigated the change in coefficient of lift and coefficient of drag values with increasing grid elements.

The plotted curves in Figure 3.15 showcased a linear variation in  $C_l$  and  $C_d$  from G1 to G4, followed by nearly straight curves. The average variations in  $C_l$  and  $C_d$  between G3 and G4 were 5.45%, and the variation between grids G4 and G5 was 1.35%. Consequently, grid G4 was selected for further numerical analysis to investigate airfoil flow characteristics and aerodynamic performance. Table 3.5 summarizes the pertinent information regarding the grids utilized in the study.



# CHAPTER 4

## RESULTS & DISCUSSIONS

The study investigates the effect of leading edge modifications, such as sinusoidal, triangular, and slotted configurations, on two distinct low Reynolds number airfoils (E216 and SG6043) in the first section, using both numerical and experimental approaches. The second section looks at how Reynolds number under static conditions and reduced frequency under dynamic conditions affect the aerodynamic properties of the E216 airfoil. Following that, smoke flow visualization studies on both the E216 and SG6043 airfoils are carried out to gain insight into flow behaviours.

### 4.1 NUMERICAL SCHEME VALIDATION

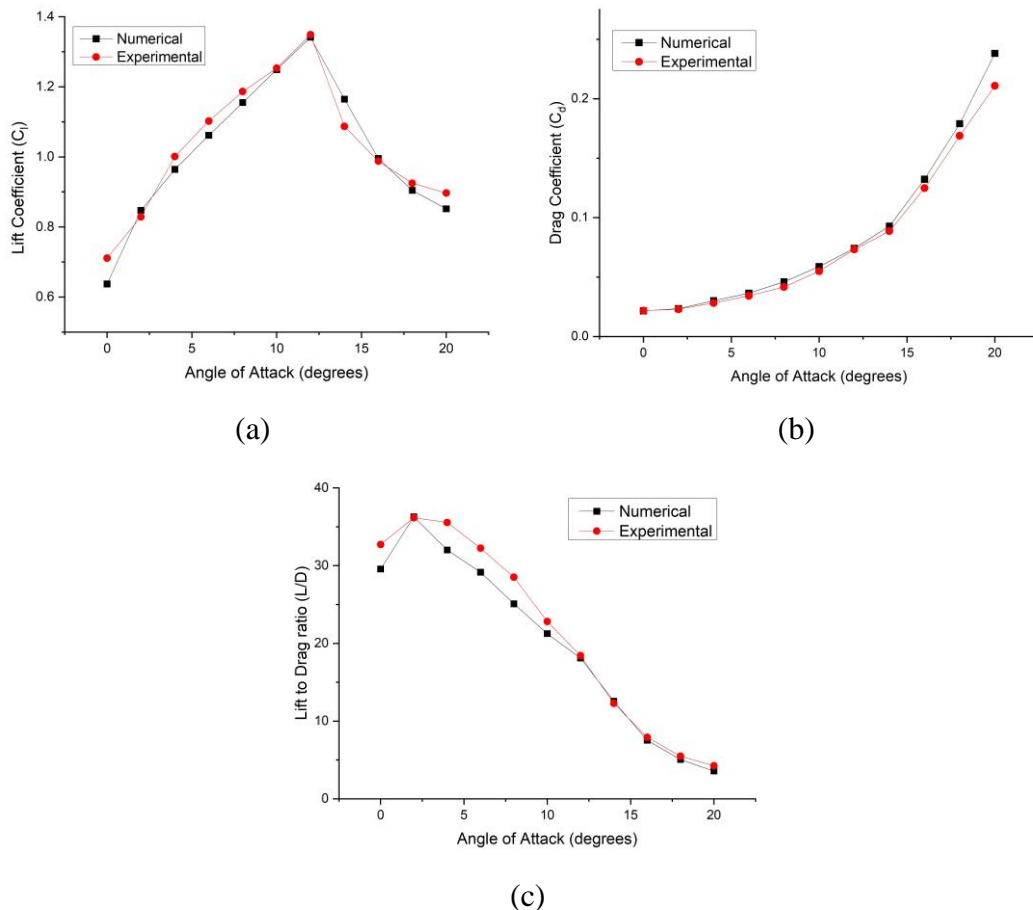


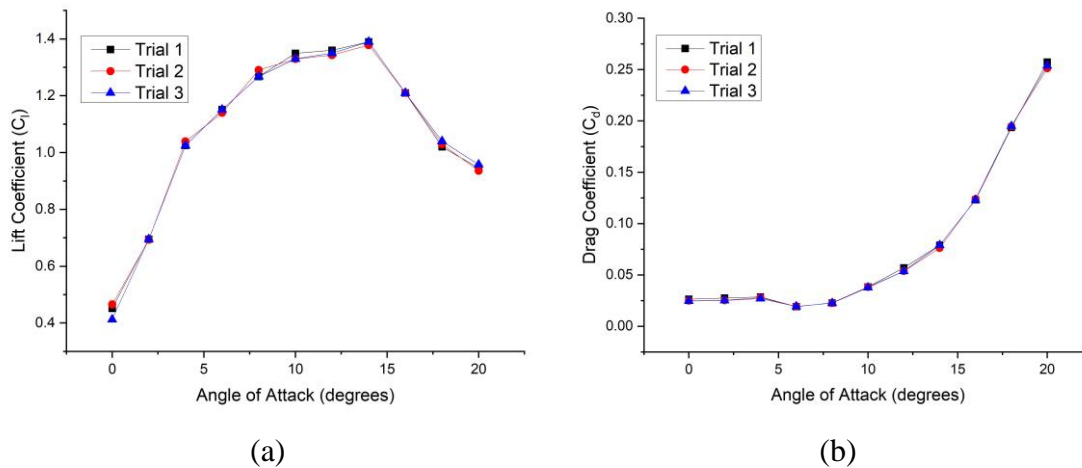
Figure 4.1: Numerical scheme validation for the E216 baseline airfoil (a) Lift coefficient (b) Drag coefficient, and (c) Lift to drag ratio

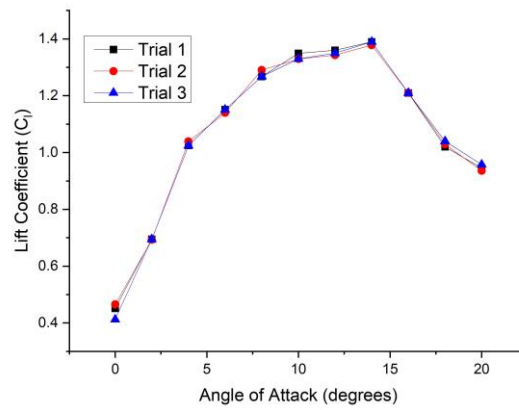
Simulation results for the E216 baseline airfoil model were compared and validated against experimental results. The values of  $C_l$ ,  $C_d$ , and  $L/D$  obtained from both experiments and simulations were plotted against the angle of attack as shown in Figure 4.1.

The agreement between the simulation and experimental results was deemed acceptable. On average, a 1.37% error was observed for  $C_l$ , 6.73% for  $C_d$ , and 6.84% for  $L/D$ . Factors contributing to this discrepancy include experimental model surface roughness, ambient temperature fluctuations, accuracy of the computational model, and experimental imprecision. Due to the computational expense related to higher-order models, the numerical analyses were conducted using the  $k-\omega$  SST model. Additionally, while simulations utilized pure air properties, experimental conditions might involve impurities in the air, potentially contributing to differences in the obtained results.

## 4.2 EXPERIMENTAL REPEATABILITY

To ensure experimental reliability, outcomes from three distinct trials were graphically compared on a single set of axes for the SG6043 baseline airfoil, as shown in Figure 4.2. The results indicated consistent trends across the trials without any significant differences noted. Throughout the experimentation, average errors of 0.31%, 1.39%, and 2.1% were observed for  $C_l$ ,  $C_d$ , and  $L/D$ , respectively. All experiments were conducted under identical atmospheric conditions to maintain stability in the aerodynamic coefficients, ensuring consistency across the trials.





(c)

Figure 4.2: Experiment repeatability for the SG6043 baseline airfoil (a) Lift coefficient (b) Drag coefficient, and (c) Lift to drag ratio

## 4.3 STATIC STUDY

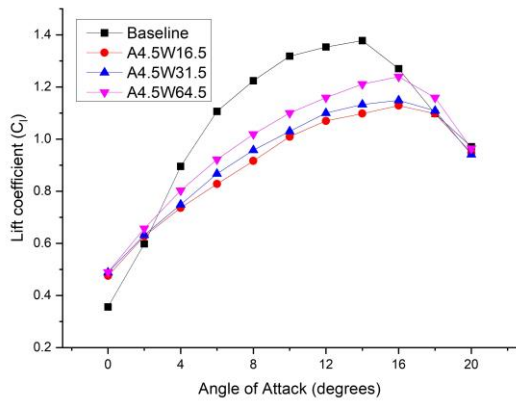
### 4.3.1 Sinusoidal Protuberances

Various aerodynamic variables like maximum lift coefficient ( $C_{l_{max}}$ ), stall angle ( $\alpha_{stall}$ ), and maximum lift to drag ratio ( $(L/D)_{max}$ ) for different configurations and airfoils were compared with baseline values (SG6043 and E216) in Table 4.1. Generally, lower amplitude configurations caused a  $2^\circ$  delay in stall angle for both airfoils. Lower amplitude configurations in E216 airfoil showed higher  $C_{l_{max}}$  and  $(L/D)_{max}$  compared to the baseline.  $C_{l_{max}}$  and  $(L/D)_{max}$  increased with constant amplitude and higher wavelength but decreased with increased amplitude for constant wavelength.

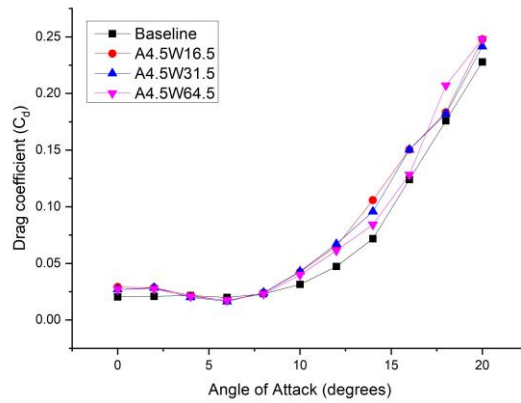
The stall delay was associated with improved  $C_{l_{max}}$  and  $(L/D)_{max}$  for A4.5W31.5 and A4.5W64.5 configurations of E216 airfoil. All of the other configurations showed a decrease in  $C_{l_{max}}$  and  $(L/D)_{max}$  but not in stall angle.  $C_{l_{max}}$  and  $(L/D)_{max}$  increased with wavelength for configurations with the same amplitude. However, for constant wavelength,  $C_{l_{max}}$  and  $(L/D)_{max}$  decreased as amplitude increased. As a result, low amplitude and high wavelength are recommended for the best aerodynamic performance. In Figures 4.3 and 4.4, these numerical results are plotted alongside the baseline SG6043 and E216 results. We observed a decrease in prestall lift performance and a marginal improvement in post-stall lift for SG6043. For all protuberance configurations, the zero-lift coefficient increased.

Table 4.1: The aerodynamic performance of the E216 and SG6043 airfoils with sinusoidal protuberances.

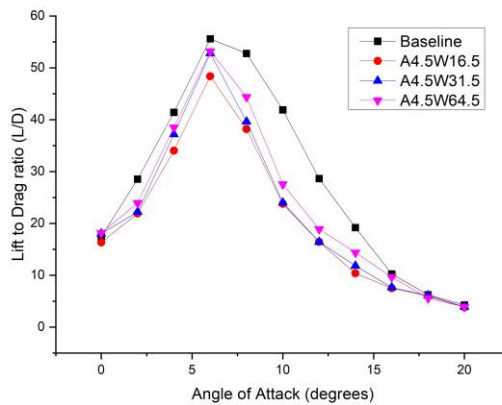
Configuration	E216			SG6043		
	$C_{lmax}$	$\alpha_{stall}$	$(L/D)_{max}$	$C_{lmax}$	$\alpha_{stall}$	$(L/D)_{max}$
A4.5W16.5	1.31	14	34.3	1.12	16	48.39
A4.5W31.5	1.36	14	36.1	1.14	16	52.83
A4.5W64.5	1.39	14	38.6	1.23	16	53.16
A9W16.5	1.28	12	30.7	1.15	14	45.71
A9W31.5	1.31	12	32.3	1.17	14	48.88
A9W64.5	1.34	12	34.6	1.25	14	51.89
A16.5W16.5	1.21	12	27.3	1.13	14	44.12
A16.5W31.5	1.25	12	29.5	1.18	14	47.32
A16.5W64.5	1.30	12	32.4	1.26	14	48.91
Baseline	1.35	12	36.2	1.37	14	55.6



(a)



(b)



(c)

Figure 4.3: The effect of sinusoidal protuberance wavelength on the aerodynamic parameters of an SG6043 airfoil with constant amplitude (a) Lift coefficient (b) Drag coefficient, and (c) Lift to drag ratio

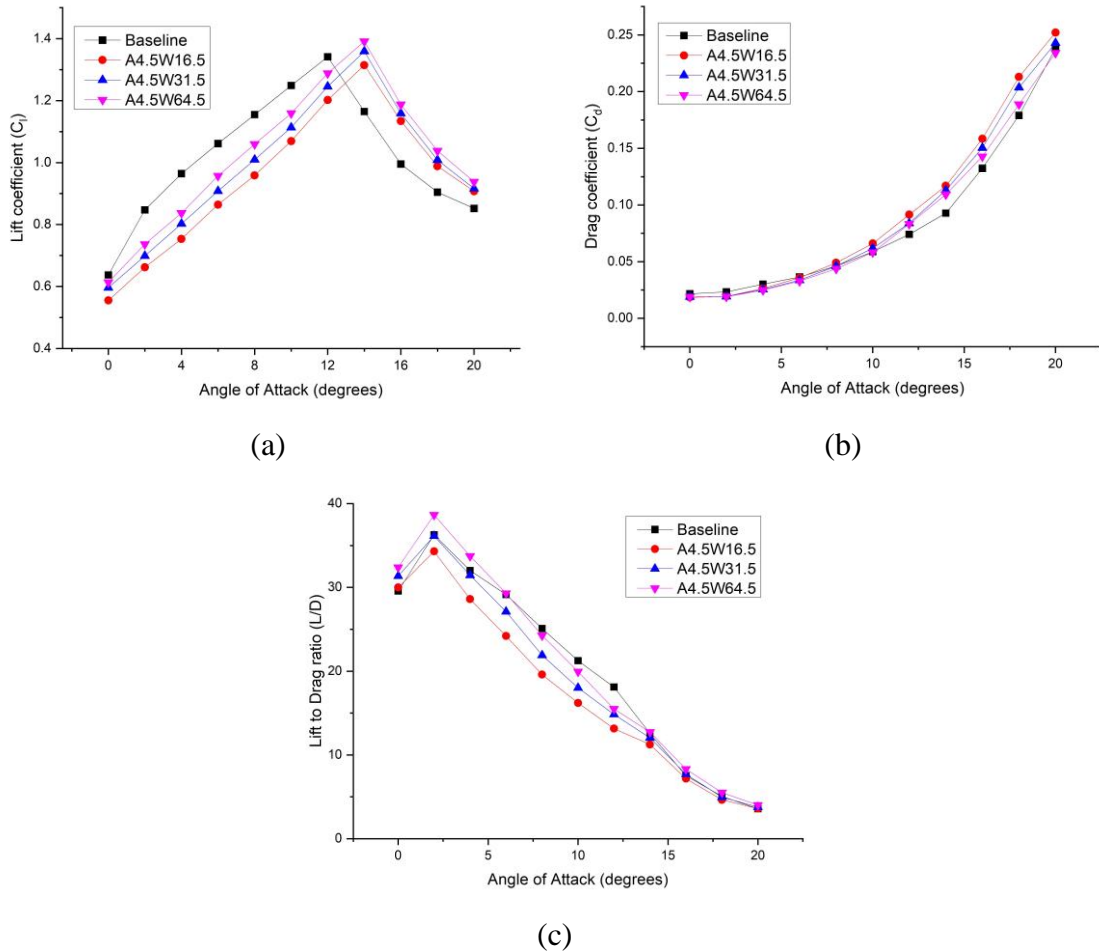


Figure 4.4: The effect of sinusoidal protuberance wavelength on the aerodynamic parameters of an E216 airfoil with constant amplitude (a) Lift coefficient (b) Drag coefficient, and (c) Lift to drag ratio

Drag values remained unchanged until an angle of attack of  $8^\circ$ , at which point protuberance configurations produced higher drag values than the baseline. L/D ratios were lower in all configurations than at the baseline. Lift curves plotted in Figure 4.4(a) show a degradation in pre-stall lift performance, stall delay, and an improvement in  $C_{l_{max}}$  for E216.

Furthermore, we noticed improved poststall lift performance. Drag values were not significantly affected until an angle of attack of  $10^\circ$ , at which point protuberance configurations produced higher drag values than the baseline.

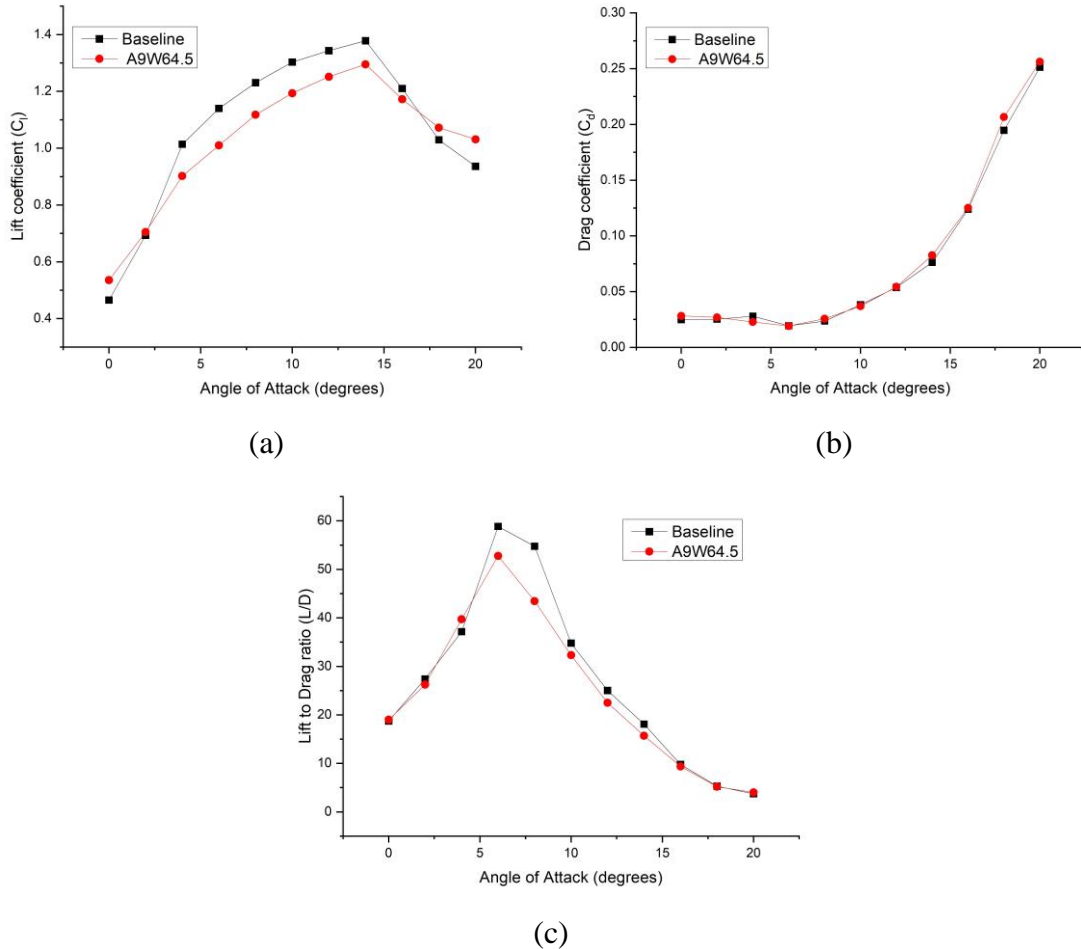


Figure 4.5: Experimental results of the SG6043 baseline and the A9W64.5 sinusoidal protuberance model (a) Lift coefficient (b) Drag coefficient, and (c) Lift to drag ratio

A4.5W64.5 had the highest drag at high angle of attack of the configurations tested. Despite the fact that the L/D ratio was lower than the baseline for the majority of the angle of attack, the protuberance configurations produced higher  $(L/D)_{\max}$  values. Only the A9W64.5 configuration was used for experimental force measurements because it produced the best results in the numerical analysis. The outcomes were compared to the baseline outcomes (Figures 4.5 and 4.6). In the experimental lift curve depicted in Figure 4.5(a), prestall lift degradation, poststall lift improvement, and increased zero lift coefficient were observed for

the SG6043 airfoil. The drag values in Figure 4.5(b) are similar to the baseline across the entire angle of attack range, contradicting the numerical results.

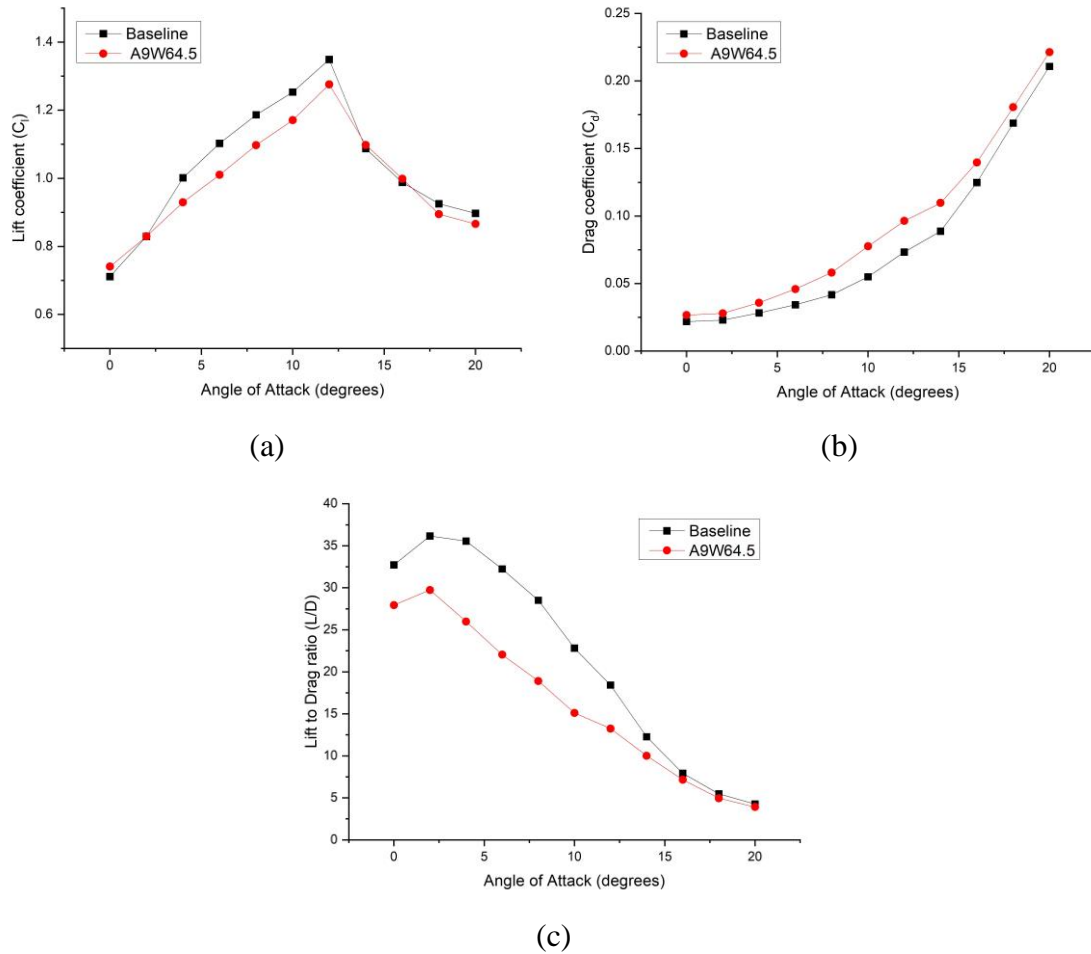


Figure 4.6: The experimental results of the E216 baseline and the A9W64.5 sinusoidal protuberance model (a) Lift coefficient (b) Drag coefficient, and (c) Lift to drag ratio

This could be because of the drag measurement technique, which employs strain gauges. The wake survey method, which is beyond the scope of this study, can provide more accurate drag measurements. For the majority of the angle of attack range, the L/D ratio curve of A9W64.5 was lower than the baseline curve (Figure 4.5(c)). Similarly, prestall lift degradation was observed in experimental lift curves for the E216 airfoil, as shown in Figure 4.6(a). There was no stall delay and an improvement in poststall lift, which is consistent with numerical simulations. The drag curves in Figure 4.6(b) show that the protuberance configuration has a higher drag than the baseline across the entire angle of attack range, which is partially captured in simulations. For the majority of the angle of attack range shown in Figure 4.6(c), the L/D ratio curve of A9W64.5 was lower than the baseline curve.

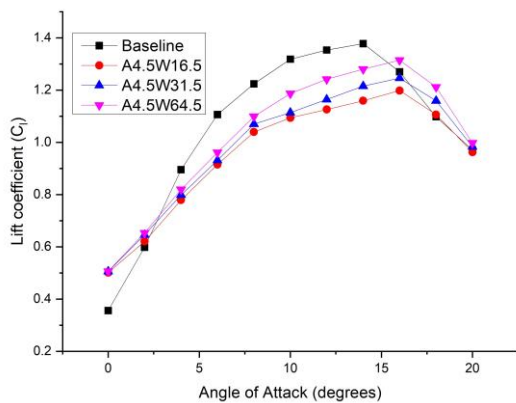
### 4.3.2 Triangular Protuberances

Table 4.2 summarizes the numerical results for E216 and SG6043 airfoils with triangular protuberances, compared with baseline values. For SG6043, a  $2^\circ$  stall delay was seen in the lowest amplitude configuration, leading to reduced  $C_{lmax}$  and  $(L/D)_{max}$  for all configurations except A4.5W64.5, which showed comparable values to the baseline. The E216 exhibited a  $2^\circ$  to  $4^\circ$  stall delay for A4.5 and A9 models, with improved  $C_{Lmax}$  and  $(L/D)_{max}$  for the lowest amplitude configuration.

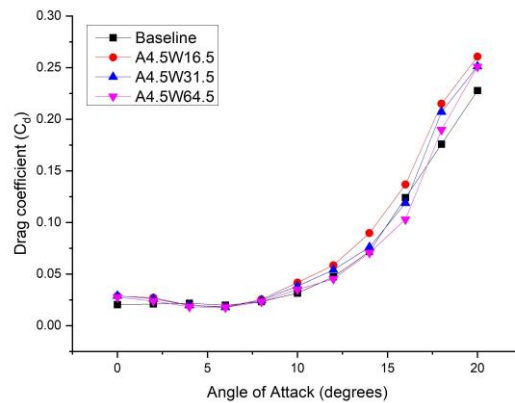
Stall delay of  $2^\circ$  to  $4^\circ$  was observed for A4.5 and A9 models of the E216 airfoil. The lowest amplitude configuration showed an improvement in  $C_{lmax}$  and  $(L/D)_{max}$ .

Table 4.2: The aerodynamic performance of the E216 and SG6043 airfoils with triangular protuberances.

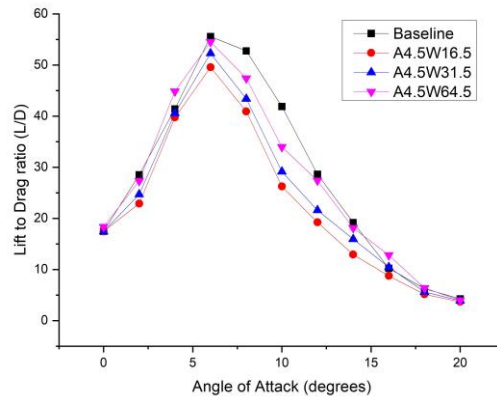
Configuration	E216			SG6043		
	$C_{lmax}$	$\alpha_{stall}$	$(L/D)_{max}$	$C_{lmax}$	$\alpha_{stall}$	$(L/D)_{max}$
A4.5W16.5	1.39	16	38.3	1.19	16	49.57
A4.5W31.5	1.46	16	40.6	1.24	16	52.3
A4.5W64.5	1.52	16	42.3	1.31	16	54.52
A9W16.5	1.29	14	30.1	1.15	14	48.12
A9W31.5	1.31	14	33.9	1.21	14	51.09
A9W64.5	1.36	14	35.4	1.29	14	53.11
A16.5W16.5	1.24	12	29.7	1.13	14	46.22
A16.5W31.5	1.27	12	31.3	1.18	14	48.17
A16.5W64.5	1.32	12	33.8	1.26	14	50.35
Baseline	1.35	12	36.2	1.37	14	55.6



(a)

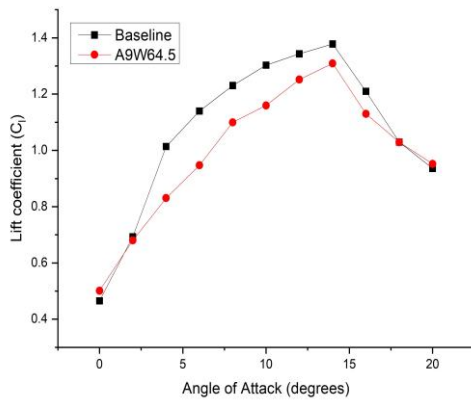


(b)

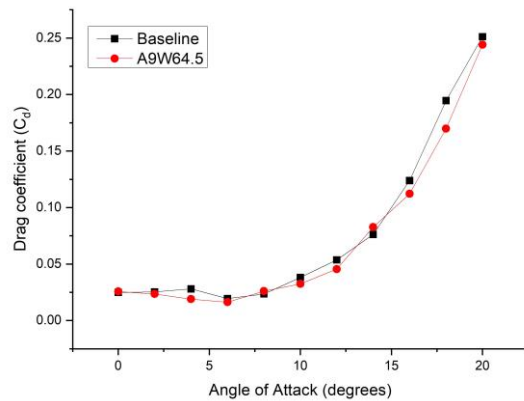


(c)

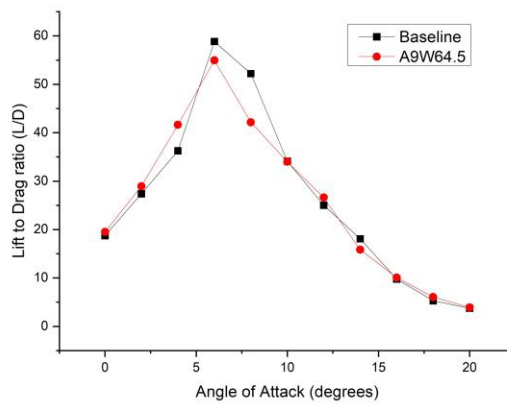
Figure 4.7: The effect of triangular protuberance wavelength on the aerodynamic parameters of the SG6043 airfoil at constant amplitude (a) Lift coefficient (b) Drag coefficient, and (c) Lift to drag ratio



(a)



(b)



(c)

Figure 4.8: The experimental results of the SG6043 baseline and the A9W64.5 triangular protuberance model (a) Lift coefficient (b) Drag coefficient, and (c) Lift to drag ratio

When the amplitude was held constant for both airfoil profiles,  $C_{lmax}$  and  $(L/D)_{max}$  increased with increasing wavelength, whereas when the wavelength was held constant,  $C_{lmax}$  and  $(L/D)_{max}$  decreased with increasing amplitude. In Fig. 4.7, the numerical results of  $C_l$ ,  $C_d$ , and  $L/D$  for various models of the SG6043 airfoil are plotted alongside baseline values. The lift curves in Fig. 4.7 (a) showed a decrease in prestall lift for all configurations and a slight increase in poststall lift for a longer-wavelength model. The protuberance configurations resulted in a greater zero  $C_l$ . Despite the stall delay, it was associated with a decrease in  $C_{lmax}$ . The drag curves in Fig. 4.7 (b) show that protuberance configurations had higher drag values than the baseline at angle of attack higher than  $12^\circ$ . In the high AOA range, the configuration with the lowest amplitude and lowest wavelength (i.e., A4.5W16.5) had the highest drag. The  $L/D$  curves in Fig. 4.7 (c) showed that all protuberance configurations had lower  $L/D$  values than the baseline.

The experimental force measurements of the A9W64.5 model were performed using the SG6043 airfoil and compared to baseline experimental values (Fig. 4.8). At an angle of attack of higher than  $16^\circ$ , there was a decrease in prestall lift followed by a marginal increase in poststall lift. The protuberance configuration had a higher zero-lift coefficient, which was also observed in numerical simulations. Drag values were comparable to baseline in the low angle of attack range. At angle of attack more than  $16^\circ$ , however, the baseline had a higher drag than the protuberance configuration, contradicting numerical simulation results.

Because drag measurement and prediction in the poststall region are difficult and sensitive to many variables, a dedicated study to address drag analysis in the poststall region should be conducted. The  $L/D$  ratio values were higher than baseline for protuberance configurations in the low angle of attack range, but comparable to baseline values in the high angle of attack range. The numerical results for the E216 baseline airfoil and the modified models were compared (Fig. 4.9). The lift curves shown in Fig. 4.9(a) show a decrease in prestall lift and an improvement in poststall lift. A delay in the stall was linked to an increase in  $C_{lmax}$ . Drag coefficient values of protuberance configurations are comparable to baseline until an angle of attack of  $10^\circ$ , but higher at high angle of attack, according to the drag curves in Fig. 4.9 (b).

The baseline curve was above the L/D curves of protuberance configurations (Fig. 4.9c). An increasing trend with wavelength was observed, with the A4.5W64.5 configuration having the highest  $(L/D)_{\max}$ . The experimental force measurements were carried out for the A9W64.5 configuration at the maximum amplitude and wavelength. These nondimensional experimental coefficients were compared to the baseline experimental values (Fig. 4.10). We observed an improvement in lift performance in both the prestall and poststall regimes based on the lift curves shown in Fig. 4.10(a). In numerical simulation, only poststall improvement was captured. Drag values of protuberance configurations were higher than baseline at a high angle of attack, as shown by the drag curves in Fig. 4.10(b), which was also observed in simulations. The L/D ratio values matched the baseline values (Fig. 4.10(c)).

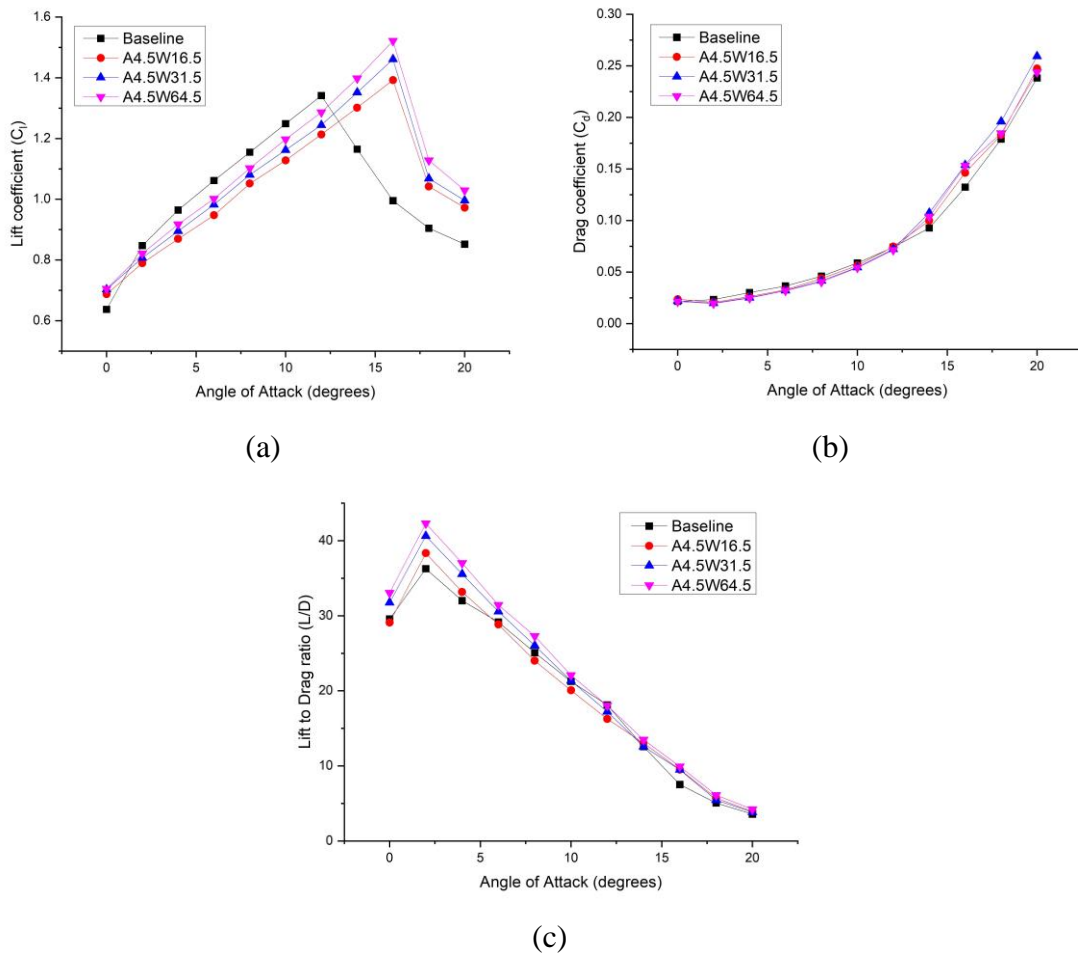


Figure 4.9: The effect of triangular protuberance wavelength on the aerodynamic parameters of an E216 airfoil with constant amplitude (a) Lift coefficient (b) Drag coefficient, and (c) Lift to drag ratio

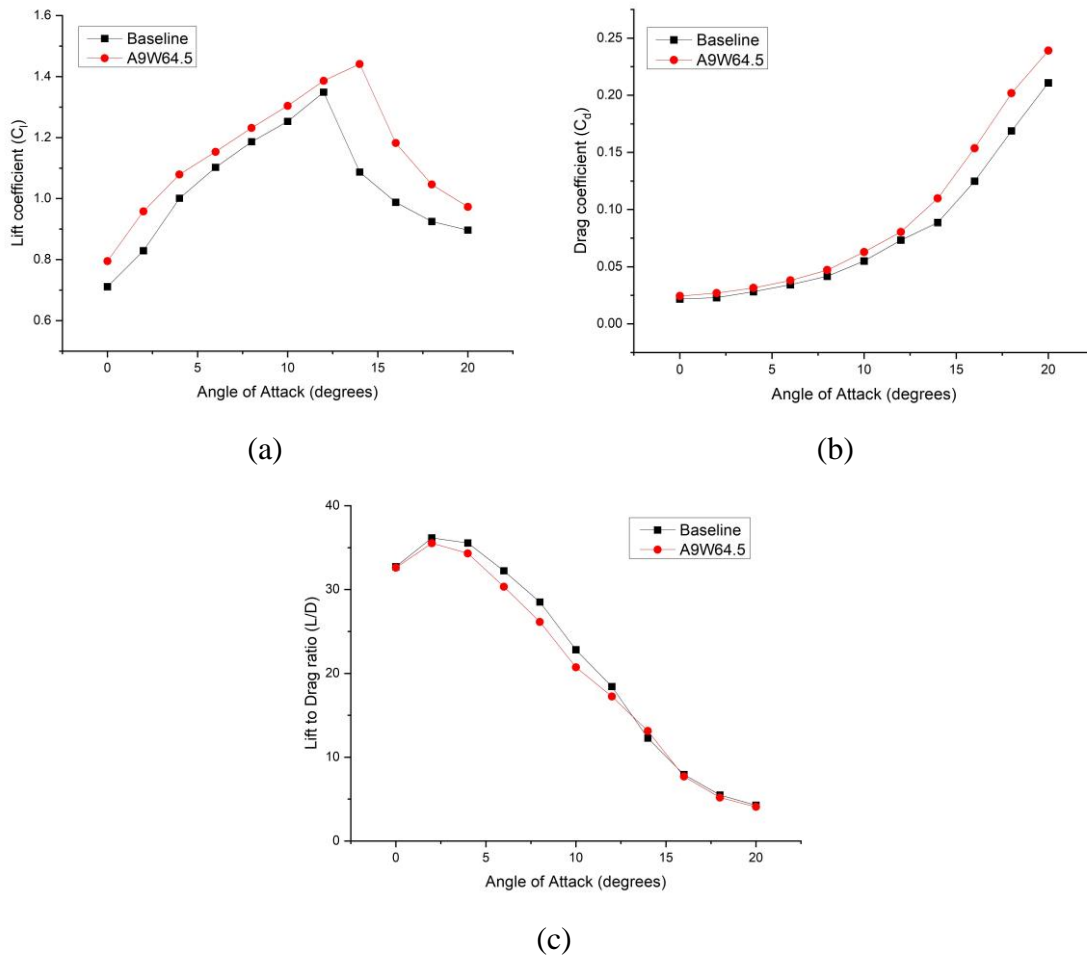


Figure 4.10: The experimental results of the E216 baseline and the A9W64.5 triangular protuberance model (a) Lift coefficient (b) Drag coefficient, and (c) Lift to drag ratio.

### 4.3.3 Slot Protuberances

Table 4.3 compares and lists the numerical results of various configurations of E216 and SG6043 airfoils. All configurations of both airfoils exhibited stall delays ranging from  $2^\circ$  to  $4^\circ$ . Most protuberance configurations for the E216 airfoil improved the  $C_{l_{max}}$  while also delaying stall. The  $L/D_{max}$  was improved in the lowest amplitude configurations. According to the lift curves shown in Fig. 4.11(a), all configurations had a decrease in prestall lift, while high wavelength designs had a slight improvement in poststall lift.

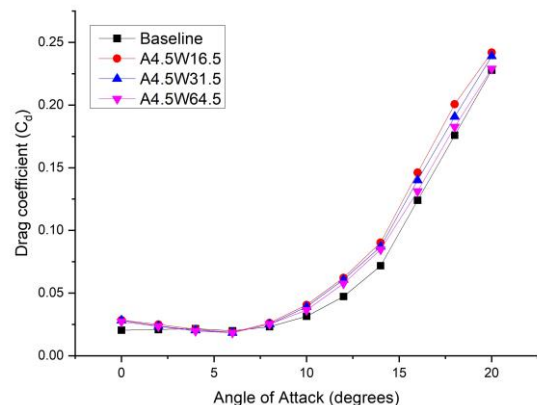
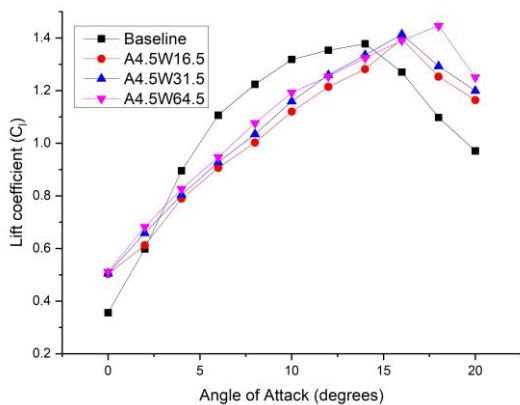
Significant zero lift coefficients are provided by protuberance designs. Although there was a stall delay, it was linked to a decrease in  $C_{l_{max}}$ . As shown in Fig. 4.11(b), the drag values of protuberance configurations were significantly higher than the baseline values. In the high angle of attack range, the configuration with the smallest amplitude and shortest wavelength, A4.5W16.5, had the most drag. As shown in Fig. 4.11(c), all of the protuberance designs

produced lower L/D values than the baseline. The maximum wavelength and optimum amplitude A9W64.5 configuration were tested for force measurements. These experimental nondimensional coefficients were compared to baseline experimental values, as shown in Fig. 4.12. A decrease in prestall lift was observed, followed by a significant increase in the stall and poststall areas.

Table 4.3: The aerodynamic performance of the E216 and SG6043 airfoils with slot protuberances.

Configuration	E216			SG6043		
	$C_{lmax}$	$\alpha_{stall}$	$(L/D)_{max}$	$C_{lmax}$	$\alpha_{stall}$	$(L/D)_{max}$
A4.5W16.5	1.38	16	35.8	1.39	16	48.47
A4.5W31.5	1.42	16	37.1	1.41	16	50.46
A4.5W64.5	1.45	16	39.3	1.44	18	51.81
A9W16.5	1.36	14	33.8	1.29	16	44.61
A9W31.5	1.39	14	35.9	1.33	16	46.8
A9W64.5	1.41	14	37.6	1.36	16	50.73
A16.5W16.5	1.29	14	29.5	1.22	16	43.40
A16.5W31.5	1.34	14	32.5	1.28	16	45.57
A16.5W64.5	1.37	14	35.7	1.32	16	47.88
Baseline	1.35	12	36.2	1.37	14	55.6

The zero-lift coefficient was significant for protuberance configurations, as demonstrated by numerical simulations. In the low angle of attack range, the drag values were similar to baseline values; however, the baseline had lower drag than the protuberance configuration in the stall and post stall regions. Because drag measurement and prediction in the poststall zone are complex and dependent on numerous variables, studies addressing drag analysis in the poststall region should be conducted.



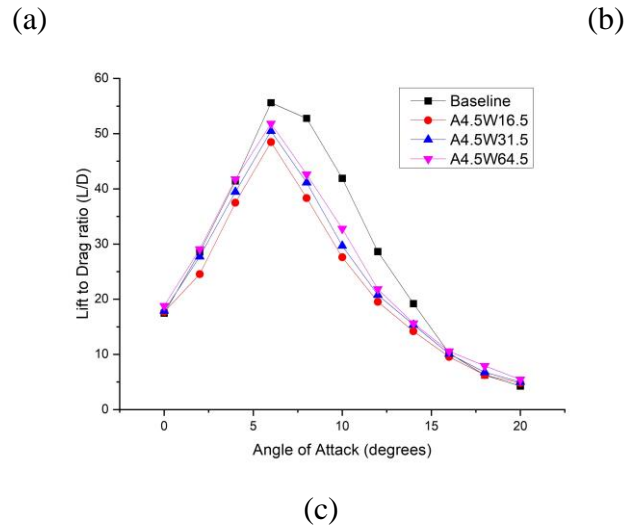
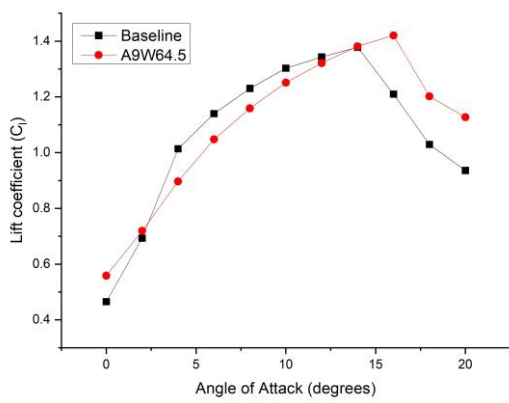
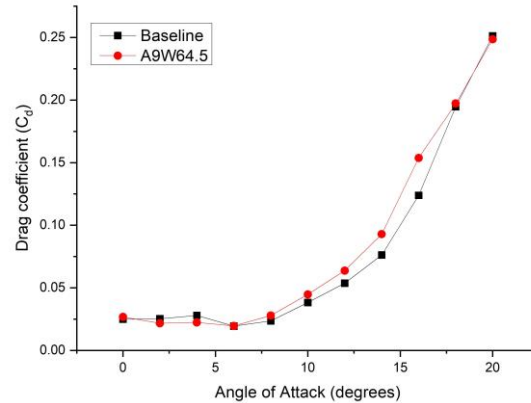


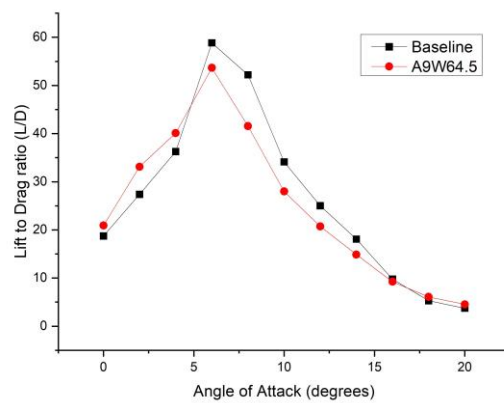
Figure 4.11: The effect of slot protuberance wavelength on the aerodynamic parameters of the SG6043 airfoil at constant amplitude (a) Lift coefficient (b) Drag coefficient, and (c) Lift to drag ratio.



(a)



(b)



(c)

Figure 4.12: The experimental results of the SG6043 baseline and the A9W64.5 slot protuberance model (a) Lift coefficient (b) Drag coefficient, and (c) Lift to drag ratio.

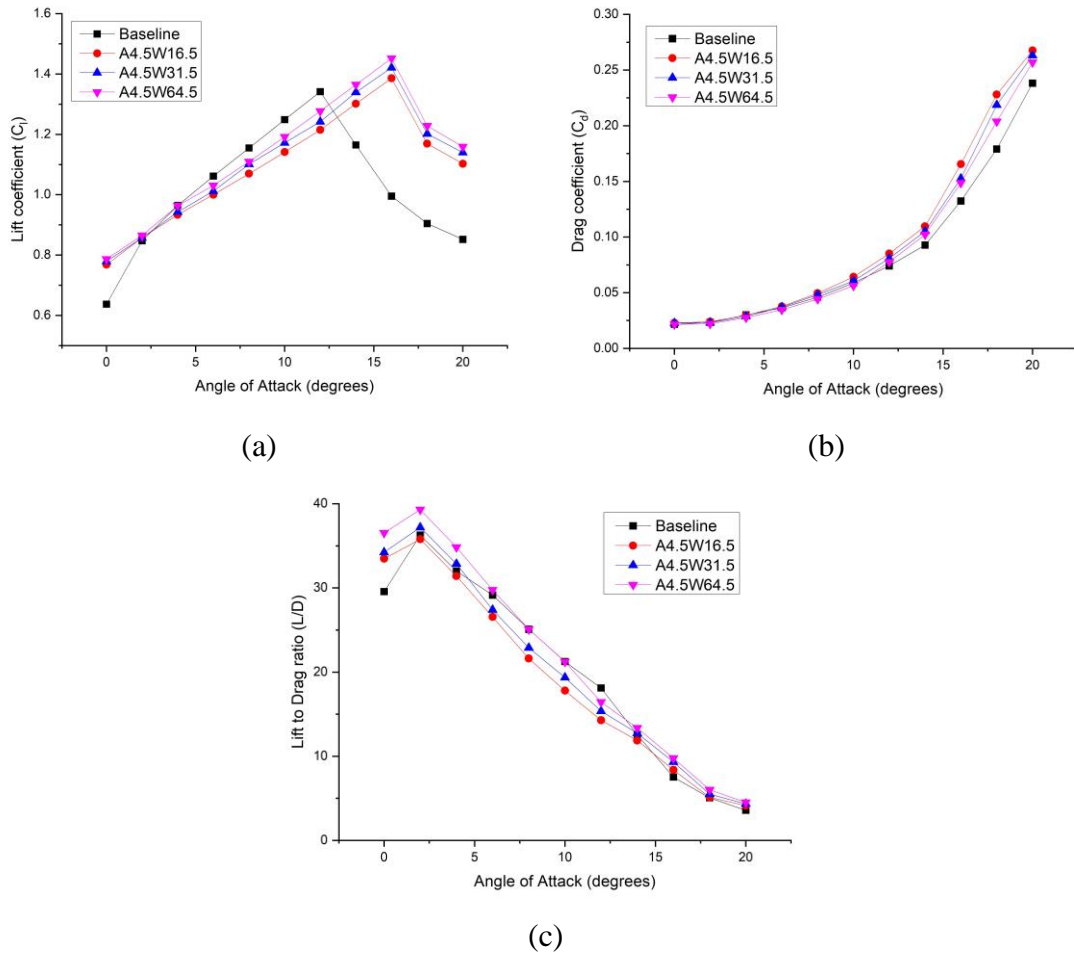


Figure 4.13: The effect of slot protuberance wavelength on the aerodynamic parameters of an E216 airfoil with constant amplitude (a) Lift coefficient (b) Drag coefficient, and (c) Lift to drag ratio.

The L/D ratio was greater than baseline in the low angle of attack range, but it is equivalent to baseline in the high angle of attack range. As shown in Fig. 4.13, the numerical results are plotted and compared to the baseline. Figure 4.13(a) shows a significant improvement in poststall lift performance. Prestall lift degradation was reduced in other protuberance shapes, and lift values were comparable to the baseline configuration. Furthermore, an increase in the zero-lift coefficient was observed. The drag curves in Fig. 4.13(b) showed that the drag values of slot configurations were unaffected until an angle of attack of  $12^\circ$ , after which they exhibited higher drag than the baseline. At a high angle of attack, A4.5W16.5 had the highest

drag of the configurations tested. Although the  $(L/D_{max})$  improved in Fig. 4.13(c), the  $(L/D)$  values of slot configurations were lower in the majority of the angle of attack ranges.

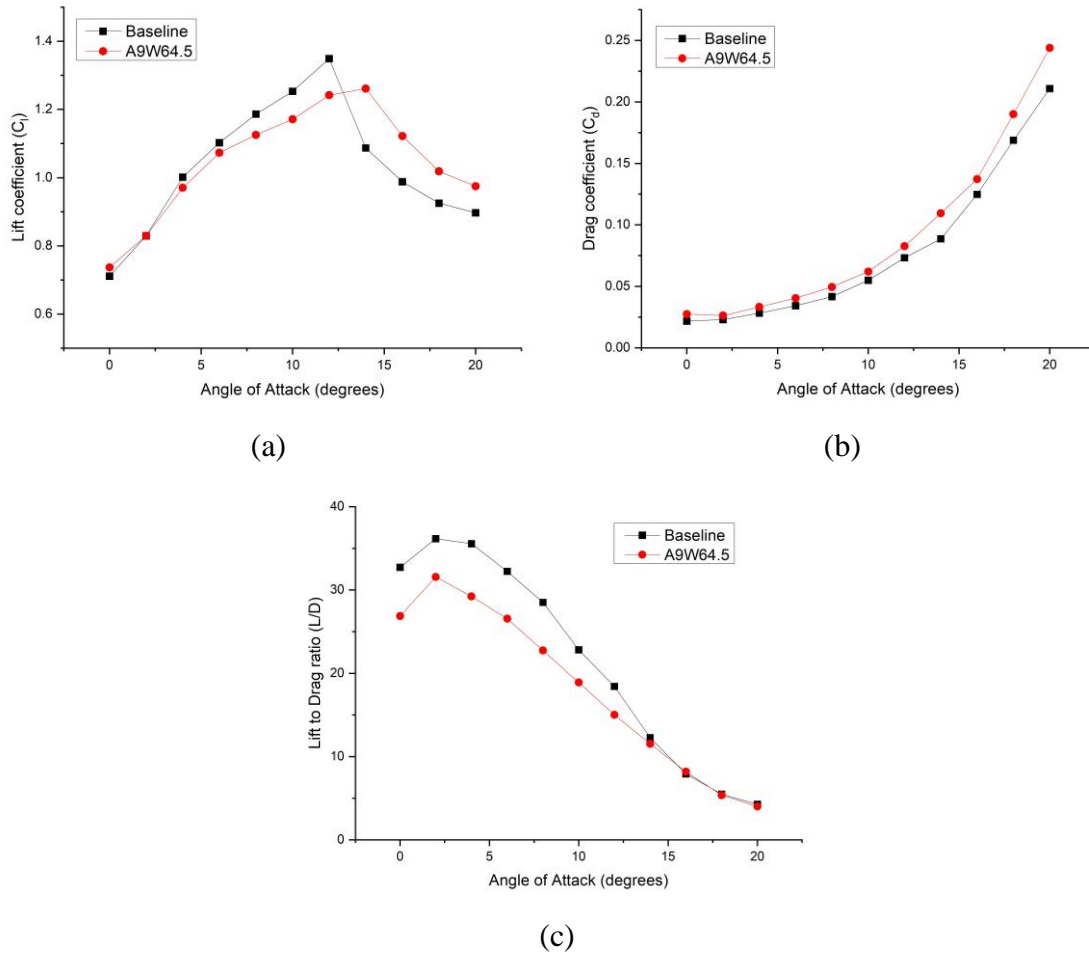


Figure 4.14: The experimental results of the E216 baseline and the A9W64.5 slot protuberance model (a) Lift coefficient (b) Drag coefficient, and (c) Lift to drag ratio.

Force experiments were carried out with the configuration A9W64.5 slots, and the results are shown in Fig. 4.14. In the experimental curves shown in Fig. 4.14(a), poststall lift improved while prestall lift degraded slightly. Overall drag values for slot configuration were higher than the baseline, and L/D values degraded until an angle of attack of  $14^\circ$ .

#### 4.3.4 Effect of Distinct Airfoil Profiles

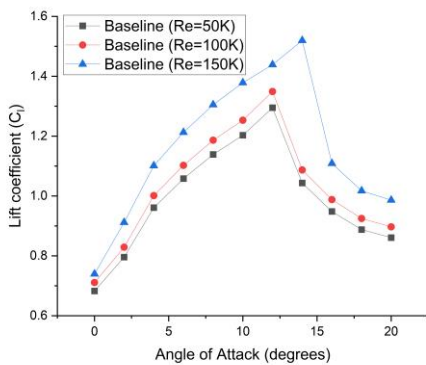
In the baseline configuration, the SG6043 airfoil had a higher stall and  $C_{lmax}$  than the E216 airfoil. An airfoil's maximum lift coefficient is determined by its geometrical parameters: thickness ratio, leading edge radius, camber, and maximum thickness location. The maximum thickness-to-chord ratio  $(t/c)_{max}$  for the E216 airfoil is 10.4% at 26.2% chord and the

maximum camber was 4.7% at 59% chord. The maximum  $(t/c)_{\max}$  for the SG6043 airfoil was 10% at 32.1% chord, and the maximum camber was 5.1% at 53.3% chord. These values contribute to SG6043 having a higher  $C_{l_{\max}}$ . The SG6043 airfoil has a larger leading-edge radius than the E216 airfoil, as shown in Table 3.3. A large upper surface leading-edge radius reduced peak negative pressure coefficients, postponing stall to a higher angle of attack (Roskam and Lan, 1997). As a result, the stall angle of the SG6043 airfoil was greater than that of the E216 airfoil.

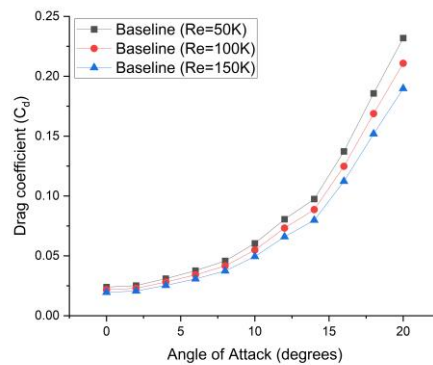
According to the preceding sections, the effect of leading-edge protuberances is dependent on the airfoil to which it is applied. In general, leading-edge protuberances benefited E216 more than SG6043. Among the examined protuberance shapes, the shape of the slot improved performance the most for both airfoil profiles. Hansen *et al.* (2011) hypothesised that when the maximum thickness position is further aft, the boundary layer expanse is larger, implying that tubercles may be more advantageous. However, the current study's findings contradict Hansen's hypothesis. This can be attributed to the similarity of the chosen profiles and the difference in maximum thickness positions, which was less than 10%.

#### 4.3.5 Reynolds Number effect

The lift coefficient of the baseline and protuberance airfoils is depicted in Figure 4.15 as a function of angle of attack, spanning Reynolds numbers from 50K to 150K. The observed behavior of the lift coefficient aligns with the expected pattern for the thin airfoil profile under examination.

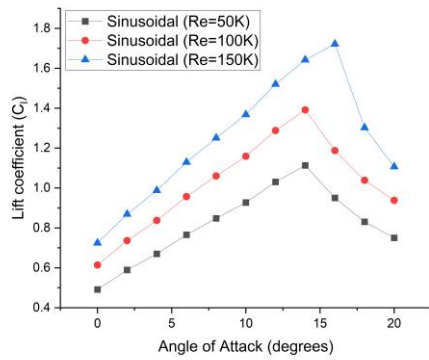


(i) Lift coefficient

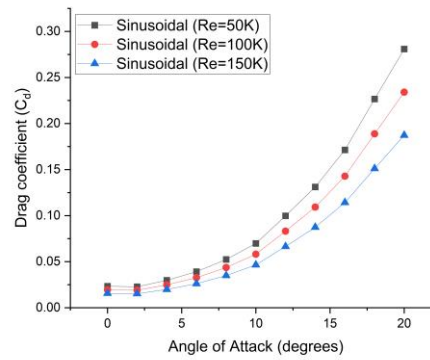


(ii) Drag coefficient

(a) E216 Baseline

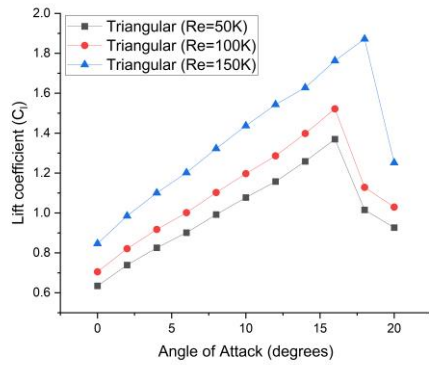


(i) Lift coefficient

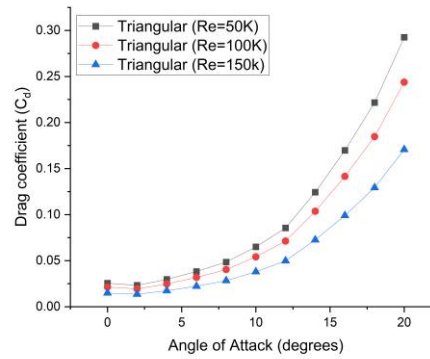


(ii) Drag coefficient

(b) E216 Sinusoidal

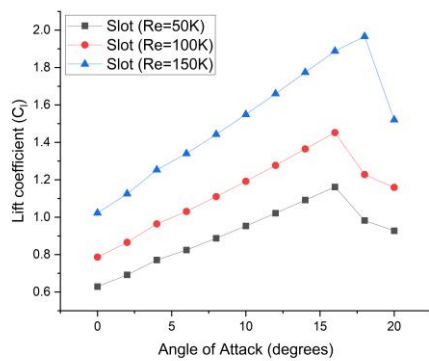


(i) Lift coefficient

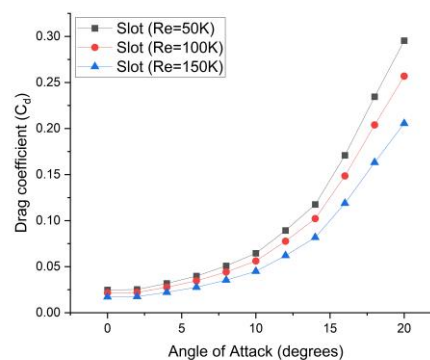


(ii) Drag coefficient

(c) E216 Triangular



(i) Lift coefficient



(ii) Drag coefficient

(d) E216 Slot

Figure 4.15: Effect of Reynolds number on the (a) baseline, (b) sinusoidal, (c) triangular, and (d) slot protuberance models.

Across all tested Reynolds numbers, there is a consistent linear increase in  $C_l$  until a certain point. Notably, as the angle of attack rises beyond this threshold, flow separation becomes apparent in the drag characteristics, leading to a rapid increase in  $C_d$  at higher angles of attack after the stall. The  $C_{lmax}$  values for baseline airfoil observed are 1.295, 1.348, and 1.519 for Reynolds numbers of 50K, 100K, and 150K, respectively. Specifically, the stall occurs at  $14^\circ$  for the 150K Reynolds number, while in the remaining two cases stall happens at  $12^\circ$ . Following the stall, there is a significant drop in  $C_l$  within the range of  $12^\circ$  to  $16^\circ$ , which stabilizes thereafter. Following the stall point, the drag coefficient undergoes an abrupt rise with changing angles of attack due to phenomena related to flow separation and subsequent reattachments. Aerodynamic parameters of E216 baseline and modified airfoils at 50K, 100K, and 150K Reynolds numbers are tabulated in Table 4.4.

In the sinusoidal protuberance model,  $C_{lmax}$  measured 1.112, 1.391, and 1.721 for Reynolds numbers of 50K, 100K, and 150K, respectively. At 150K Reynolds number, stall occurs at the angle of attack  $16^\circ$ , while the other cases at  $14^\circ$ . Compared to the baseline, there is a 14.05% reduction in  $C_{lmax}$  at 50K Reynolds number, whereas, at 100K and 150K Reynolds numbers,  $C_{lmax}$  increases by 3.18% and 13.29% respectively. Across the range, there's a consistent stall delay of up to  $2^\circ$  compared to the baseline. The lift and drag behaviors are consistent, with no abrupt rises or drops across the considered range, as opposed to the baseline.

Table 4.4: Aerodynamic parameters of E216 baseline and modified airfoils at 50K, 100K, and 150K Reynolds numbers

Airfoil Configuration	Reynolds Number	Stall angle	$C_{lmax}$	$C_{lmax}$ improvement
Baseline	50,000	12	1.295	-
	1,00,000	12	1.348	-
	1,50,000	14	1.519	-
Sinusoidal	50,000	14	1.113	-14.05%
	1,00,000	14	1.391	+3.18%
	1,50,000	16	1.721	+13.29%
Triangular	50,000	16	1.369	+5.71%
	1,00,000	16	1.521	+12.83%
	1,50,000	18	1.872	+23.23%
Slot	50,000	16	1.161	-10.34%
	1,00,000	16	1.451	+7.64%
	1,50,000	18	1.966	+29.42%

The lift coefficients of triangular protuberance model were found to be 1.369, 1.521, and 1.872 corresponding to Reynolds numbers of 50K, 100K, and 150K, respectively. Notably, the stall occurs at  $18^\circ$  for the 150K Reynolds number, while for the other cases, stall is observed at the angle of attack  $16^\circ$ . In comparison to baseline results, there is a notable increase in  $C_{lmax}$  by 5.71%, 12.83%, and 23.23% for Reynolds numbers of 50K, 100K, and 150K, respectively. A stall delay of up to  $4^\circ$  is apparent across all cases when contrasted with the baseline.

In slot protuberance results the maximum lift coefficient observed was 1.966 at a Reynolds number of 150K, which was the highest among all protuberance configurations. For the 150K Reynolds number, stall occurred at the angle of attack  $18^\circ$ , while other cases at  $16^\circ$ . When compared to baseline results, a significant 7.64% and 29.42% increase in  $C_{lmax}$  was observed for Reynolds numbers of 100K and 150K. In comparison to the baseline, there was a stall delay of up to  $4^\circ$  in all scenarios

## **4.4 DYNAMIC STUDY**

Dynamic stall experiments were performed on the airfoil within an angle of attack range spanning from  $-5$  to  $15^\circ$ . The investigation encompassed three distinct reduced frequency values, specifically 0.025, 0.05, and 0.065.

### **4.4.1 Baseline**

Figure 4.16 shows the variation in lift coefficients for baseline airfoil at various reduced frequencies. As the angle of attack increases, the forward-moving reversed flow generates a powerful suction vortex at the leading edge. As the angle of attack increases further, this LEV separates from the airfoil to form a DSV. With further increase in angle of attack, the convection of DSV towards the trailing edge begins. At the same time, secondary vortices form on the leading edge, and vortices grow at the trailing edge.

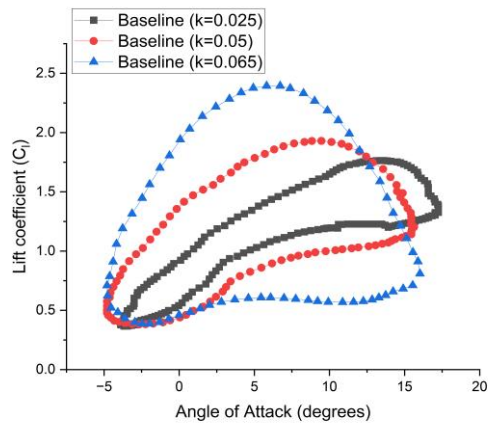


Figure 4.16: Lift coefficient variation with angle of attack for baseline airfoil at various reduced frequencies.

When the angle of attack is increased further, the trailing edge vortices and DSV completely detach from the airfoil, resulting in complete flow separation and thus dynamic stall (Wei *et al.* 2021).

At a reduced frequency of 0.025, the lift coefficient exhibits a linear increase with the angle of attack during pitch-up, reaching  $C_{lmax}$  of 1.7 at 12° angle of attack. The stall onset is sustained from 12° to 15° angle of attack, and beyond this range, there is a sudden drop in lift coefficient, indicative of flow separation. Conversely, during pitch-down, the flow remains stable and nearly constant. Reattachment of the flow initiates at 6° angle of attack.

At reduced frequencies of 0.05 and 0.065, the lift coefficient demonstrates a rapid increase during pitch up with the angle of attack, yielding  $C_{lmax}$  values of 1.9 and 2.4 at angles of attack 10° and 8°, respectively. The size of the hysteresis loop expands proportionally with the increase in reduced frequency. Conversely, during pitch-down maneuvers, the flow exhibits instability, resulting in delayed reattachment.

The early stall initiation, despite the enhanced lift coefficient, presents a limitation to the overall performance. While the increase in reduced frequency can yield advantages in terms of lift coefficient, it is crucial to consider the associated stall characteristics. The stall and hysteresis characteristics of baseline and protuberance airfoils differ significantly, which will be discussed further in the following section.

#### 4.4.2 Sinusoidal protuberances

Much like the baseline airfoil, the sinusoidal protuberance airfoil also exhibits a trend where an increase in reduced frequency corresponds to a higher maximum lift coefficient shown in Figure 4.17. With a rise in reduced frequency, there is an observed increase in the hysteresis loop size as well. However, it's noteworthy that in the case of the sinusoidal protuberance airfoil, the hysteresis loop appears smaller, and reattachment initiates at an earlier stage compared to the baseline airfoil.

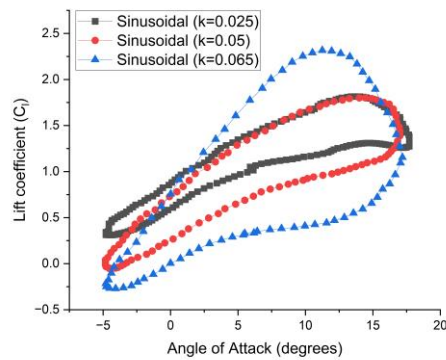


Figure 4.17: Lift coefficient variation with angle of attack for sinusoidal airfoil at various reduced frequencies.

At a reduced frequency of 0.025 and 0.05, the lift coefficient exhibits a linear increase with the angle of attack during pitch-up, reaching  $C_{l_{max}}$  of 1.7 and 1.8 at  $12^\circ$  angle of attack. The stall onset is sustained from  $12^\circ$  to  $15^\circ$  angle of attack, and beyond this range, there is a gradual drop in lift coefficient, indicative of flow separation. Conversely, during pitch-down, the flow remains stable and nearly constant. Reattachment of the flow initiates at  $8^\circ$  angle of attack.

At reduced frequency 0.065, the lift coefficient demonstrates a rapid increase during pitch up with the angle of attack, yielding  $C_{l_{max}}$  values of 2.4 at angles of attack  $10^\circ$ . During pitch-down, the flow remains stable and reattachment of the flow initiates early compared with the baseline. The size of the hysteresis loop increases with the increase in reduced frequency for sinusoidal model. But comparing with the baseline the size of the hysteresis loop is small in sinusoidal protuberance case.

The incorporation of sinusoidal protuberances facilitated secondary flow through the troughs, contributing to improved lift characteristics in the post-stall region. This is a critical

advantage attributed to the presence of protuberances, showcasing more favorable aerodynamic behaviors.

#### 4.4.3 Triangular protuberances

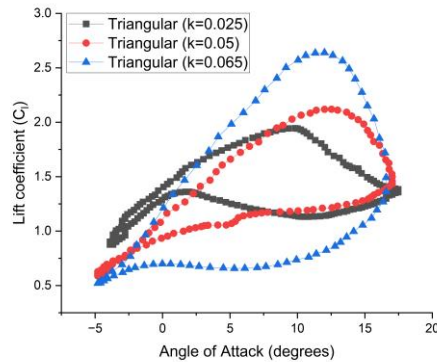


Figure 4.18: Lift coefficient variation with angle of attack for triangular airfoil at various reduced frequencies.

In the study analyzing triangular protuberances under dynamic conditions as depicted in Figure 4.18. The presence of triangular protuberances with sharp edges at the leading edge peak and troughs, as well as a wavy surface along the chordwise, allowed for increased secondary airflow through the troughs, resulting in improved lift characteristics, particularly in the post-stall region. For reduced frequency 0.065, the maximum lift coefficient reached 2.7 at a angle of attack  $10^\circ$ . Stall onset within the range of  $8$  to  $12^\circ$  was observed for the 0.05 reduced frequency, reaching a maximum lift coefficient of approximately 2.3. And for the 0.025 reduced frequency, the maximum lift coefficient reached 2.1 at an angle of attack  $8^\circ$ . The dynamic hysteresis loop observed in the airfoil with triangular protuberances was small compared with the baseline.

#### 4.4.4 Slot protuberances

Reduced frequency increases, the maximum lift coefficient increases in slot protuberance model shown in Figure 4.19. At reduced frequency of 0.065, the maximum lift coefficient is higher than in the baseline configuration. At reduced frequency of 0.065, the airfoil demonstrates  $C_{l_{max}}$  value of 2.7. This peak  $C_{l_{max}}$  value is achieved at a stall angle of  $12^\circ$ .

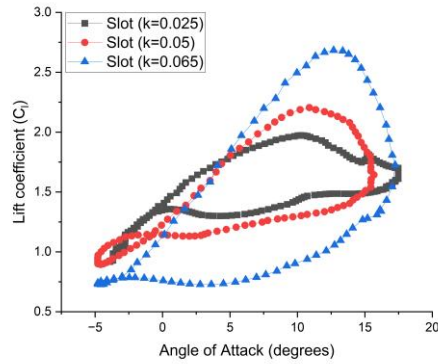


Figure 4.19: Lift coefficient variation with angle of attack for slot airfoil at various reduced frequencies.

At a reduced frequency of 0.025 and 0.05, the lift coefficient exhibits a linear increase with the angle of attack during pitch-up, reaching  $C_{lmax}$  of 1.9 and 2.2 at  $10^\circ$  angle of attack. Further increase in angle of attack there is a gradual drop in lift coefficient, indicative of flow separation. Conversely, during pitch-down, the flow remains stable and nearly constant. Reattachment of the flow initiates early compared with baseline. In the case of slot protuberances, a consistent trend is observed: the size of the hysteresis loop expands with higher reduced frequencies, as seen in both baseline and other protuberance cases.

#### 4.4.5 EFFECT OF PROTUBERANCES AT CONSTANT FREQUENCY

The effect of protuberances on dynamic stall at constant reduced frequency of 0.025, 0.05, and 0.065 is shown in Figure 4.20. For reduced frequency 0.025,  $C_{lmax}$  was observed as 1.7, 1.8, 1.9 and 2 for baseline, sinusoidal, triangular and slot protuberance models. For reduced frequency 0.05,  $C_{lmax}$  was observed as 1.9, 1.8, 2.2 and 2.3 for baseline, sinusoidal, triangular and slot protuberance models. And for reduced frequency 0.065,  $C_{lmax}$  was observed as 2.2, 2.3, 2.6 and 2.7 for baseline, sinusoidal, triangular and slot protuberance models.

It is also observed that for three reduced frequencies the baseline model results in less  $C_{lmax}$  compared with protuberance models. The hysteresis loop is small for all protuberance models compared with baseline across three reduced frequencies. A significant departure from the baseline occurred at the 0.065 reduced frequency, where the protuberance models prevented the sudden drop in  $C_l$  after stall. This is a critical advantage attributed to the presence of protuberances, showcasing more favorable aerodynamic behaviors. It is also observed that, the slot and triangular protuberance models reattachment during pitch down is smooth and begins early compared with baseline for reduced frequencies 0.025 and 0.05. Overall slot and

triangular protuberance models showcasing improved aerodynamic efficiency at 0.025 and 0.05 reduced frequencies compared with baseline model.

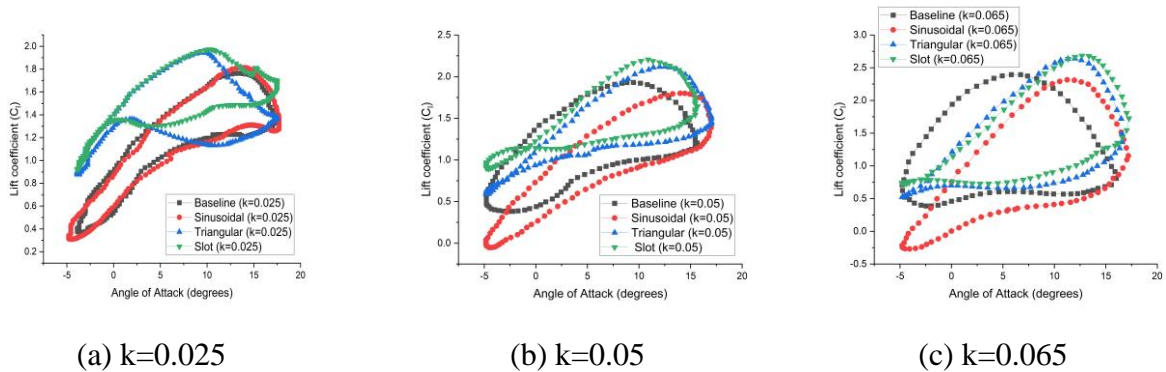


Figure 4.20: Aerodynamic performance comparison of protuberance models with baseline at various reduced frequencies (a)  $k = 0.025$ , (b)  $k=0.05$ , and (c)  $k=0.65$ .

## 4.5 WORKING MECHANISM OF LEADING-EDGE PROTUBERANCES

Miklosovic *et al.* (2004), Hansen *et al.* (2011), Van Nierop *et al.* (2008), Fletcher (1975) and Johari *et al.* (2007), have proposed various explanations for the functionality of leading-edge protuberances. The most frequently cited mechanisms involve the generation of streamwise vortices and comparisons to vortex generators. To understand the underlying flow dynamics, we examined vorticity magnitude and Turbulent Kinetic Energy (TKE) contours in both spanwise and streamwise directions in this study. Multiple slices were generated in the streamwise direction at various points, including the leading edge, mid-chord, trailing edge, and far-field regions. The term "X-vorticity" refers to a critical parameter in fluid dynamics that denotes the curl of the velocity as a measure of fluid rotation in the X-direction (aligned with the flow direction).

### 4.5.1 Sinusoidal Protuberances

Figures 4.21 (a) and (b) show the X vorticity and overall vorticity magnitude contours at these slices for an A4.5W64.5 configuration with sinusoidal protuberances at an angle of attack of  $0^\circ$ . Figure 4.21 (a) shows the generation of counter-rotating vortices from the leading-edge protuberance region and their passage in the streamwise direction. Because of the presence of the airfoil, the downstream flow was split into two high vorticity regions after passing through the trailing edge, as shown in Figure 4.21 (b). As shown in Figure 4.22, the intensity of these

counter-rotating vortices decreased as they grew in the streamwise direction. This behaviour is similar to that of vortex generators (VG) producing streamwise vortices (Godard and Stanislas, 2006).

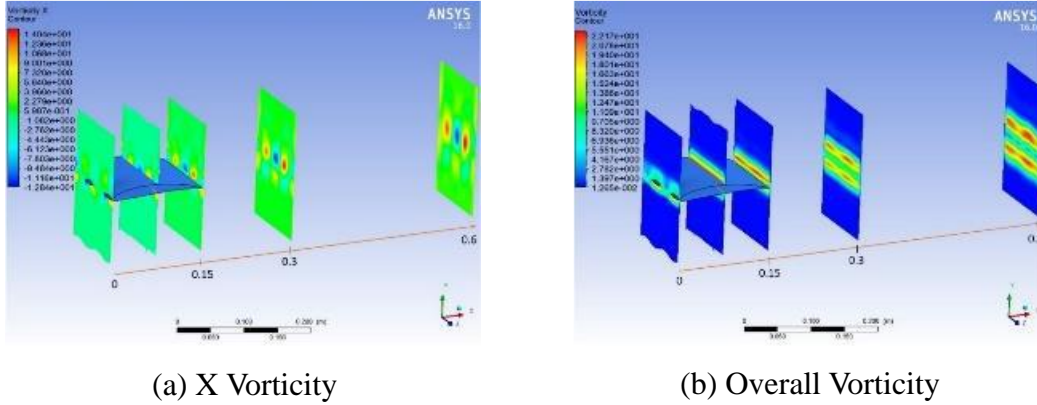


Figure 4.21: Contours of vorticity magnitude for A4.5W64.5 configuration with sinusoidal protuberances at an angle of attack of  $0^\circ$ .

Even at a stall angle of  $16^\circ$ , this behaviour remained consistent. In the case of VGs, these vortices energise the boundary layer, causing flow separation to be delayed. The TKE contour analysis should be used to conduct additional research on the flow physics of leading-edge protuberances.

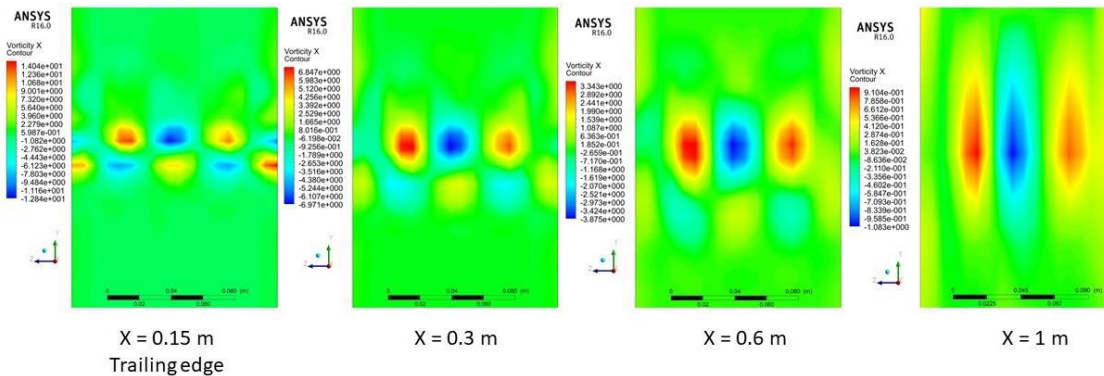


Figure 4.22: Counter-rotating vortices generated by A4.5W64.5 sinusoidal protuberances in a streamwise direction at an angle of attack  $0^\circ$ .

The TKE contours in the spanwise direction of an A4.5W64.5 configuration with sinusoidal protuberances at zero and stall angles are shown in Figure 4.23(a). TKE is a direct measure of flow turbulence. The contours at a zero angle are similar in the peak and trough regions. The flow becomes turbulent at approximately 50% of the chord at a stall angle behind the peak region, then reattaches near the trailing edge, forming a separation bubble. However, the flow

separates near the trailing edge in the trough region, resulting in a significant increase in TKE magnitude after the trailing edge.

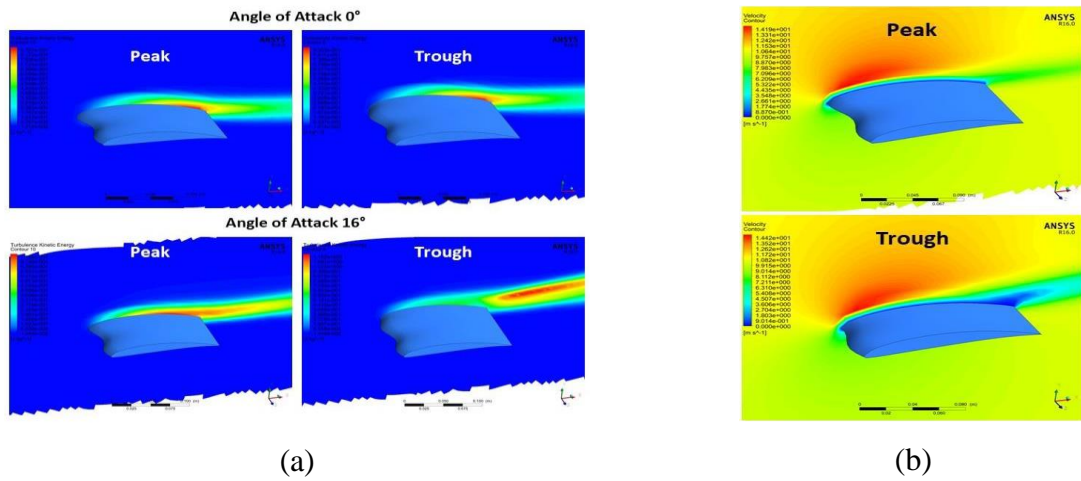


Figure 4.23: (a) TKE contours at peak and trough regions at angle of attacks  $0^\circ$  and  $16^\circ$  (b) Velocity contours at peak and trough regions at  $16^\circ$  angle.

Flow separation begins in the trough region. Previous wind tunnel experiments (Johari *et al.* (2007)) and numerical simulations (Fish and Lauder, 2006) revealed similar flow behaviour. This is also confirmed by examining velocity contours at stall angles, as shown in Figure 4.23 (b), which shows a region of zero velocity at the trailing edge. At a higher angle of attack, the velocity field generated by leading-edge protuberances is variable along the span, as seen in previous stereoscopic particle image velocimetry measurements (Esmaeili *et al.* 2018).

#### 4.5.2 Triangular Protuberances

Triangular protuberances generate counter-rotating vortices similar to sinusoidal vortices. They differ from other protuberances in their occurrence, behaviour, and strength. They are numerically represented by considering X vorticity contours at various streamwise slices for the A4.5W64.5 configuration with triangular protuberances at  $0^\circ$  angle (Figure 4.24).

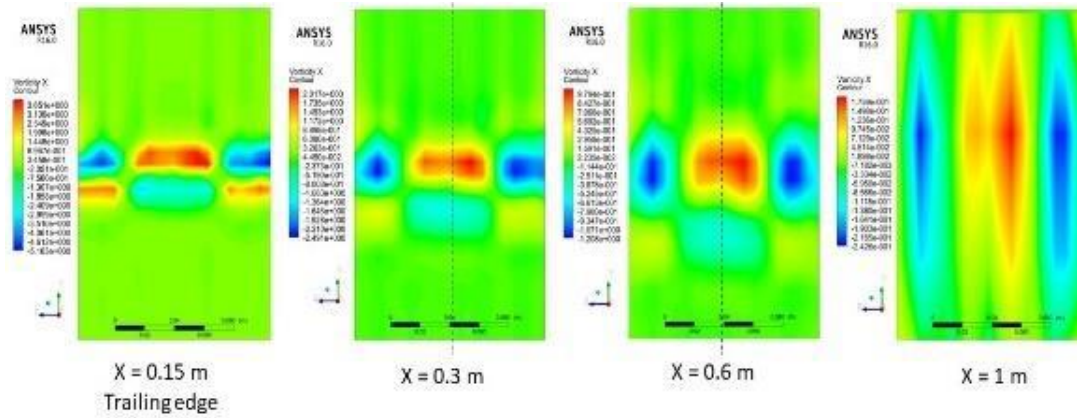


Figure 4.24: Counter-rotating vortices are visualized at different streamwise slices for A4.5W64.5 configuration with triangular protuberances at  $0^\circ$  angle of attack.

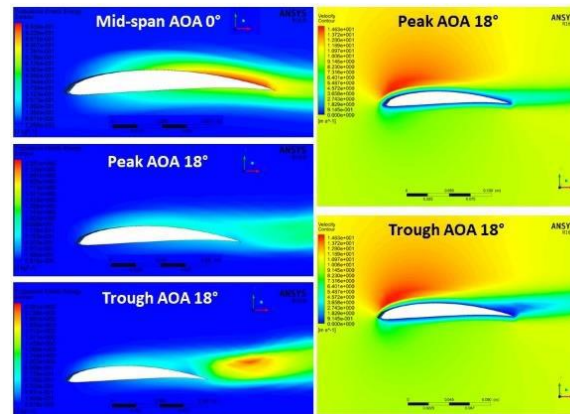


Figure 4.25: Contours of TKE and velocity magnitude at peak and trough regions of A4.5W64.5 configuration with triangular protuberances at angles  $0^\circ$  and  $18^\circ$ .

We discovered that counter-rotating vortex pairs generated behind adjacent protuberances were symmetric using the contours at  $X = 0.3$  m and  $0.6$  m. A significant increase in vortices size after  $X = 0.6$  m in the streamwise direction was associated with a decrease in intensity. Even at stall angles, the behaviour was consistent. The magnitudes of overall vorticity were found to be less than those of sinusoidal protuberances.

Figure 4.25 depicts TKE and velocity magnitude contours at the mid-span, peak, and trough regions of the A4.5W64.5 configuration with triangular protuberances at  $0^\circ$  and  $18^\circ$ . There was no variation in TKE along the spanwise direction at  $0^\circ$ . This represents the formation of a separation bubble near the trailing edge. TKE was different at the peak and trough regions at a stall angle ( $18^\circ$ ). Although no separation bubbles were observed, the separation began at the

trough region. Examining the velocity magnitude contours at peak and trough regions confirms this.

### 4.5.3 Slot Protuberances

As shown in Figure 4.26 (a), the leading-edge slots model (i.e., the A4.5W64.5 configuration) generated a pair of counter-rotating vortices associated with two slots. These vortices grew in size and intensity as they moved in a streamwise direction. These vortices were more powerful than triangular and sinusoidal protuberances.

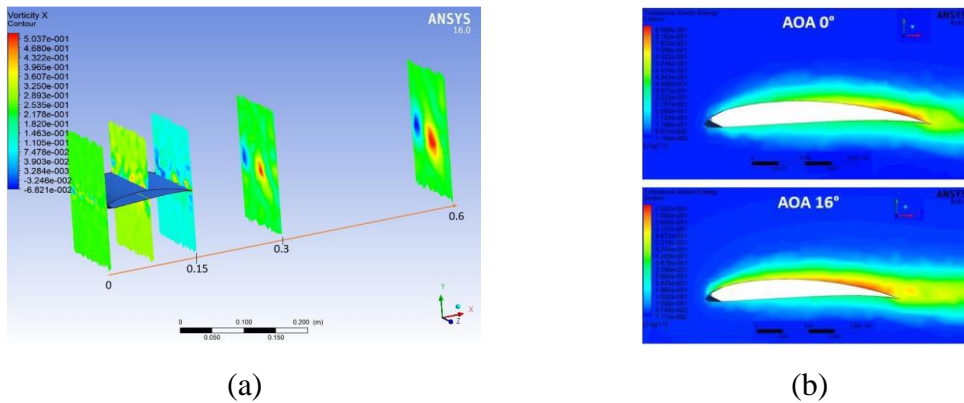


Figure 4.26: (a) X vorticity contours at streamwise slices at  $0^\circ$  angle and (b) TKE contours at  $0^\circ$  and  $16^\circ$  taken at slot regions of A4.5W64.5 configuration with slot protuberances.

At stall angles, similar vortex formation was observed. In the spanwise direction, the TKE field was constant. TKE contours at  $0^\circ$  and  $16^\circ$  observed at the slot region are shown in Figure 4.26 (b). A turbulent reattachment near the trailing edge can be seen in both cases. The three protuberance shapes' vortex behaviour leads to the following conclusions. Counter-rotating vortices are generated by all protuberance shapes. These vortices grow in size with decreasing intensity in the streamwise direction, similar to the behaviour of VG vortices. The vortex strength is highest in slots and lowest in triangular protuberances. Adjacent triangular protuberances generate symmetric vortices at an imaginary midpoint between them. A pair of counter-rotating vortices is produced by two distinct slots, whereas triangular and sinusoidal produce one pair per protuberance (one at peak and one at trough).

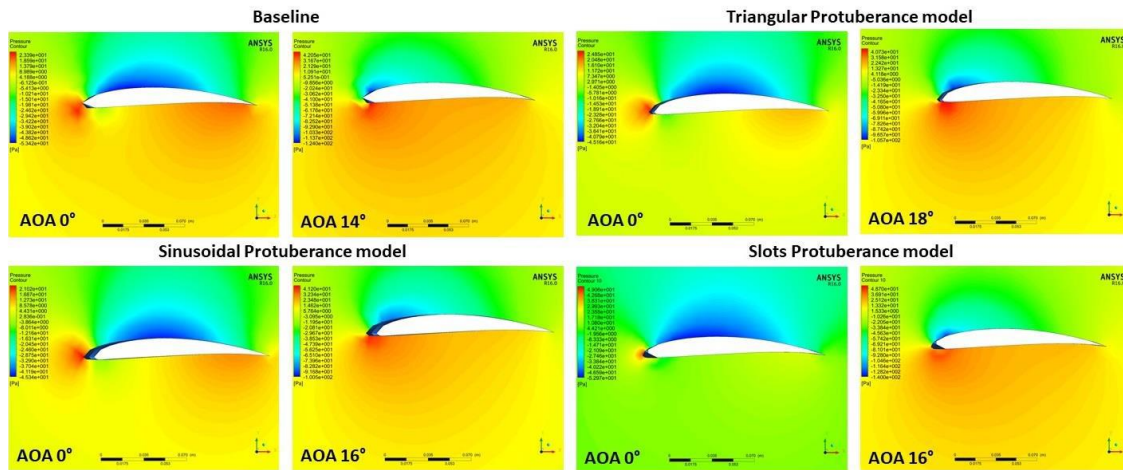


Figure 4.27: Comparison of pressure distributions of baseline and modified configurations at  $0^\circ$  and stall angles.

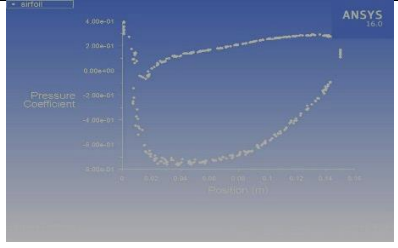
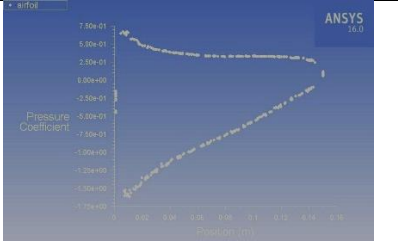
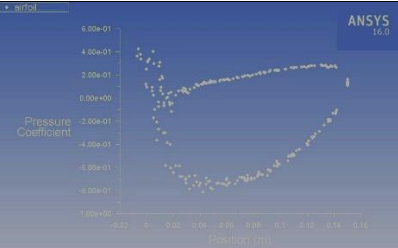
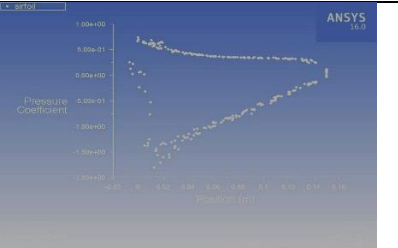
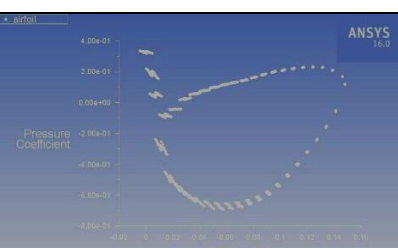
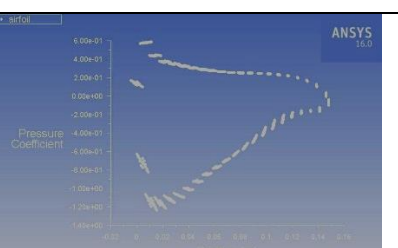

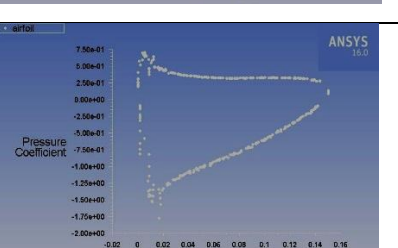
Based on vortex strength, slots shape result in the best performance in terms of stall delay and  $C_{lmax}$  improvement, which can be explained by vortex lift theory (Polhamus 1968) . The behaviour is similar to that of VG-generated vortices.

However, Van Nierop *et al.* (2008) claim that they can act as VGs because their amplitude and wavelength are greater than the boundary layer thickness. As a result, additional numerical studies should be carried out to investigate the effect of these protuberances on pressure distribution.

As shown in Figure 4.27, the pressure distributions of the baseline and modified configurations were compared at  $0^\circ$  and stall angles. The pressure distribution was significantly altered by the leading-edge protuberances. When compared to the baseline, the static pressure difference between suction and pressure surfaces was small for sinusoidal and triangular protuberances, whereas slots had significantly higher pressure differences. Variations in the coefficient of pressure ( $C_p$ ), a nondimensional parameter in the chordwise direction, can be used to study the pressure distribution generated by the airfoil. Because the difference in static pressure between an airfoil's upper and lower surfaces manifests as aerodynamic forces, chordwise variation was considered.

Table 4.5 compares chordwise variations for A9W64.5 configurations with different protuberance shapes to the baseline airfoil.

Table 4.5: Comparison of chordwise pressure coefficient variation for various configurations at zero and stall angles of attack

Configuration	Chordwise Variation of Coefficient of Pressure ( $C_p$ )	
	Angle of attack $0^\circ$	Stall angle of attack
Baseline		
A9W64.5 Sinusoidal		
A9W64.5 Triangular		
A9W64.5 Slots		

At zero and stall angles, the  $C_p$  plots of baseline and slots are nearly identical. Because the area covered by the  $C_p$  plot represents the generated aerodynamic forces, both produce the same amount of lift. The sinusoidal shape had the smallest area covered by  $C_p$  plots, which is reflected in lift curves, of the three protuberance shapes. Slots had the best performance in terms of  $C_{lmax}$ , stall delay, and poststall performance based on both vortex strength and

pressure distribution. To determine the precise mechanism responsible for the protuberance effect, the relative contributions of the two mechanisms should be investigated. Because of the higher static pressure, the triangular protuberances produced higher  $C_{lmax}$  values than the sinusoidal despite having low strength vortices. As a result, the change in pressure distribution, rather than vortex strength, is responsible for this result.

## **4.6 FLOW VISUALIZATION**

In this study, smoke and tuft flow visualization methods are employed to visually illustrate and study flow behaviour by tracing airflow patterns using smoke particles and tufts of yarn.

Smoke flow visualization method involves introducing smoke into a flow field, which allows for the observation of flow behavior around the airfoil as well as the understanding of invisible phenomena like turbulence, separation, and vortices. Its importance lies in providing qualitative insights into aerodynamic behaviors, assisting with design optimization, and validating computational models. This cost-effective technique provides a practical way to understand and analyze flow patterns.

Flow visualization using tufts has been a valuable technique extensively employed in aerodynamic research to provide insights into the complex flow behavior around airfoil surfaces. This method offers a qualitative understanding of airflow patterns and separation phenomena, which is often challenging to capture through numerical simulations alone.

Previous literature highlights the significance of smoke and tuft flow visualization in elucidating airfoil aerodynamics. Tuft flow visualization has proven to be an indispensable tool in aerodynamic research, offering a visual representation of complex flow phenomena and enhancing our understanding of airfoil behavior.

### **4.6.1 Smoke flow visualization**

At low wind speeds, the behaviour of leading-edge protuberances was investigated using a smoke flow visualisation technique for baseline and modified SG6043 airfoils. Figures 4.28 to 4.31 depict the observed flow patterns. The flow pattern and vortices produced by the straight leading edge, as shown in the figures in Figure 4.28 (a) were used as a reference. As shown in Figure 4.28 (b), a separation bubble formed for the baseline at  $15^\circ$ . The flow reattached after the mid-chord position, and the separation point was close to the leading edge.

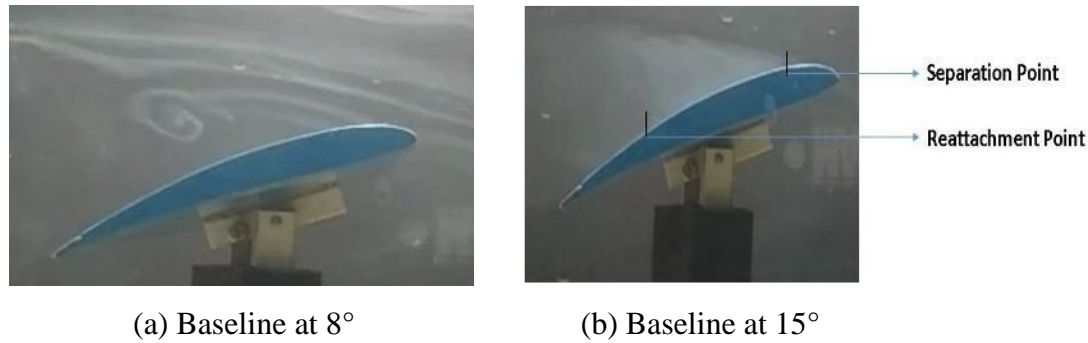
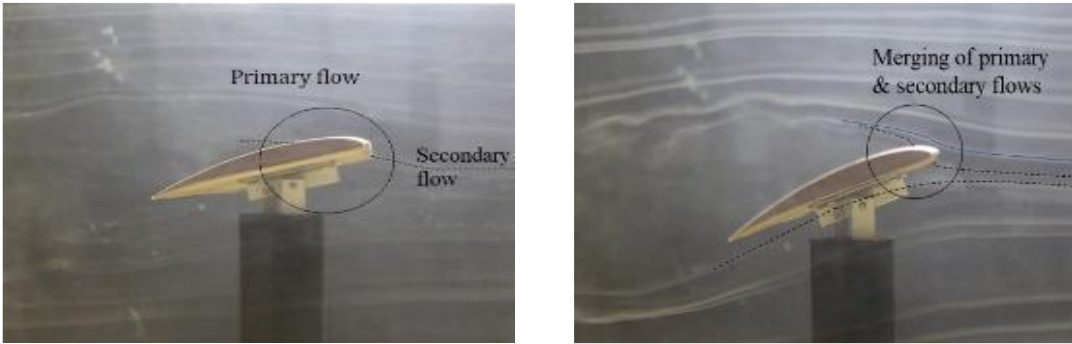


Figure 4.28: Experimental flow patterns observed using the smoke flow visualization for the SG6043 baseline.

Previous research ((Miklosovic *et al.* 2004), (Hansen *et al.* 2011), (Fletcher, 1975), (Van Nierop *et al.* 2008), (Johari *et al.* 2007)) has shown that the tubercle effect is caused by the generation of streamwise vortices, which energise the boundary layer. Because only one smoke stream was introduced into the flow in this study, we could only look at streamwise flow patterns. For sinusoidal and triangular models, a distinct flow feature was observed at greater angles.

As shown in Figure 4.29(a), secondary flow emerged from trough regions. The secondary flow merged with the primary flow as the angle of attack increased, as shown in Figure 4.29(b). This phenomenon energised the flow at greater angles, yielding higher poststall lift values in experiments. Despite the fact that the sinusoidal and triangular profiles produced similar flow behaviour, there was a difference in secondary flow volume and strength. The sharp triangular edges effectively guide the flow to the trough regions, resulting in a large volume of secondary flow.

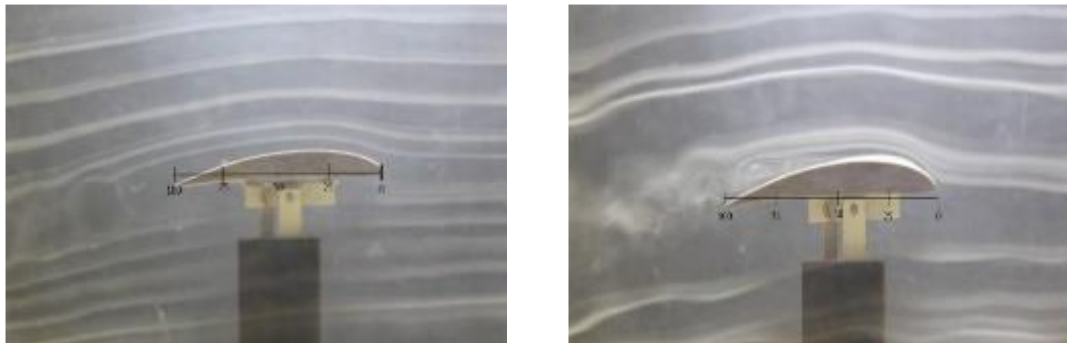
Furthermore, the reduced flow attached to the pressure side of the airfoil reduced skin friction drag. As a result, triangular protuberances are better suited for the SG6043 airfoil in terms of drag reduction due to off-design penalties at Reynolds number of 100K and poststall lift improvement. More flow research is needed to determine the behaviour of streamwise vortices and better understand the stall delay phenomenon. Figure 4.30 depicts the flow patterns obtained for the slotted model at an angle of attack of 0°.



(a)

(b)

Figure 4.29: (a) Secondary flow emerging from the trough region at  $10^\circ$  and (b) Merging of primary and secondary flows at  $15^\circ$  for SG6043 A9W64.5 Triangular model.

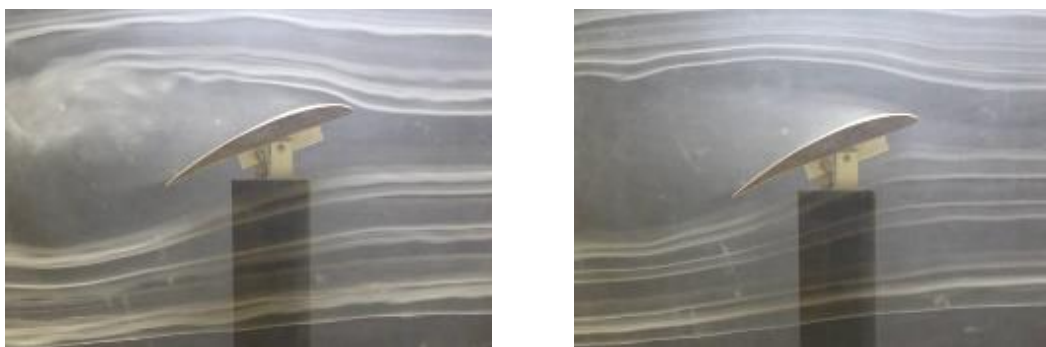


(a)

(b)

Figure 4.30: Streamline patterns of SG6043 A9W64.5 Slotted model with angle of attack  $0^\circ$  (a) At non-slot region and (b) At slot region.

The flow behaviour differed between slotted and straight leading-edge regions. The streamline followed the airfoil contour shape until 60% of the chord in the straight leading-edge region, as shown in Figure 4.31(a). The flow separated at the slotted region at precisely 50% of the chord, resulting in vortices, as shown in Figure 4.31(b).



(a)

(b)

Figure 4.31: (a) Leading edge separation and (b) Formation of recirculation region behind the leading edge observed at angle of attack  $15^\circ$ .

After passing through the trailing edge, these vortices continued for a short distance. When compared to the baseline, the slotted model had a slight increase in the lift value at zero angle. This result is attributed to additional streamwise vortices generated by leading-edge slots, which contribute to the flow's overall vorticity. Vortex flow theory can explain the additional lift. Figure 4.31(b) shows the flow patterns obtained for the slotted model at higher angles. At  $15^\circ$  angle, flow phenomena such as leading edge separation, formation of recirculation regions at the leading edge, and wake regions were observed.

#### **4.6.2 Tuft flow visualization**

Tuft flow visualization on the E216 airfoil provides a comprehensive insight into its aerodynamic behavior across different flow regimes. At various key points in the airflow, such as  $0^\circ$  angle of attack, pre-stall, stall, and post-stall conditions, tuft patterns offer valuable information about the airflow's characteristics and separation phenomena.

Starting at  $0^\circ$  angle of attack, tufts on the airfoil's surface exhibit a smooth and aligned pattern, indicating attached flow shown in Figure 4.32(a). As the angle of attack increases beyond this point, the tufts begin to display subtle deviations from alignment, suggesting the initiation of boundary layer separation. At pre-stall conditions, the tufts may become slightly disordered, indicating the onset of flow separation on the airfoil's upper surface. This visualization helps in identifying the regions where airflow detachment starts to occur shown in Figure 4.32(b). As the angle of attack progresses further into stall conditions, the tufts become more chaotic and disorganized. This signifies the occurrence of dynamic stall, a complex phenomenon characterized by intermittent flow separation and reattachment over the airfoil's surface shown in Figure 4.32(c). Flow separation occurs uniformly at 20% of the chord length from the leading edge in the baseline model. This position represents the maximum lift coefficient and stall occurrence.

#### 4.6.2.1 Baseline

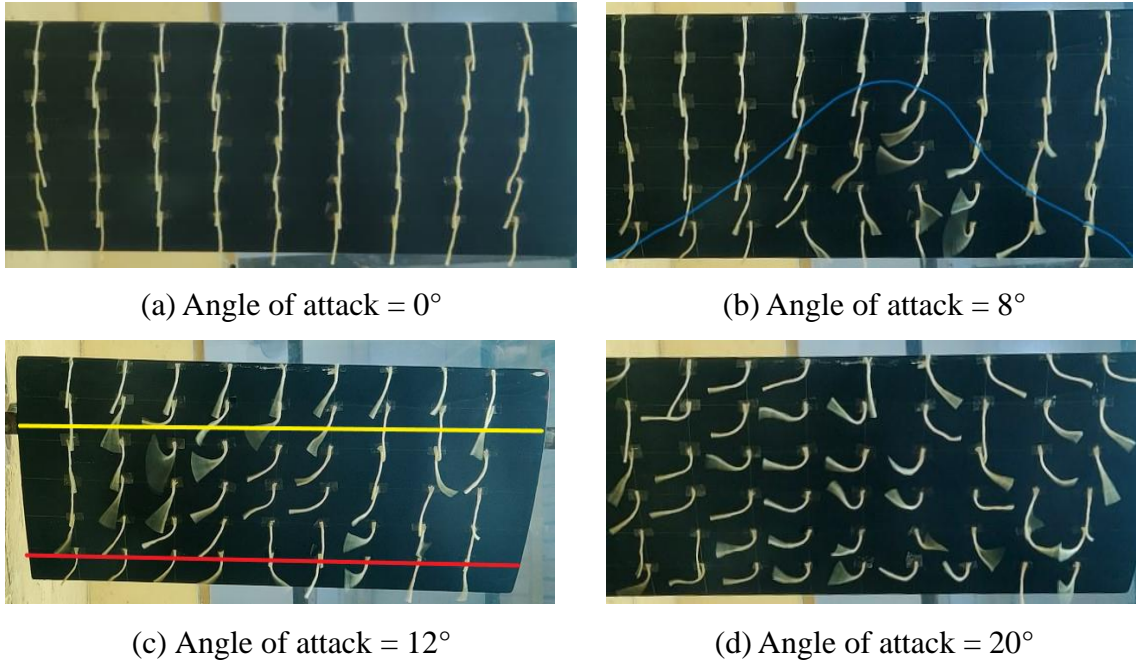


Figure 4.32: Visualisation of tuft patterns on a baseline airfoil at various angles of attack

Tufts located on the upper surface may fluctuate rapidly and even intermittently detach and reattach, indicating the turbulent and unsteady airflow patterns during stall. This behavior aligns with the expected behavior during dynamic stall, where vortex shedding and flow separation become prominent. Figure 4.32(d) highlights the tufts moving away completely in the post stall region at angle of attack  $20^\circ$ .

In the post-stall region, the tuft patterns begin to stabilize, suggesting the reattachment of airflow to the airfoil's surface as the angle of attack decreases. However, the tufts may continue to exhibit slight variations and oscillations, highlighting the transient nature of the post-stall flow regime.

#### 4.6.2.2 Sinusoidal Protuberances

Tuft flow visualization on the sinusoidal protuberance airfoil shown in Figure 4.33, highlighting the flow separation and reattachment in stall and post stall regions.

Starting at  $0^\circ$  angle of attack, the tufts on the airfoil's surface exhibit a relatively uniform and aligned pattern, indicating attached flow shown in Figure 4.33(a). As the angle of attack increases and approaches pre-stall conditions, the tufts begin to show subtle deviations from alignment, indicating the initiation of boundary layer separation, particularly around the

protuberances shown in Figure 4.33(b). Moving into the pre-stall phase, the tuft patterns on the sinusoidal protuberance airfoil become more disordered and erratic compared to the baseline. This suggests that the presence of the protuberances alters the airflow dynamics, potentially delaying separation and altering flow patterns around the protuberances. This effect becomes more pronounced as the angle of attack continues to increase.

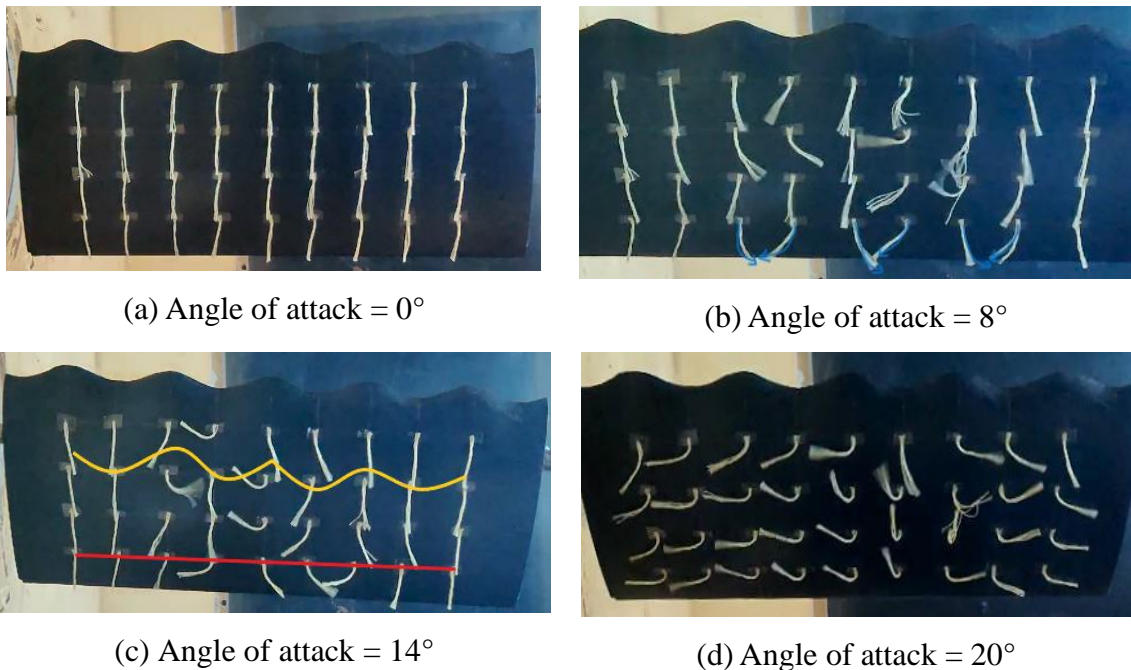


Figure 4.33: Visualisation of tuft patterns on a sinusoidal airfoil at various angles of attack

During stall conditions, the tufts may exhibit a more complex behavior on the airfoil's surface, indicating the presence of dynamic stall. The tufts near the protuberances experience intermittent separation and reattachment, indicative of the unsteady airflow characteristics. Notably, the tuft patterns over the protuberances shows variations in response to the oscillating flow, secondary flow through these wave patterns promotes attached flow over the surface, causing the separation line to shift towards the trailing edge shown in Figure 4.33(c). In the sinusoidal protuberance model, this phenomenon contributes to increased lift and delays stall. Flow separation occurs at about 22% of the chord length from the leading edge for the sinusoidal model. In the post-stall region, as the angle of attack reaches 20°, the tufts exhibit complete detachment from the airfoil surface indicating full flow separation as shown in Figure 4.33(d).

### 4.6.2.3 Triangular Protuberances

Tuft flow visualization on the triangular protuberance airfoil at different angles of attack shown in Figure 4.34. At the initial angle of attack  $0^\circ$  shown in Figure 4.34(a), the tuft patterns on the triangular protuberance model airfoil exhibit a relatively uniform and aligned arrangement, indicating attached flow. As the angle of attack gradually increases, at angle of attack  $8^\circ$ , the tuft patterns start to show slight deviations from alignment, suggesting the beginning of boundary layer changes shown in Figure 4.34(b).

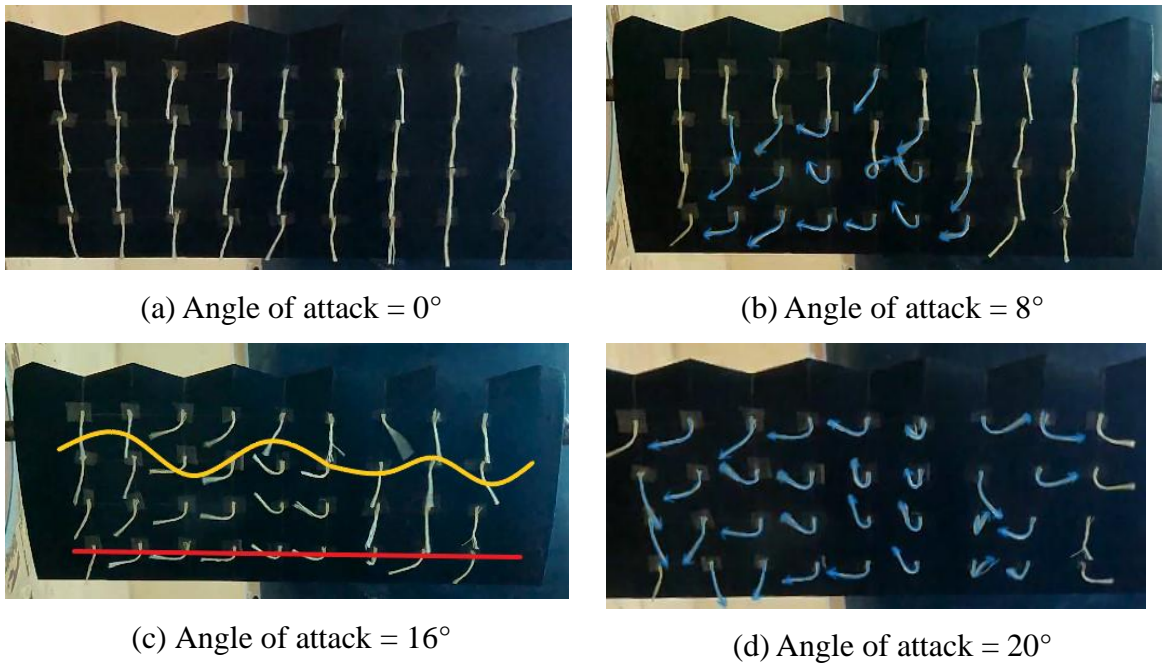


Figure 4.34: Visualisation of tuft patterns on a triangular airfoil at various angles of attack

Approaching pre-stall conditions, the tufts on the airfoil's surface display more noticeable deviations from alignment, signifying the initiation of boundary layer separation. Notably, the presence of triangular protuberances alters the flow dynamics, potentially delaying the onset of flow separation around the protuberances. Transitioning into the pre-stall phase, the tuft patterns on the triangular protuberance airfoil exhibit a more complex and disturbed appearance compared to the baseline airfoil. This alteration in tuft behavior indicates that the triangular protuberances influence airflow around them, possibly delaying separation and affecting the flow patterns.

During the stall phase, at angle of attack  $16^\circ$ , the tufts demonstrate intricate and dynamic behavior, particularly near the triangular protuberances. The tufts shown in Figure 4.34(c), experience intermittent separation and reattachment, indicative of the unsteady and complex

flow phenomena associated with dynamic stall. Flow separation occurs at about 24% of the chord length from the leading edge for the triangular model. This behavior provides visual cues about how the triangular protuberances influence the stall characteristics of the airfoil. As the angle of attack approaches  $20^\circ$ , the tuft patterns on the airfoil surface shown in Figure 4.34(d), completely shifted and highlights full flow separation.

#### 4.6.2.4 Slot Protuberances

Tuft flow visualization on the slot protuberance airfoil illustrates improved aerodynamic performance compared to baseline. At the initial angle of attack ( $0^\circ$ ), tufts display relatively uniform patterns, highlights attached flow as shown in figure 4.35(a). As the angle of attack increases, tuft alignments remain coherent, indicating favorable boundary layer behavior. In the pre-stall phase, tuft patterns exhibit stability around the slot protuberances, indicating effective flow control shown in Figure 4.35(b). During stall, tufts show organized patterns near the protuberances, suggesting delayed flow separation. Flow separation occurs at about 24% of the chord length from the leading edge for the slot model shown in Figure 4.35(c). At  $20^\circ$ , the tuft patterns on the airfoil surface shown in Figure 4.35(d) completely shifted and highlights full flow separation. In the post-stall phase, tuft reattachment patterns near the protuberances suggest efficient aerodynamic recovery.

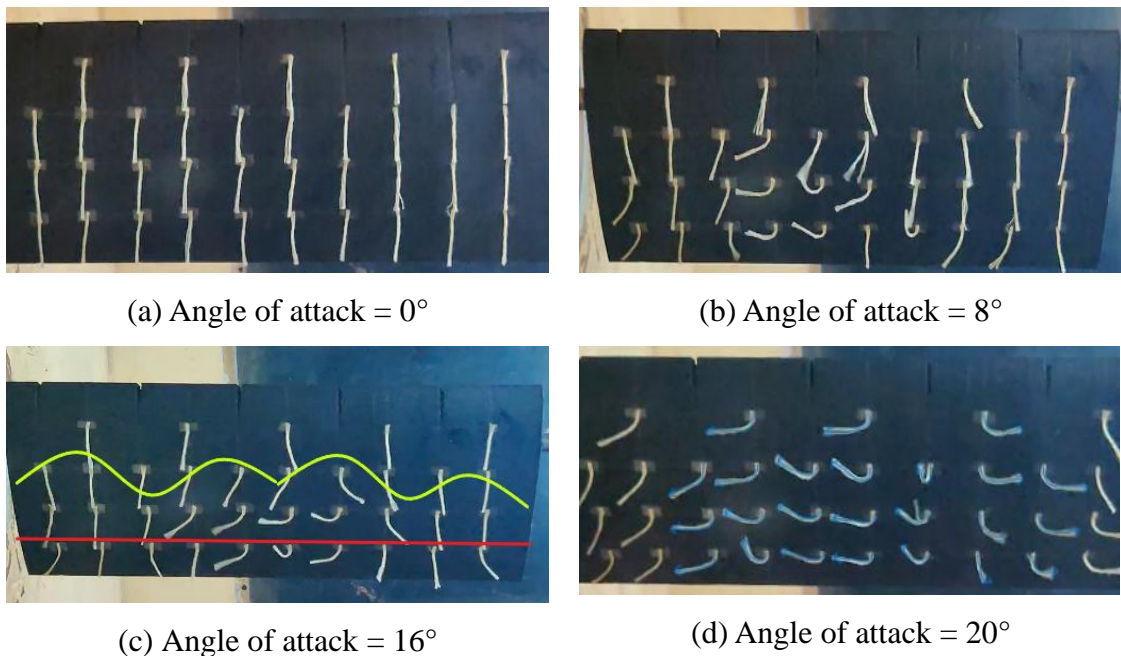


Figure 4.35: Visualisation of tuft patterns on a slot airfoil at various angles of attack

Overall, tuft visualization underscores the positive impact of slot protuberances on flow control and enhanced aerodynamic performance. Tuft flow visualization highlights varied aerodynamic effects among different protuberance models. Sinusoidal patterns indicate early stalls and disruption. Notably, slot and triangular protuberance models displayed more attached flow through the troughs resulting in increased lift coefficients with stall delay.

## 4.7 CONCLUSIONS

The static study concluded that leading-edge protuberances (sinusoidal, triangular, and slot-shaped) significantly improved the aerodynamic performance of SG6043 and E216 airfoils at Reynolds number 100K. Sinusoidal and triangular protuberances delayed stall by  $2^\circ$  to  $4^\circ$ , enhancing lift and lift-to-drag ratios, with triangular and slot shapes showing the most promise for stall delay and post-stall performance. Optimal performance was observed with low amplitude and high wavelength configurations. Slot protuberances exhibited the best  $C_{lmax}$ , stall delay, and post-stall characteristics due to strong vortex formation and pressure distribution. The E216 airfoil benefited more from these modifications compared to the SG6043, highlighting the impact of protuberance geometry on enhancing aerodynamic properties.

The Reynolds number study found that at 100K and 150K, Reynolds numbers slot, triangular, and sinusoidal protuberances significantly improved aerodynamic performance, with  $C_{lmax}$  increases of 29%, 23%, and 13%, respectively, compared to the baseline at 150K Reynolds number. Slot and triangular protuberances particularly enhanced post-stall lift and provided smoother post-stall behavior, making them more effective than sinusoidal protuberances.

The dynamic study revealed that adding protuberances to the airfoil not only altered lift coefficient patterns but also affected hysteresis loop size during dynamic stall. Furthermore, protuberance models exhibited smoother post-stall behavior compared to the baseline. Overall, slot and triangular protuberances notably enhanced  $C_{lmax}$  compared to both the baseline and sinusoidal protuberance models.

the flow control mechanisms behind leading-edge protuberances for E216 and SG6043 airfoils are studied further. The investigation utilizes numerical methods, including turbulent kinetic energy (TKE) analysis and pressure contours, alongside smoke flow visualization techniques. Specifically, tuft flow visualization is applied to the E216 airfoil for dynamic studies, aimed at observing the generation of counter-rotating vortices, as well as flow

separation and reattachment over the airfoil surface. The study reveals that the flow control mechanism demonstrates consistent effects across both static and dynamic scenarios, particularly in the generation of counter-rotating vortices.



## CHAPTER- 5

### EFFECT OF LEADING EDGE PROTUBERANCES ON THE PERFORMANCE OF SHAWT

In continuation of the previous study, wind turbine experiments were conducted to evaluate the aerodynamic efficiency of both baseline and protuberance blades of E216 cross section. Sinusoidal, triangular, and slotted blade configurations were experimentally tested and compared to the baseline results.

#### 5.1 SIZE OF THE WIND TURBINE

The design process for wind turbines begins by determining the desired power output required for its intended application. Knowledge about the average wind speed is then employed to calculate the turbine diameter (D) using the power equation 5.1 (Tummala *et al.* 2016). This equation establishes a relationship between the power output of the turbine and its corresponding diameter, forming a crucial aspect of the turbine design procedure.

$$P = \eta \frac{1}{2} \rho A_s V_\infty^3 \quad (5.1)$$

Where,  $\eta$  represents the overall efficiency of the turbine and  $A_s$  is the swept area of the turbine.

$$A_s = \frac{\pi}{4} D^2 \quad (5.2)$$

where D denotes the diameter of the turbine. Literature suggests that the overall efficiency falls within the range of 20-25% for SHAWT.

#### 5.2 DESIGN OF WIND TURBINE BLADE

The blade design incorporates BEMT, relying on fundamental blade geometry parameters: chord length (c), twist ( $\theta_T$ ), and pitch angle ( $\beta$ ). The design of the rotor blade accounts for wake rotations, utilizing empirical relations governing the relative angle ( $\phi$ ) and chord variation at each segment of the blade. These relations are represented by equations (5.3), (5.4), (5.5), (5.6), (5.7), and (5.8) (Manwell *et al.* 2010), providing essential guidelines for the blade's optimal form concerning rotational wake effects and variations in chord length at distinct blade segments.

$$\phi = \frac{2}{3} \tan^{-1}\left(\frac{1}{\lambda_r}\right) \quad (5.3)$$

Where,  $\lambda_r = \lambda\left(\frac{r}{R}\right)$

The axial and tangential induction factors are given by the equations,

$$c = \frac{8\pi r}{BC_l} \left[ \frac{2}{3} \tan^{-1}\left(\frac{1}{\lambda_r}\right) \right] \quad (5.4)$$

The twist angle ( $\theta_T$ ), pitch angle at any specific section ( $\theta_P$ ), and the pitch angle at the tip ( $\theta_{P,0}$ ) are determined using the following equations:

$$a = \frac{1}{\left[ 1 + \frac{4 \sin^2 \phi}{\sigma_r C_l \cos \phi} \right]} \quad (5.5)$$

$$a^t = \frac{1-3a}{[4a-1]} \quad (5.6)$$

$$\theta_T = \theta_P - \theta_{P,0} \quad (5.7)$$

$$\phi = \theta_P + \alpha_{design} \quad (5.8)$$

Where,  $\alpha_{design}$  is the design angle of attack.

### 5.2.1 Blade shape

To determine the twist and chord distributions shaping the blade, the entire blade was divided into N segments. The twist and chord for each segment were calculated using BEMT (Manwell *et al.* 2010). The input parameters are provided in Table 5.1 for wind turbine rotor design.

Table 5.1. Rotor design input parameters through BEMT

Airfoil	Design tip speed ratio( $\lambda$ )	Rotor radius (m)	No. of blades	No. of elements	Rated Velocity (m/s)
E216	2.5	0.325	3	10	10

The torque and speed sensors provide the torque and angular values during experiments. Further, with this information, it becomes feasible to calculate the power coefficient using equation 5.9.

$$C_p = \frac{P_{rotor}}{P_{wind}} = \frac{B\tau_{blade}\omega}{0.5\rho AV_{rated}^3} \quad (5.9)$$

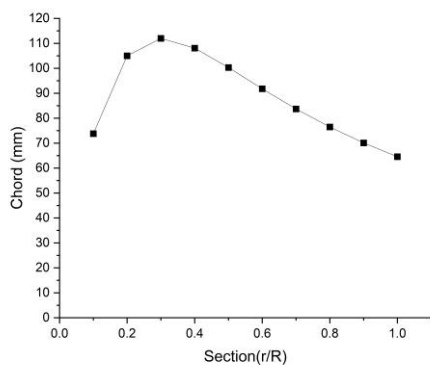
where,

$B$  = No. of blades,  $\omega$  = Angular speed of rotor (rad/s),  $V_\infty$  = free stream velocity (m/s),  
 $\tau_{blade}$  = Blade torque (N-m).

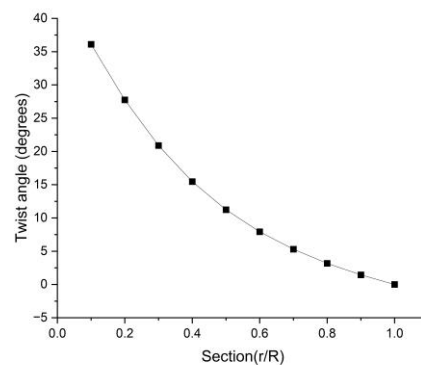
The blade design using BEMT is tabulated in Table 5.2 and plotted in Figure 5.1:

Table 5.2. Determination of chord length and twist angle using BEMT

Section	Section radius (m)	$\lambda_r$	Angle of Relative Wind	Section pitch angle ( $\theta_p$ )	Twist angle ( $\theta_T$ )	Chord (m)
1	0.0325	0.25	50.642	44.642	36.108	0.073
2	0.065	0.5	42.289	36.289	27.755	0.104
3	0.0975	0.75	35.420	29.420	20.885	0.111
4	0.13	1	30	24	15.465	0.108
5	0.1625	1.25	25.773	19.773	11.238	0.100
6	0.195	1.5	22.460	16.460	7.925	0.091
7	0.2275	1.75	19.829	13.829	5.295	0.083
8	0.26	2	17.710	11.710	3.175	0.076
9	0.2925	2.25	15.974	9.974	1.440	0.070
10	0.325	2.5	14.534	8.534	0	0.064



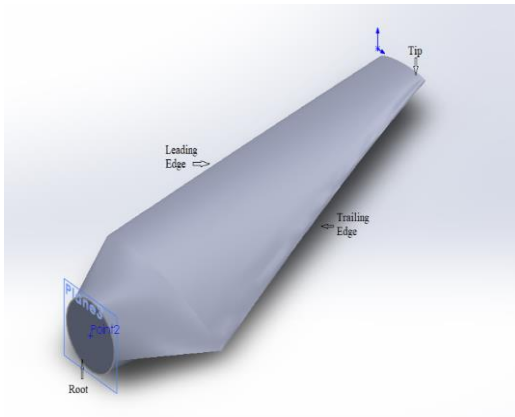
(a) Chord



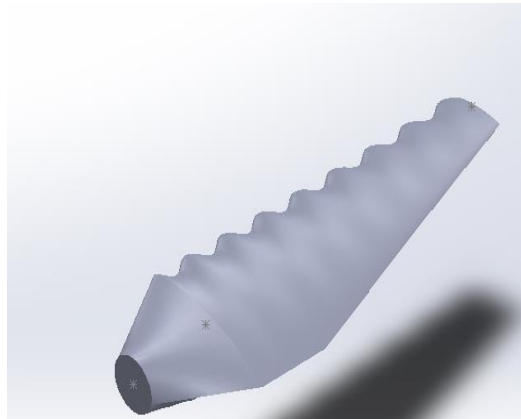
(b) Twist angle

Figure 5.1: Section radius vs Chord and twist angle

## 5.2.2 Geometry modelling



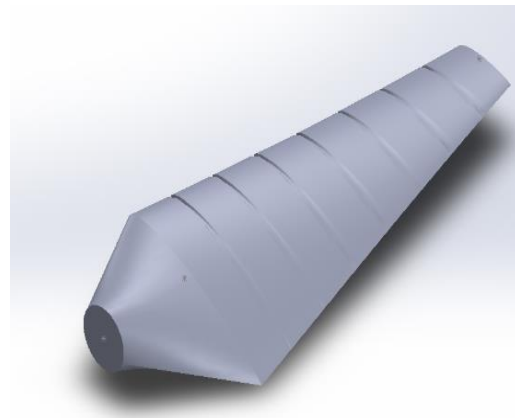
(a) Baseline blade



(b) Sinusoidal blade



(c) Triangular blade



(d) Slot blade

Figure 5.2: Wind turbine blade design models: baseline and protuberance variants

The current study utilizes the E216 airfoil as the cross-sectional geometry for both the baseline and protuberance models. SOLIDWORKS software is employed to generate the blade based on chord and twist distribution given in Table 5.2. The baseline turbine has a blade span of 0.255m and a rotor diameter of 0.65m. The average chord length of the blade measures 0.1m. The chord of the airfoil varies at each section in accordance with the taper. Additionally, the twist angle is specified at each section based on the designated design values. Like the baseline blades, the protuberance blades are designed by modifying the leading edge of the blade, incorporating sinusoidal, triangular, and slot shapes shown in Figure 5.2. Additionally, it's ensured that the designed protuberance models maintain a surface waviness upto 40% from the leading edge, facilitating the existence of secondary flow on the blade surface.

### 5.2.3 Fabrication of wind turbine blades



(a) Baseline blades



(b) Sinusoidal protuberance blades



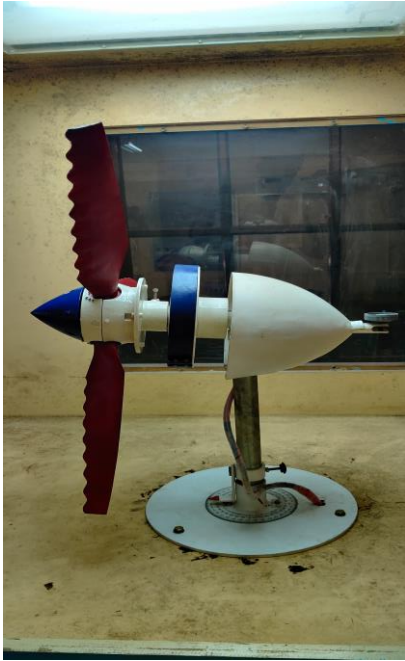
(c) Triangular protuberance blades



(d) Slot protuberance blades

Figure 5.3 Experimental models for SHAWT aerodynamic performance testing

Wind turbine blades were designed for a test section velocity of 10m/s and a Reynolds number of 100K. The models chosen for experimentation are baseline and leading-edge protuberances with A9W64.5, which has been previously identified as optimal in aerodynamic performance in previous chapter. The wind turbine blades are 3D printed with poly lactic acid material, shown in Figure 5.3. The manufactured blades are then connected to the turbine rotor, and the wind turbine unit is finally mounted in the subsonic wind tunnel facility shown in 5.4(a)(b).



(a) Wind turbine side view



(b) Wind turbine front view

Figure 5.4: Installation of wind turbine within the test section

#### 5.2.4 Wind Tunnel facility along with turbine testing unit

Experiments are carried out at the subsonic wind tunnel facility shown in Figure 5.5. The wind turbine aerodynamic analysis involves the utilization of various instruments and components. Key instruments employed in the experiment include an anemometer, generator, torque sensor, and speed sensor. The torque sensor, equipped with a linear Hall effect, and the speed sensor, featuring a digital pulse output, provide crucial data necessary for analyzing the wind turbine's performance within the wind tunnel. A parameter display unit is employed to monitor the wind turbine parameters throughout the experimentation process shown in Figure 5.6.

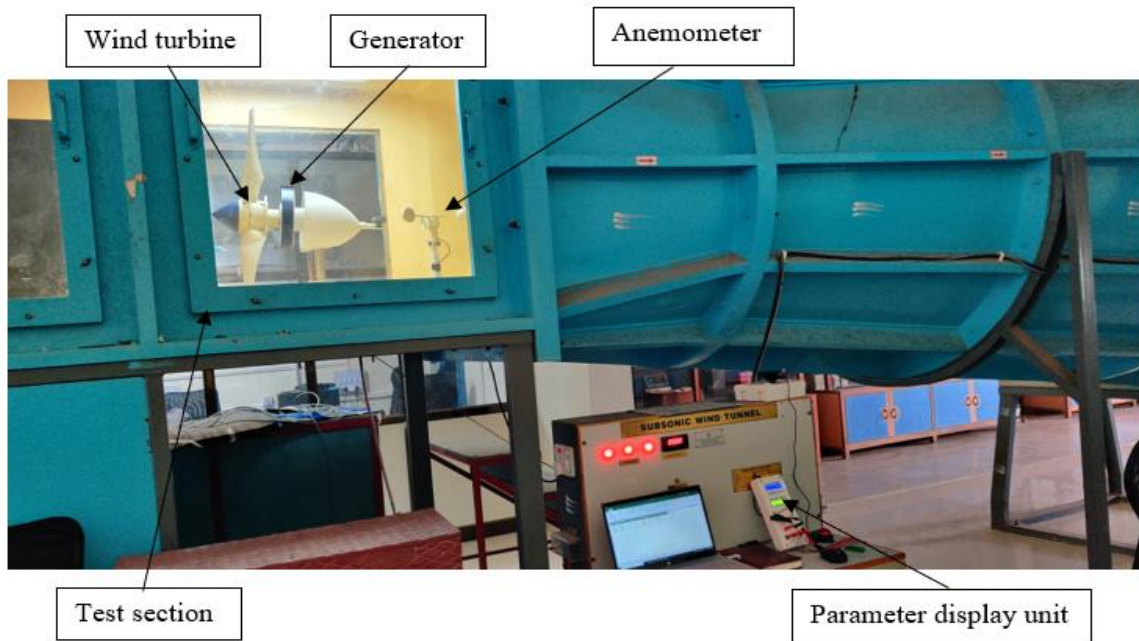


Figure 5.5: Subsonic wind tunnel facility along with wind turbine test setup



Figure 5.6: Wind turbine parameter display unit

The parameter display unit is integrated with an anemometer, torque sensor, generator, and speed sensor, allowing for comprehensive continuous monitoring. This unit displays multiple parameters at the same time, such as the generator's voltage and current outputs, the anemometer's wind velocity readings, and the torque sensor data. The technical specifications

for the parameter display unit are detailed in Table 5.3. Detailed technical specifications of generator are tabulated in Table 5.4.

Table 5.3 Technical specification of the parameter display unit

<b>Parameter</b>	<b>Range</b>
RPM sensing range	0-999
V <sub>Dc</sub>	0-24
A <sub>Dc</sub>	0-15
Torque	0-99 N/m

Table 5.4 Technical specifications of generator unit

<b>Parameter</b>	<b>Type / range</b>
Rotor Diameter	210 mm
Generator voltage	12V / 24V
Generator wattage	300 Watt
Generator type	Axial Flux PMG
Number of poles	16
Type of magnet	Neodymium N35
Stator	Magnetic copper
Number of phases	3 + 1 Neutral
Maximum wattage	360 W
Maximum voltage	30 V
Maximum current	12 A

## 5.3 RESULTS AND DISCUSSION

The power coefficient ( $C_P$ ) measures the performance of wind turbines. The  $C_P$  is defined as the power extracted by the wind turbine divided by the energy available in the wind stream. The  $C_P$  of a wind turbine varies with operational conditions such as wind speed, pitch angle, turbine rotation speed, and tip speed ratio.

### 5.3.1 Baseline wind turbine

Figure 5.7 illustrates the impact of velocity on the  $C_P$  of the baseline wind turbine across various tip speed ratios.

Initially, the  $C_P$  value rises as the tip speed ratio increases, peaking at  $\lambda=3$ . Subsequently, there is a sudden decline in  $C_P$  until  $\lambda=3.5$ , followed by a gradual decrease beyond that point. Throughout the study, it was noted that the highest  $C_P$  value recorded was 0.36, achieved at a tip speed ratio of 3 and a wind speed of 10m/s. Similar trends were observed across other wind velocities.

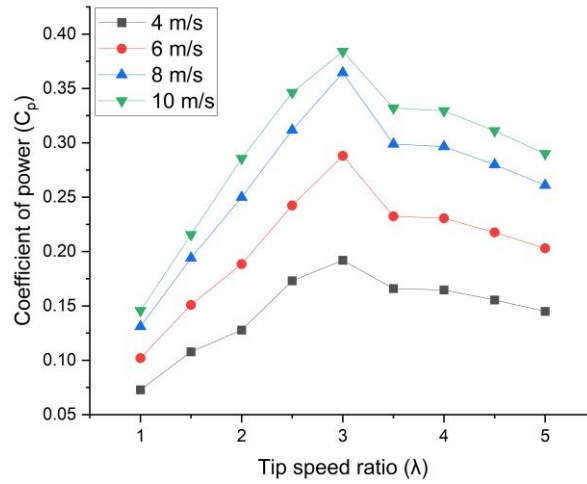


Figure 5.7: Validation of  $C_P$  with TSR for baseline wind turbine

### 5.3.2 Wind turbine with sinusoidal protuberance blades

Figure 5.8 depicts how the  $C_P$  varies for wind turbine with sinusoidal leading edge protuberance blades with tip speed ratio.

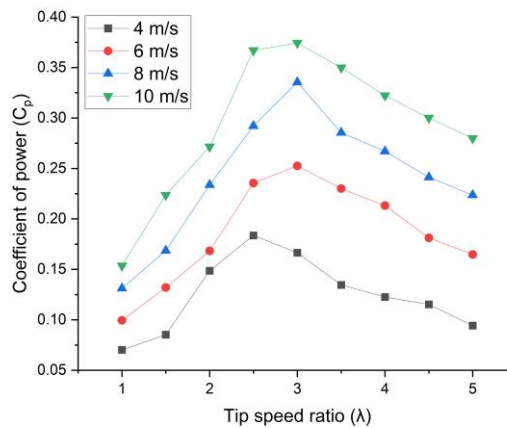


Figure 5.8: Variation of  $C_P$  with TSR for wind turbine with sinusoidal protuberance blades

Initially, the  $C_P$  value ascends with increasing tip speed ratio until it reaches 3. After this threshold, the  $C_P$  value gradually declines with further increase in tip speed ratio. Throughout the experiment, the highest  $C_P$  value recorded was 0.37, observed at a tip speed ratio of 2.93 and a wind speed of 10m/s. In comparison to the baseline wind turbine, the  $C_P$  increased slightly in the wind turbine equipped with sinusoidal protuberance blades.

### 5.3.3 Wind turbine with triangular protuberance blades

The study found that as the tip speed ratio increases, the  $C_P$  initially increases. This suggests that there is an optimal range of tip speed ratios at which the turbine runs more efficiently and extracts more power from the wind. The maximum  $C_P$  is observed at a tip speed ratio of 2.8. However, beyond the optimal tip speed ratio of 2.8, the  $C_P$  begins to decrease.

This implies that operating the turbine at higher tip speed ratios yields diminishing returns in terms of power extraction efficiency. The study reports that the highest observed  $C_P$  during the experiment was 0.38. The maximum value was achieved at a tip speed ratio of 2.8 and a wind speed of 10 m/s shown in Figure 5.9.

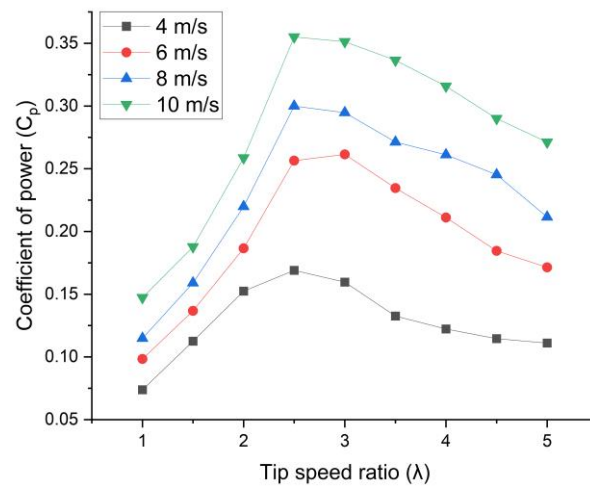


Figure 5.9: Variation of  $C_P$  with TSR for wind turbine with triangular protuberance blades

Overall, these findings indicate that using a triangular leading edge tubercle can improve wind turbine performance, especially when operating within the optimal tip speed ratio range.

### 5.3.4 Wind turbine with slot protuberance blades:

The study highlights how adding a slotted leading edge protuberances can improve wind turbine performance by maximizing the  $C_P$  within a specific range of tip speed ratios shown in Figure 5.10. Results show  $C_P$  increases with tip speed ratio until reaching 3, peaking at 0.39 ( $\lambda=2.97$ , 10 m/s). However, exceeding this optimal range lowers  $C_P$ , indicating decreased efficiency. Understanding this relationship is crucial for optimizing wind turbine performance.

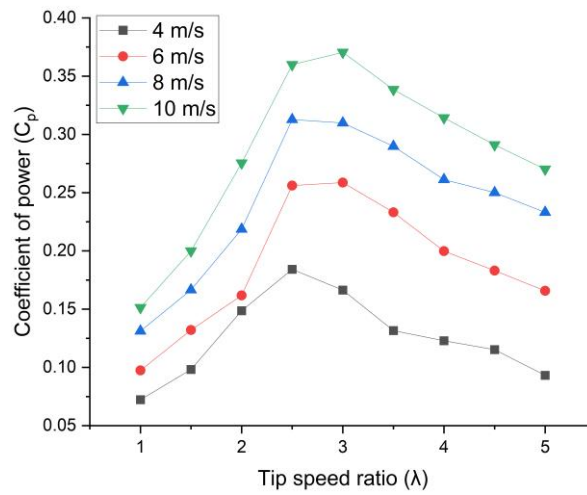


Figure 5.10: Variation of  $C_P$  with TSR for wind turbine with slot protuberance blades

## 5.4 PROTUBERANCES EFFECT ON COEFFICIENT OF PERFORMANCE

The aerodynamic performance of wind turbines at a velocity 10m/s with various protuberance blade models, such as sinusoidal, triangular, and slot designs, was tested and compared with the baseline, as shown in Figure 5.11. The wind turbines, equipped with different protuberance blades such as sinusoidal, triangular, and slotted blades, demonstrate enhancements in  $C_P$  by 2.7%, 5.2%, and 7.6%, respectively, when compared to the baseline blades.

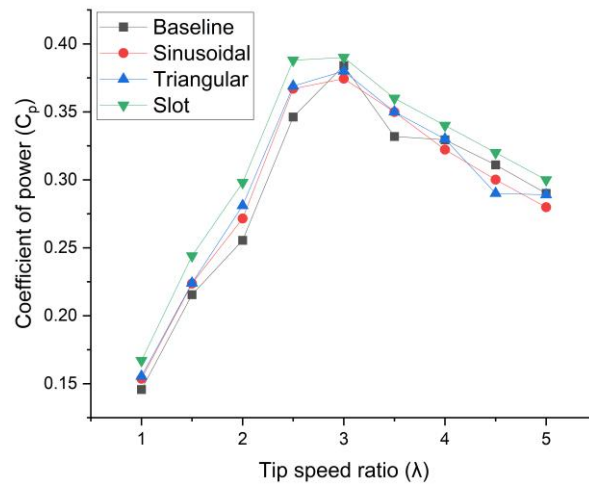


Figure 5.11: Comparison of  $C_P$  vs TSR for different turbines at a velocity 10m/s

According to the findings, the slot protuberances blade model exhibited the highest  $C_P$  value among the three shapes. This indicates that wind turbines equipped with slot protuberances achieved improved aerodynamic efficiency compared to those with sinusoidal and triangular protuberances.

## 5.5 CONCLUSIONS

Wind turbines with protuberance blades, including sinusoidal, triangular, and slotted designs, show  $C_P$  enhancements of 2.7%, 5.2%, and 7.6%, respectively, compared to baseline blades. Testing reveals that slot, triangular, and slot protuberances notably boost  $C_P$ , indicating enhanced aerodynamic efficiency in SHAWT.

## CHAPTER 6

### CONCLUSIONS AND SCOPE FOR FUTURE WORK

#### 6.1 CONCLUSIONS

The study assessed how sinusoidal, triangular, and slot-shaped leading-edge protuberances impacted SG6043 and E216 airfoils at Reynolds number 100K through a blend of experimental and numerical analysis. Sinusoidal protuberances delayed stall by  $2^\circ$  with the smallest amplitudes, enhancing E216 A4.5W64.5  $C_{lmax}$  by 2.88% and  $(L/D)_{max}$  by 6.22%. The E216's  $C_{lmax}$  and  $(L/D)_{max}$  increased with wavelength at a fixed amplitude but decreased with amplitude at a constant wavelength.

Triangular protuberances delayed stall by  $2^\circ$  to  $4^\circ$  for E216 A4.5 and A9 models. The lowest amplitudes improved  $C_{lmax}$  and  $(L/D)_{max}$ , rising with wavelength at a consistent amplitude while decreasing with amplitude at a steady wavelength. The E216 A4.5W64.5 achieved an 11.2% increase in  $C_{lmax}$  and a 14.43% rise in  $(L/D)_{max}$  at stall angle.

Slot protuberances delayed stall by  $2^\circ$  to  $4^\circ$  across configurations. The E216 showed enhanced  $C_{lmax}$  and stall delay, boosting  $(L/D)_{max}$  for configurations with the lowest amplitude. The SG6043 exhibited only improved  $C_{lmax}$  with low amplitudes, although a decrease in  $(L/D)_{max}$  was observed.

Among them, A4.5 slot and triangular protuberances excelled in stalling and post-stall performance, respectively, delaying stall initiation, enhancing stall  $C_l$ , and delivering smoother post-stall lift. Optimal performance favored low amplitude and high wavelength.

Detailed analysis of static pressure distributions unveiled significant differences among protuberance types, with slots demonstrating superior  $C_{lmax}$ , stall delay, and post-stall performance. The static pressure displayed similar trends for sinusoidal, triangular, and baseline models, while slots indicated marginally higher pressure differences. The smallest  $C_p$  plot in sinusoidal configuration led to  $C_l$  degradation. Conversely, slots exhibited superior  $C_{lmax}$ , stall delay, and post-stall performance due to robust vortex strength and pressure distribution. These variations in pressure distributions, influenced by protuberance shape,

directly impacted the generation and behavior of counter-rotating vortices, thereby affecting the overall aerodynamic performance.

Additionally, visualization studies using smoke visualization techniques illustrated unique flow features, highlighting increased secondary flow volumes at higher angles, contributing to elevated post-stall lift values. Such visualization confirmed distinct flow behaviors for sinusoidal and triangular protuberances, indicating different secondary flow volume and strength. The tuft flow visualization revealed that flow separation occurred at varying distances from the leading edge in protuberance models, at approximately 22% for the sinusoidal model and 24% for the triangular and slot configurations. Notably, both the slot and triangular protuberance models demonstrated enhanced attached flow through the troughs, resulting in higher lift coefficients and stall delay.

In summary, each protuberance model showcased specific aerodynamic characteristics, presenting a mix of advantages and limitations when compared to the baseline airfoil. Triangular and slot protuberances emerged as promising designs, exhibiting favorable stall delay and improved  $C_{lmax}$ . These findings underline the pivotal role of protuberance design in augmenting aerodynamic performance, emphasizing the necessity of considering protuberance geometry for enhancing lift and stall characteristics across various operational conditions.

In the baseline configuration, the SG6043 airfoil has a higher stall angle and  $C_{lmax}$  than the E216 airfoil. However, leading-edge protuberances provided more advantages to the E216 airfoil than to the SG6043 airfoil.

The study examining the Reynolds number effect on protuberances found negligible impact on aerodynamic performance at very low Reynolds numbers. However, at 100K and 150K Reynolds numbers, notable improvements emerged: enhanced post-stall lift coefficients alongside stall delay compared to the baseline. Specifically, slot, triangular, and sinusoidal protuberances showcased significant increases in  $C_{lmax}$  by 29%, 23%, and 13%, respectively, compared to the baseline configuration at 150K Reynolds number.

The introduction of protuberances to the airfoil not only affects the lift coefficient patterns but also influences the hysteresis loop size during dynamic stall. Additionally, the protuberance models offer smooth post stall behavior when compared with baseline. Overall, the study

found that slot and triangular protuberances significantly improved  $C_{lmax}$  when compared with baseline and sinusoidal protuberance models.

The wind turbines, equipped with different protuberance blades such as sinusoidal, triangular, and slotted blades, demonstrate enhancements in  $C_P$  by 2.7%, 5.2%, and 7.6%, respectively, when compared to the baseline blades. Based on the turbine testing outcomes, slot, triangular and slot protuberances significantly increased the  $C_P$ , demonstrating improved aerodynamic efficiency in SHAWT.

Overall, this study's comprehensive insights into protuberance induced aerodynamic alterations offer valuable contributions to airfoil design strategies, urging careful consideration of protuberance geometry's role in optimizing aerodynamic performance in SHAWT.

## **6.2 SCOPE FOR FUTURE WORK**

The current investigation concentrates on assessing the impact of three protuberance shapes - sinusoidal, triangular, and slot - within a specific range of amplitude and wavelength at low Reynolds numbers. Future research could expand the scope to include other shapes such as circular, semicircular, and beyond. Additionally, implementing particle image velocimetry studies would enable an experimental exploration of the flow mechanisms associated with these protuberances.

Furthermore, there is a need to delve into structural considerations, specifically focusing on stress concentration and potential fracture failures in the protuberance blades. To comprehensively adopt protuberances into wind turbine blades, it is essential to conduct acoustic and vibration studies as well.



## REFERENCES

- Ahmad, M., and Zafar, M. H. (2023). “Enhancing vertical axis wind turbine efficiency through leading edge tubercles: A multifaceted analysis.” *Ocean Eng.*, 288(P1), 116026.
- Ahmed Farouk Abdel Gawad. (2013). “Utilization of Whale-Inspired Tubercles as a Control .” *Tsest*, Vol. 2, 212–218.
- Alkhabbaz, A., Yang, H. S., Weerakoon, A. H. S., and Lee, Y. H. (2021). “A novel linearization approach of chord and twist angle distribution for 10 kW horizontal axis wind turbine.” *Renew. Energy*, 178, 1398–1420.
- Broeren, A. P., and Bragg, M. B. (2001). “Spanwise variation in the unsteady stalling flowfields of two-dimensional airfoil models.” *39th Aerosp. Sci. Meet. Exhib.*, (January).
- Carr et al. (1977). “Analysis of the development of dynamic stall based on oscillating airfoil experiments.” NASA TN D-.
- Carr, L. W. (1988). “Dynamic stall progress in analysis and prediction.” 25(1).
- Carr, L. W., Mcalister, K. W., and Ames, N. (1983). “The Effect of a Leading-Edge Slat on the Dynamic Stall of an Oscillating Airfoil AIAA Aircraft Design , Systems and Technology Meeting.” *New York*.
- Corsini, A., Delibra, G., and Sheard, A. G. (2013). “On the role of leading-edge bumps in the control of stall onset in axial fan blades.” *J. Fluids Eng. Trans. ASME*, 135(8), 1–9.
- Dearing, S., Lambert, S., and Morrison, J. (2007). “Flow control with active dimples.” *Aeronaut. J.*, 111(1125), 705–714.
- Drela, M., and Youngren, H. (2001). “XFOIL 6.94 user guide.”
- Esmaeili, A., Delgado, H. E. C., and Sousa, J. M. M. (2018). “Numerical simulations of low-Reynolds-Number flow past finite wings with leading-Edge protuberances.” *J. Aircr.*, 55(1), 226–238.
- Fan, M., Dong, X., Li, Z., Sun, Z., and Feng, L. (2022). “Numerical and experimental study on flow separation control of airfoils with various leading-edge tubercles.” *Ocean Eng.*, 252(June 2021), 111046.

- Fish, F. E., and Lauder, G. V. (2006). "Passive and active flow control by swimming fishes and mammals." *Annu. Rev. Fluid Mech.*, 38, 193–224.
- Fish, F. E., Weber, P. W., Murray, M. M., and Howle, L. E. (2011). "The tubercles on humpback whales' flippers: Application of bio-inspired technology." *Integr. Comp. Biol.*, 51(1), 203–213.
- Fletcher. (1975). "Mechanics of flight." *Phys. Educ.*, 10(5), 385.
- FLUENT. (2014). "Theory Guide." 15.
- Francis and Keesee. (1985). "Airfoil dynamic stall performance with large-amplitude motions." *AIAA J.*, 23(11), 1653-1659.
- Godard, G., and Stanislas, M. (2006). "Control of a decelerating boundary layer. Part 1: Optimization of passive vortex generators." *Aerosp. Sci. Technol.*, 10(3), 181–191.
- Ham, N. D., and Garelick, M. S. (2009). "Dynamic Stall Considerations in Helicopter Rotors." *J. Am. Helicopter Soc.*, 13(2), 49–55.
- Hansen, K. L., Kelso, R. M., and Dally, B. B. (2011). "Performance variations of leading-edge tubercles for distinct airfoil profiles." *AIAA J.*, 49(1), 185–194.
- Holst, D., Balduzzi, F., Bianchini, A., Nayeri, C. N., Paschereit, C. O., and Ferrara, G. (2019a). "Static and dynamic analysis of a NACA 0021 airfoil section at low Reynolds numbers: Drag and moment coefficients." *Proc. ASME Turbo Expo*, 9, 1–12.
- Holst, D., Church, B., Pechlivanoglou, G., Tüzüner, E., Saverin, J., Nayeri, C. N., and Paschereit, C. O. (2019b). "Experimental analysis of a NACA 0021 airfoil section through 180-deg angle of attack at low Reynolds numbers for use in wind turbine analysis." *J. Eng. Gas Turbines Power*, 141(4), 1–12.
- Horton, H. P. (1968). "Laminar separation bubbles in two and three dimensional incompressible flow." 452.
- Huang, G. Y., Shiah, Y. C., Bai, C. J., and Chong, W. T. (2015). "Experimental study of the protuberance effect on the blade performance of a small horizontal axis wind turbine." *J. Wind Eng. Ind. Aerodyn.*
- Jahanmiri, M. (2011). "Laminar Separation Bubble : Its Structure , Dynamics and Control."

*Res. Rep.*, (2011:06), 1–24.

Jewel B. Barlow, William H. RAE Jr., A. P., and Hrynuik, J. T. (2015). “Low Speed Wind Tunnel Testing.” 7(1), 31–39.

Johari, H., Henoch, C., Custodio, D., and Levshin, A. (2007). “Effects of leading-edge protuberances on airfoil performance.” *AIAA J.*, 45(11), 2634–2642.

Kline, S. J. (1963). “Describing uncertainties in single-sample experiments.” *Mech. Eng.*, 75, 3–8.

Leishman, J. G. (1990). “Dynamic stall experiments on the NACA 23012 aerofoil.” *Exp. Fluids*, 9(1–2), 49–58.

Miklosovic, D. S., Murray, M. M., and Howle, L. E. (2007). “Experimental evaluation of sinusoidal leading edges.” *J. Aircr.*, 44(4), 1404–1408.

Miklosovic, D. S., Murray, M. M., Howle, L. E., and Fish, F. E. (2004). “Leading-edge tubercles delay stall on humpback whale (*Megaptera novaeangliae*) flippers.” *Phys. Fluids*, 16(5).

Ministry of Power. (2022). “Monthly Renewable Energy Generation Report Date November 2022.” *Gov. India*, 162(5), 1–31.

Moghaddam, T., and Neishabouri, N. B. (2017). “On the Active and Passive Flow Separation Control Techniques over Airfoils.” *IOP Conf. Ser. Mater. Sci. Eng.*, 248(1).

Monterey, C. M. S. C. hand rase khara N. P. S. (1993). “Interferometric investigations of compressible dynamic stall over a transiently pitching airfoil.”

Mueller, T. J. (1999). “Defense Technical Information Center Compilation Part Notice Numbers for Fixed Wing Micro-Air Vehicles Aerodynamic Measurements at Low Reynolds Numbers for Fixed Wing Micro-Air Vehicles.” 1–8.

Mueller, T. J., and Batill, S. M. (1980). “Experimental Studies of the Laminar Separation Bubble on a Two-Dimensional Airfoil At Low Reynolds Numbers.” *AIAA Pap.*, 20(4), 457–463.

Musial, W. D., and Cromack, D. E. (1988). “Influence of reynolds number on performance modeling of horizontal axis wind rotors.” *J. Sol. Energy Eng. Trans. ASME*, 110(2), 139–144.

- Ng, B. F., New, T. H., and Palacios, R. (2017). "Bio-inspired leading-edge tubercles to improve fatigue life in horizontal axis wind turbine blades." *35th Wind Energy Symp. 2017*, (January), 1–11.
- Nierop, E. A. Van, Alben, S., and Brenner, M. P. (2008). "How bumps on whale flippers delay stall: An aerodynamic model." *Phys. Rev. Lett.*
- Nosenchuck et al. (1995). "Spatial and temporal characteristics of boundary layers controlled with the Lorentz force." *12th Australas. Fluid Mech. Conf.*, 93–96.
- Ozen, C. A., and Rockwell, D. (2010). "Control of vortical structures on a flapping wing via a sinusoidal leading-edge." *Phys. Fluids*, 22(2), 1–3.
- Patankar, S. V. (2018). "Numerical heat transfer and fluid flow." *CRC Press*.
- Paula, A. A. de, Padilha, B. R. M., Mattos, B. da S., and Meneghini, J. R. (2016). "The airfoil thickness effect on wavy leading edge performance." *54th AIAA Aerosp. Sci. Meet.*, 0(January), 1–43.
- Pechlivanoglou, G. (2012). "Passive and active flow control solutions for wind turbine blades." *PhD thesis*.
- Pedro, H. T. C., and Kobayashi, M. H. (2008). "Numerical study of stall delay on humpback whale flippers." *46th AIAA Aerosp. Sci. Meet. Exhib.*, (January), 7–10.
- Polhamus, E. C. (1968). *Application of the leading-edge-suction analogy of vortex lift to the drag due to lift of sharp-edge delta wings*.
- Ramesh et al. (2009). "Development of Smart Actuators for Active Flow Control." (Ldv), 38–40.
- Rodriguez, J., and Rothan, D. (1993). "Low reynolds number laminar separation bubble control using a backward facing step." *SAE Tech. Pap.*, 102, 1892–1900.
- ROGERS, J. F. M. | J. G. M. | A. L., and WIND. (2010). *Wind energy explained: theory, design and application*. John Wiley Sons.
- Roskam, J., & Lan, C. T. E. (1997). *Airplane aerodynamics and performance*.
- Sayed, M. A., Kandil, H. A., and Shaltot, A. (2012). "Aerodynamic analysis of different

wind-turbine-blade profiles using finite-volume method.” *Energy Convers. Manag.*, 64, 541–550.

Schlichting, H., & Gersten, K. (2016). *Boundary-layer theory*.

Selig, M. S., and McGranahan, B. D. (2004). “Wind tunnel aerodynamic tests of six airfoils for use on small wind turbines.” *J. Sol. Energy Eng. Trans. ASME*, 126(4), 986–1001.

Shih, C., Lourenco, L., Dommelen, L. Van, and Krothapall, A. (1992). “Unsteady flow past an airfoil pitching at a constant rate.” *AIAA J.*, 30(5), 1153–1161.

Siram, O., Sahoo, N., and Saha, U. K. (2022). “Wind Tunnel Tests of a Model Small-Scale Horizontal-Axis Wind Turbine Developed From Blade Element Momentum Theory.” *J. Energy Resour. Technol. Trans. ASME*, 144(6), 1–10.

Stanway, M. J. (2008). “Hydrodynamic effects of leading-edge tubercles on control surfaces and in flapping foil propulsion.” *Master Sci. Ocean Eng.*, 101.

Tiainen, J., Grönman, A., Jaatinen-Värri, A., & Backman, J. (2017). Flow control methods and their applicability in low-Reynolds-number centrifugal compressors—a review. *International Journal of Turbomachinery, Propulsion and Power*, 3(1), 2.

Tummala, A., Velamati, R. K., Sinha, D. K., Indraja, V., and Krishna, V. H. (2016). “A review on small scale wind turbines.” *Renew. Sustain. Energy Rev.*, 56, 1351–1371.

Walker. (1991). “The role of laminar-turbulent transition in gas turbine engines.” *J. Turbomach.*, 113(4), 509–536.

Watts, P., and Fish, F. E. (2001). “The influence of passive, leading edge tubercles on wing performance.” *Proc. Twelfth Intl. Symp. Unmanned Untethered Submers. Technol., Durham New Hampsh.*, (May), 2–9.

Weber, P. W., Howle, L. E., & Murray, M. M. (2010). “Lift, drag, and cavitation onset on rudders with leading-edge tubercles.” *Mar. Technol. SNAME News*, 47(01), 27–36.

Weber, P. W., Howle, L. E., Murray, M. M., and Miklosovic, D. S. (2011). “Computational evaluation of the performance of lifting surfaces with leading-edge protuberances.” *J. Aircr.*, 48(2), 591–600.

Wei, B., Gao, Y., and Li, D. (2021). “Physics of Dynamic Stall Vortex During Pitching

Oscillation of Dynamic Airfoil.” *Int. J. Aeronaut. Sp. Sci.*, 22(6), 1263–1277.

Wei, B., Gao, Y., Wang, L., and Li, D. (2019). “Analysis of flow transition and separation on oscillating airfoil by pressure signature.” *J. Mech. Sci. Technol.*, 33(1), 279–288.

Winslow, J., Otsuka, H., Govindarajan, B., and Chopra, I. (2018). “Basic understanding of airfoil characteristics at low Reynolds numbers (104–105).” *J. Aircr.*, 55(3), 1050–1061.

Zhang, Y., Zhao, M., and Zhang, M. (2023). “Research on the aerodynamic performance of the wind turbine blades with leading-edge protuberances.” *Ocean Eng.*, 280(January), 114615.

Zhao, M., Wei, T., Zhao, Y., and Liu, Z. (2023). “Influences of Leading-Edge Tubercle Amplitude on Airfoil Flow Field.” *J. Therm. Sci.*, 32(4), 1335–1344.

Zhu, C., Yang, H., Qiu, Y., Zhou, G., Wang, L., Feng, Y., Shen, Z., Shen, X., Feng, X., and Wang, T. (2023). “Effects of the Reynolds number and reduced frequency on the aerodynamic performance and dynamic stall behaviors of a vertical axis wind turbine.” *Energy Convers. Manag.*, 293(July), 117513.

## LIST OF PUBLICATIONS

### Journals

1. **Jayapal Reddy, C.**, & Sathyabhama, A. (2022). “Comparative Study on the Effect of Leading Edge Protuberance of Different Shapes on the Aerodynamic Performance of Two Distinct Airfoils.” *Journal of Applied Fluid Mechanics*, 16(1), 157-177. Doi: 10.47176/JAFM.16.01.1334

### Conferences

1. **Jayapal Reddy C** and Sathyabhama A, “Numerical and experimental investigation of aerodynamic performance of two distinct airfoils with leading edge triangular protuberances”, Proceedings of the 25th National and 3rd International ISHMT-ASTFE Heat and Mass Transfer Conference (IHMTTC-2019), December 28-31, 2019, IIT Roorkee, Roorkee, India.
2. **Jayapal Reddy C**, Sathyabhama A and Raghavendra S, “Lift Enhancement of an airfoil using Leading edge Triangular Protuberances for Small Scale Wind Turbine Blades”, Proceedings of the 24th National and 2nd International ISHMT-ASTFE, Heat and Mass Transfer Conference (IHMTTC-2017), December 27-30, 2017, BITS Pilani, Hyderabad, India.



## APPENDIX A

### Experimental procedure and calibration for strain gauge Force measurement system:

#### Calibration of strain gauge force measurement system:

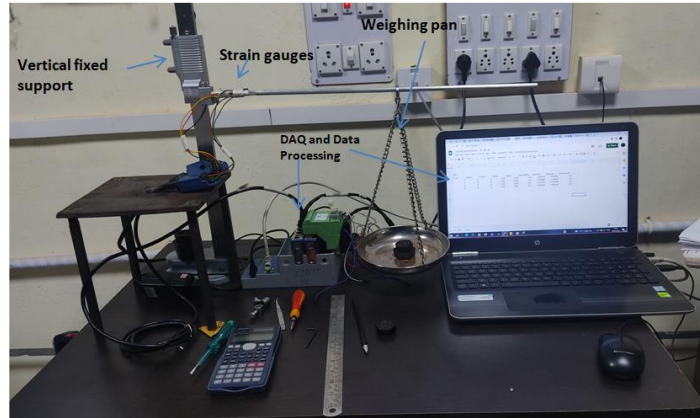


Figure 1: Calibration setup for strain gauge load measurement

The study focuses on validating force measurements using strain gauges mounted on a force measurement shaft fixed at one end and free at the other as shown in Figure 1. Initially, strain gauge readings were adjusted to zero in the absence of any load. Known loads were then applied at specified distances from the strain gauges to validate both experimental strains and theoretical calculations for lift and drag forces. The strain gauges are mounted on the shaft with a rectangular cross-section having dimensions  $h=6\text{mm}$  and  $b=6\text{mm}$ . The distance (l) from the respective strain gauges for applying loads for lift and drag is  $0.25\text{m}$  and  $0.285\text{m}$ , respectively.

$$e = \frac{\sigma}{E} \quad (1)$$

The observed strains in lift and drag measurements during the experiment revealed a maximum discrepancy of 6.4% and 1.2%, respectively, across distinct trials when contrasted with the theoretical value derived from Equation 1. Figure 2 depicted a comparative analysis demonstrating the relationship between theoretical and experimental values for lift and drag forces.

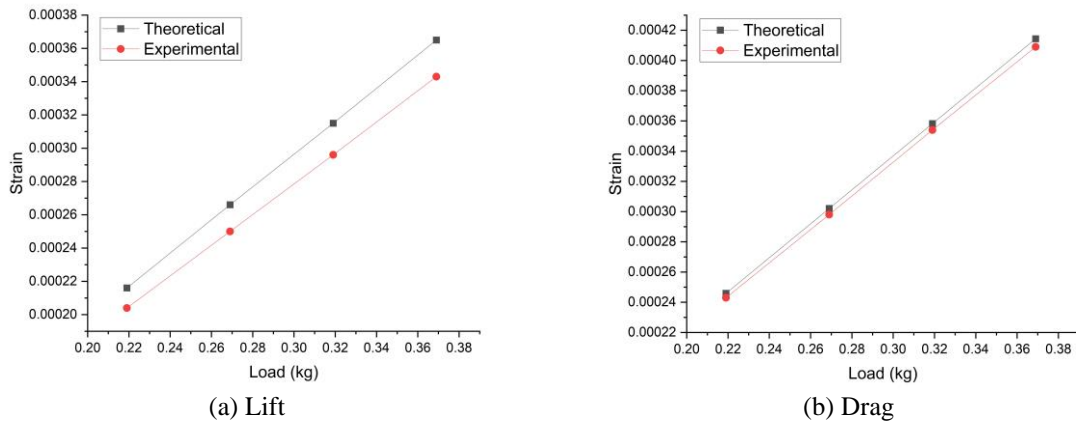


Figure 2: Strain measurement calibration

## Experimental procedure for strain gauge force measurement system:

### Static study:

In the static study case, data was gathered at two-degree intervals within the range of 0 to 20 degrees. Before data collection at each angle, a settling time of approximately 30 seconds was allowed for the airflow. The LABVIEW Program operates a stepper motor to achieve the desired angle relative to the current resting position. This is accomplished by sending a single pulse (comprising two samples - one high and one low) to the pulse channel until the specified angle is reached. The direction channel is provided with two samples (either both high or both low) based on the boolean direction input.

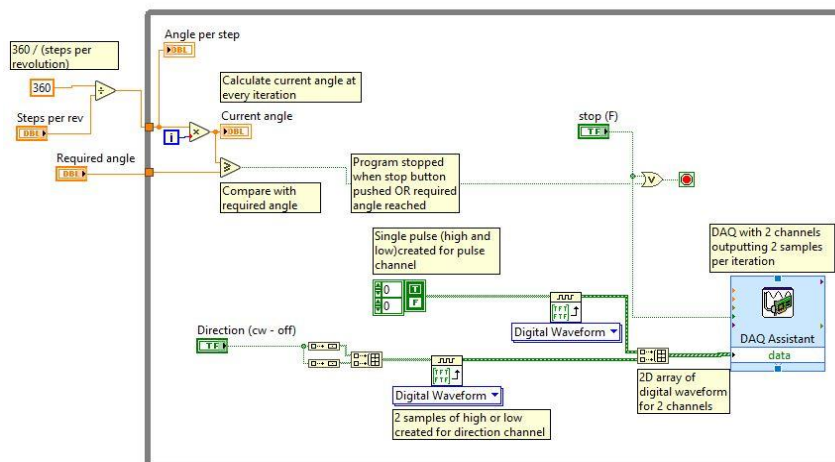
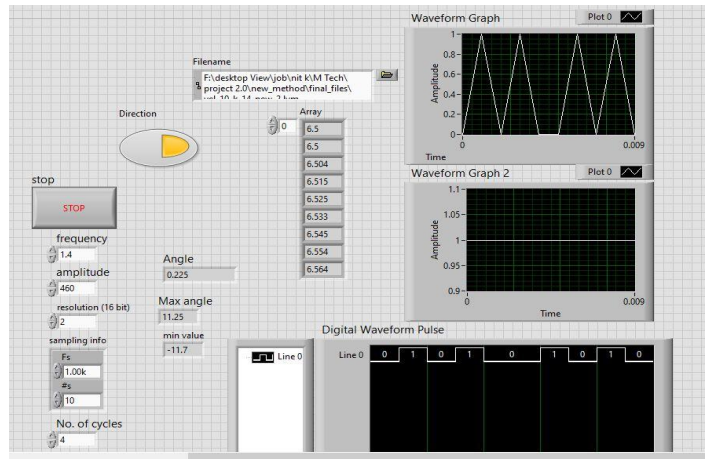


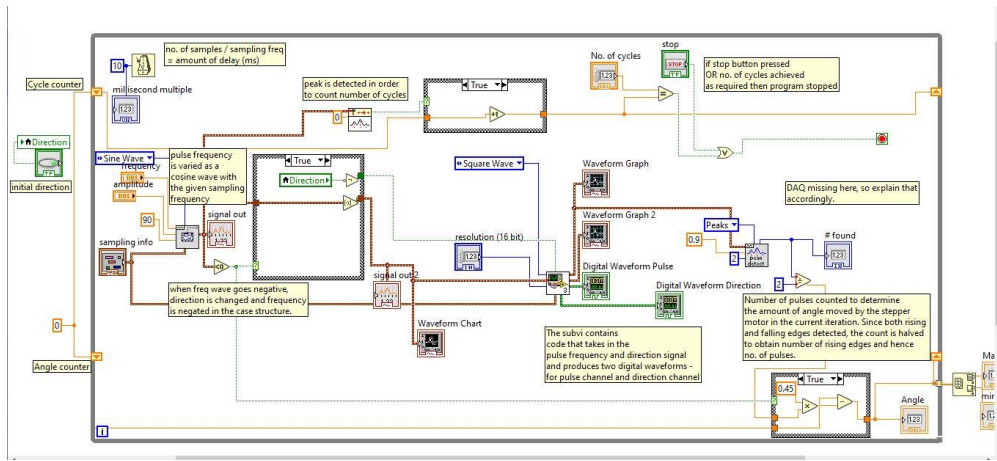
Figure 3: LabView block diagram for static case motor control.

The program depicted in Figure 3 controls a stepper motor to reach a specified angle in relation to the current resting position. This is accomplished by transmitting a single pulse (consisting of 2 samples - one high and one low) to the pulse channel until the desired angle is attained. Additionally, the direction channel is provided with 2 samples (either both high or both low) based on the boolean direction input.

**Dynamic study:**



(a)



(b)

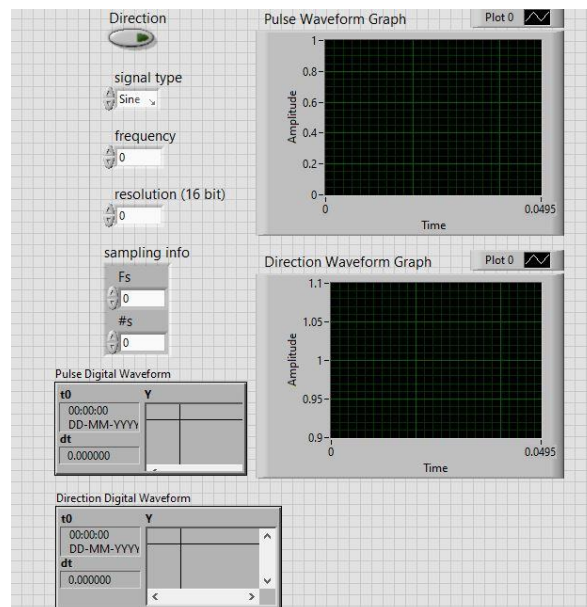
Figure 4: Motor control LabView program (a) Front panel, (b) Block diagram

In the dynamic study case, the airfoil underwent oscillation through direct control of the motor, owing to the direct coupling of the motor and shaft. At intervals of 0.01 seconds, a

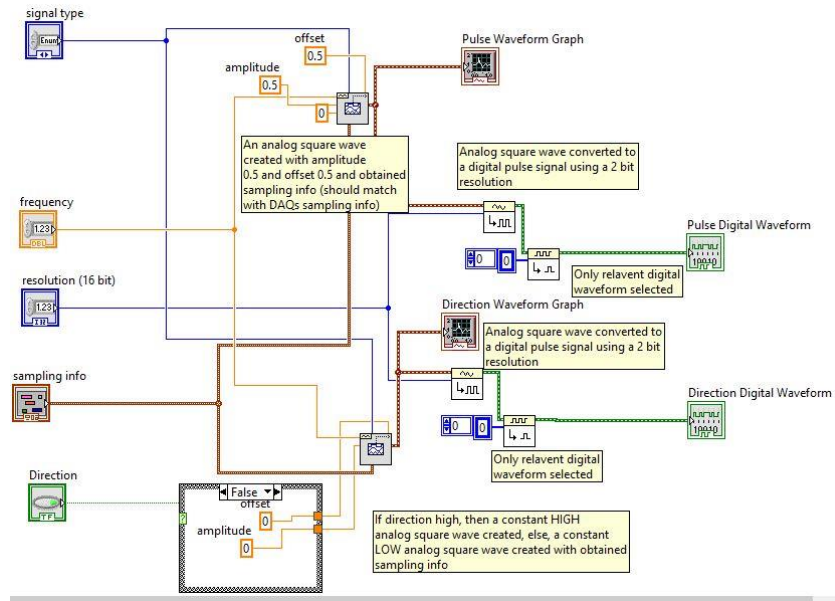
sinusoidal profile was fed to the motor controller and interpolated to achieve the required frequency for sinusoidal motion of the motor.

The LabView code generates a sinusoidal angular motion utilizing a stepper motor and a Rhino stepper driver. Given that the angular speed of a stepper driver is proportional to the pulse frequency, this frequency is modulated as a cosine wave to produce angular displacement represented as a sine wave. A customized LabView program was employed to manage the positioning, dynamic motion, and data collection from strain gauges. The objective of the program was to provide a unified user interface capable of concurrently handling the airfoil's position and collecting strain gauge data.

In Figures 4 and 5, the LabView code generates sinusoidal angular motion employing a stepper motor and Rhino stepper driver. The angular speed of the stepper driver is directly proportional to the pulse frequency. To achieve angular displacement represented as a sine wave, the pulse frequency is modulated in the code using a cosine wave. In Figure 6, the LabView code for logical strain gauge operations is illustrated.

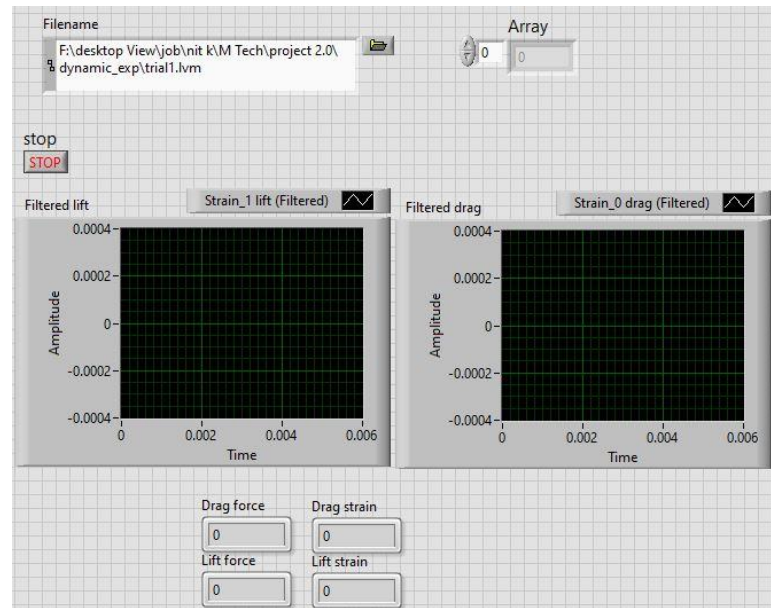


(a)

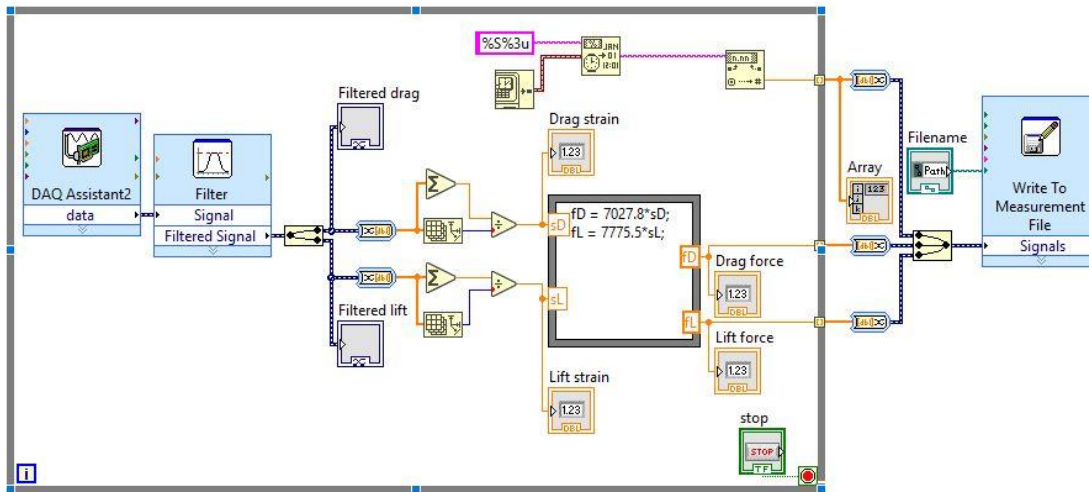


(b)

Figure 5: Motor control LabView Sub program (a) Front panel, (b) Block diagram



(a)



(b)

Figure 6: Strain gauges control LabView program (a) Front panel, (b) Block diagram

A custom program, developed using LabView software, was utilized to manage the positioning, dynamic motion, and acquisition of strain gauge data. The primary objective of the program was to create a unified user interface capable of concurrently handling both the airfoil's position and the collection of strain gauge data. Consequently, the program was designed to execute the following functions.

- Precisely control the airfoil's angular position, allowing adjustments in one-degree increments, with the option for finer adjustments at 0.225-degree increments.
- Display real-time strain and position data for prompt identification of system issues.
- Initiate the collection of static data with a single button click.
- Track data over a specified time duration.
- Choose a specific frequency for sinusoidal oscillations.
- Exercise control over the frequency and amplitude of oscillations.
- Maintain the axis in the same position during the transition between static and dynamic operation, allowing the user to define the mean angle of attack for oscillations.
- Start collecting dynamic data instantly with a button click.
- Simultaneously record both position and strain gauge data.

- Halt dynamic motion in case of a system failure.
- Provide user notifications for any system faults.
- Save the gathered information to a file.

The program was structured around a series of case structures accessible through a menu, ensuring a seamless transition between static and dynamic controls. Each structure comprised a high-priority loop and a low-priority loop.

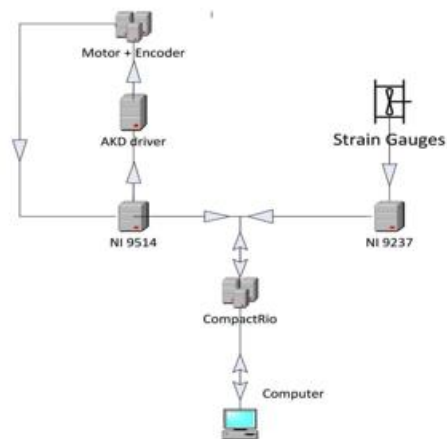


Figure 7: Experimental setup flow diagram

The high-priority loop was designed to oversee hardware functions such as motor control and strain data collection. To ensure timely completion of each task within the loop, synchronization with the Compact Rio was implemented through timing mechanisms. Acquired data, encompassing motor position, strain values from each half bridge, and timestamps, was stored in local variables. Subsequently, the low-priority loop utilized these variables to display and save the data to a file. The data flow block diagram is depicted in Figure 7.

### **Data Processing:**

The raw voltages obtained from the Wheatstone bridges underwent a conversion process to determine the equivalent lift and drag coefficients through data processing. Employing previously established calibration curves, the voltages recorded at each angle of attack were averaged over the data acquisition period and converted into their corresponding normal and tangential forces.

## Experimental Uncertainties:

The uncertainty is calculated using the following equations:

$$C_L = C_L(L, V) \quad (2)$$

$$\text{But, } L = L(\alpha, V_L) \text{ and } V = V(N, h) \quad (3)$$

$$\therefore C_L = C_L(\alpha, V_L, N, h) \quad (4)$$

$$\zeta_{C_L} = \sqrt{\left(\frac{\partial C_L}{\partial \alpha} \zeta_{\alpha}\right)^2 + \left(\frac{\partial C_L}{\partial V_L} \zeta_{V_L}\right)^2 + \left(\frac{\partial C_L}{\partial N} \zeta_N\right)^2 + \left(\frac{\partial C_L}{\partial h} \zeta_h\right)^2} \quad (5)$$

where, uncertainties of the independent variables are given in Table 1.

Table 1. Independent variables and their uncertainty values

Variable	Uncertainty
$\alpha$	$\pm 1.03\%$
$V_L$	$\pm 0.25\%$
N	$\pm 0.53\%$
h	$\pm 1.32\%$

# CURRICULUM VITAE

**JAYAPAL REDDY CHITTEPU**

**Email:** [jayapalreddychittepu@gmail.com](mailto:jayapalreddychittepu@gmail.com)

**Mobile:** +91-9963064019

---

---

## **Career Objective:**

To secure a challenging position in reputed organization, having Conducive Culture and giving scope for overall growth and enhancing my abilities and skills that helps me in contributing my best to the development of the organization as well as my personal growth.

## **Educational Qualifications:**

- **Ph. D.**, thesis entitled “Aerodynamic Performance of Leading Edge Protuberances at Low Reynolds Number” from **National Institute of Technology Karnataka**, registered in January 2017(**On going**).
- **M. Tech** in Advanced Internal Combustion Engines from **JNTUCE**, Anantapuramu with 86% of marks in the year 2013.
- **B. Tech** in Mechanical Engineering from **Intell Engineering College**, Anantapuramu with 72% of marks in the year 2011.
- **Diploma** in Mechanical Engineering from **Govt. polytechnic college**, Anantapuramu with 70% of marks in the year 2008.
- **SSC** from **ZPH School**, Putlur with 81% of marks in the year 2005.

## **Professional Experience: 10 Years**

- 1. Organization :** **Srinivasa Ramanujan Institute of Technology, Anantapuramu.**  
Designation : Assistant Professor  
Period : August 2020 to till date  
Role : Academic subjects handling (Heat transfer, thermodynamics), In-charge in administrative works like NBA & NAAC.
- 2. Organization :** **National Institute of Technology, Karnataka.**  
Designation : Senior Research Fellow  
Period : July 2018 to March 2020 (2 years)  
Funded by : DST-SERB  
Grant : 0.66 crore  
Role : Fabrication of models, Procurement of necessary instrumentation, Experimental investigation, and research report preparation.

- 3. Organization :** **National Institute of Technology, Karnataka.**  
 Designation : Junior Research Fellow  
 Period : July 2016 to June 2018 (2 years)  
 Funded by : DST-SERB  
 Grant : 0.66 crore  
 Role : Design of models, Numerical investigation, Experimental set up establishment and research report preparation.
- 4. Organization :** **Marri Laxman Reddy Institute of Technology & Management, Hyderabad.**  
 Designation : Assistant professor  
 Period : December 2015 to June 2016 (7 months)  
 Role : Academic subjects handling (Heat transfer, thermodynamics), In-charge in administrative works like NBA & NAAC.
- 5. Organization :** **Techzilon training solutions, Bangalore.**  
 Designation : Master Diploma Trainee  
 Period : June 2015 to August 2015 (3 months)  
 Role : Finding numerical solutions for flow problems using Computational Fluid Dynamics tool and also learning advanced techniques in CFD.
- 6. Organization :** **Gurunanak Institutions Technical campus, Hyderabad.**  
 Designation : Assistant professor  
 Period : January 2014 to June 2015 (1.5 years)  
 Role : Academic subjects handling (Heat transfer, thermodynamics & Fluid Mechanics and Hydraulic Machinery), Criteria 3&9 incharge in NBA work, Department Placement coordinator.

**Publications (International Journals/ International & national Conferences):**

1. **Jayapal Reddy C., & Sathyabhama, A.** (2022). “Comparative Study on the Effect of Leading Edge Protuberance of Different Shapes on the Aerodynamic Performance of Two Distinct Airfoils.” Journal of Applied Fluid Mechanics, 16(1), 157-177.
2. **Jayapal Reddy C, Sathyabhama A,** “Numerical and experimental investigation of aerodynamic performance of two distinct airfoils with leading edge triangular protuberances”, Proceedings of the 25th National and 3rd International ISHMT-ASTFE Heat and Mass Transfer Conference (IHMTTC-2019), December 28-31, 2019, IIT Roorkee, Roorkee, India.
3. Raghavendra S, Sathyabhama A, **Jayapal Reddy C,** “Effect of Leading Edge Slots on the Performance of Distinct Airfoil Profiles at Low Reynolds Numbers”, Asian Joint Workshop on Thermophysics and Fluid Science (AJWTF 7), Nov.21- 24, 2018, Trivandrum, India.

4. **Jayapal Reddy C**, Sathyabhama A, Raghavendra S, “Lift Enhancement of an airfoil using Leading edge Triangular Protuberances for Small Scale Wind Turbine Blades”, 24th National and 2nd International ISHMT-ASTFE Heat and Mass Transfer Conference (IHMTTC-2017), BITS Pilani Hyderabad, 27-30 December 2017.
5. Raghavendra S, **Jayapal Reddy C**, Sathyabhama A, “Computational Evaluation of Aerodynamic Performance of Leading edge slots at Low Reynolds numbers”, 6<sup>th</sup> Asian Symposium on Computational Heat Transfer and Fluid Flow, Indian Institute of Technology Madras, Chennai, India, 10-23 December 2017.
6. Raghavendra S, **Jayapal Reddy C**, Sathyabhama A, “A Review on the Effect of Leading Edge Protuberances on the Performance of Wind Turbine Blade”, Proceedings of the National Conference on Advances in Thermal Engineering, September 23-24, 2016, Jadavpur University, Kolkata, India.

**Personal Details:**

Father Name	:	Ramakrishna Reddy C
Gender	:	Male
Date of Birth	:	10-April-1990
Marital Status	:	Married
Languages	:	Telugu, English, Kannada and Hindi
Hobbies	:	Playing Cricket, Travelling.
Nationality	:	Indian
Permanent Address	:	C/o C Ramakrishna Reddy 2-1eu, Garuguchintala Palli (V&P), Putlur (Mandal), Anantapuramu (District), Andhra Pradesh, INDIA. Pin: 515414.

**Jayapal Reddy C**